CARBON INJECTION INTO ELECTRIC ARC FURNACE SLAGS

CARBON INJECTION INTO ELECTRIC ARC FURNACE SLAGS

By

MATTHEW PETER KING, B.Eng.

A Thesis

Submitted to the School of Graduate Studies

in Partial Fulfillment of the Requirements

for the Degree

Master of Applied Science

McMaster University

MASTER OF APPLIED SCIENCE (2009)   McMaster University

(Materials Science and Engineering)   Hamilton, Ontario, Canada

TITLE: Carbon Injection into Electric Arc Furnace Slags

AUTHOR: Matthew Peter King, B.Eng. (McMaster University, Canada)

SUPERVISORS: Dr. Kenneth S. Coley and Dr. Gordon A. Irons

NUMBER OF PAGES: xvii, 182

ABSTRACT

The reaction between carbon and iron oxide-containing slag is crucial to efficient electric arc furnace steelmaking. The reaction occurs via gaseous intermediates, and the rate of gas generation by carbon gasification is limited by the chemical reactions at the slag-gas and carbon-gas interfaces. The aim of the present study was to obtain an understanding of the gasification rate limiting factors and slag foaming behaviour that could be readily applied to industrial electric arc furnace situations.

The rate of carbon gasification was measured in experimental simulations of an electric arc furnace heat with slags containing between 21.6 and 48.2 wt % 'FeO'. It was found that rate control was dominated by the carbon-gas chemical reaction.

A model was developed which describes the carbon gasification rate, amount of residual carbon in the slag, gas composition, slag-gas interfacial area and bubble diameter during carbon injection into slag. The model predicts rate control by the carbon-gas chemical reaction, in agreement with experimental observations.

The slag foaming behaviour was investigated, and it was found that the foaming index is a useful parameter in quantifying foam height only if void fraction is constant with respect to gas flow rate. The average bubble size was observed to be an important factor in determining foam stability, with smaller bubble size resulting in greater foam height.

ACKNOWLEDGEMENTS

I am very grateful to my supervisors, Dr. K.S. Coley and Dr. G.A. Irons, for their guidance and encouragement. I am greatly indebted for the challenges and learning opportunities I was given studying under their direction. Their ideas were very helpful in the course of this work.

I wish to thank Dr. F. Z. Ji for the many hours of extra work he performed on my behalf. His mentoring is much appreciated and his depth of understanding and technical proficiency will be an encouragement to me in years to come.

In performing experiments, the extraordinary skill of Mr. Owen Kelly was invaluable. All of the staff of the department of Materials Science and Engineering are thanked for creating a warm and welcoming academic environment, and for working tirelessly on behalf of the students.

I would like to thank the McMaster Steel Research Center and its member companies, whose generous financial support enabled me to pursue my studies.

I owe very much to my parents for all their support and unconditional love through the difficult times.

And to Melanie, thank you for your enormous love and patience, for the smiles and laughs. You have my deepest gratitude and love.

TABLE OF CONTENTS

LIST OF FIGURES

LIST OF TABLES

ABBREVIATIONS AND SYMBOLS

Abbreviations

EAF – Electric arc furnace

GPMT – Gas phase mass transport

LPMT – Liquid phase mass transport

NCR 1 – Injection experiment "Nucor 1"

R – Repeat

Symbols

a_O – Oxygen activity of the slag

A_c – Cross-sectional area of the container [m^2]

A_{sl} – Slag-gas interfacial area [m^2]

c_{ij} – Margules constants

C_{Fe} – Total iron concentration in the bulk slag in [mol %]

C_{Fe}° – Total iron concentration in bulk slag at time zero [mol %]

d_b – Bubble diameter [m]

d_p° – Average injected coal particle diameter [m]

D – Diffusivity [cm^2 s^{-1}]

D_e – Effective diffusivity [m^2 s^{-1}]

D_k – Knudsen diffusivity

D_m – Molecular inter-diffusivity

D_p – Average pore diffusivity

g – Specific gravity

Δh – Change in slag height from flat bath to steady-state foamed condition [m]

j_r – Reduced superficial gas velocity [m s^{-1}]

j_y – Specific rate constant of reaction y

J_i – Rate of reaction of species i

k_a – Apparent rate constant for reaction at slag-gas interface [mol m^{-2} atm^{-1} s^{-1}]

k_C – Rate constant for reaction at carbon-gas interface [mol m^{-2} atm^{-1} s^{-1}]

k_{gmt} – Rate constant for gas phase mass transport [mol m^{-2} atm^{-1} s^{-1}]

k_{lmt} – Rate constant for liquid phase mass transport [mol m^{-2} atm^{-1} s^{-1}]

k_0 – Overall rate constant for carbon-gas-slag reaction [mol m^{-2} atm^{-1} s^{-1}]

k_a° – Temperature-dependent constant for a given slag composition [mol O cm^{-2} atm^{-1} s^{-1}]

$k_a^{t=0}$ – Rate constant for reaction at slag-gas interface at time zero [mol O m^{-2} atm^{-1} s^{-1}]

k_i – Intrinsic rate constant per unit total pore surface area

k_{PI} – Partial internal burning rate constant

K – Equilibrium constant

m_s – Mass transfer coefficient [cm s^{-1}]

M_i – Molecular weight of species i [kg mol^{-1}]

n_i – Number of moles of component i

n_C° – Number of moles of carbon at time zero

N_p – Number of particles

p_{CO} – Partial pressure of CO [atm]

p_{CO_2} – Partial pressure of CO$_2$ [atm]

$p_{CO_2}^C$ – Equilibrium partial pressure of CO$_2$ at carbon-gas interface [atm]

$p_{CO_2}^S$ – Equilibrium partial pressure of CO$_2$ at slag-gas interface [atm]

$p_{CO_2}^{\chi}$ – Experimental partial pressure of CO$_2$ before post-combustion [atm]

p^S – Pressure of the reacting gas at the external surface [atm]

pct FeO^b – FeO content in bulk slag [wt%]

pct FeO^e – FeO content at slag-gas interface [wt%]

P_{tot} – Total pressure [atm]

q – Constant in slag-gas rate constant model [mol O m^{-2} atm^{-1} s^{-1} (mol Fe)$^{-2}$]

Q – Flow rate of gas

r – Ratio of Fe^{3+} to Fe^{2+}

R – Gas constant

R_i – Rate of carbon injection [mol s^{-1}]

R_p – Rate of carbon particle injection [particles s^{-1}]

S – Pore surface area per unit mass [m^2 kg^{-1}]

SI – Coal screening mesh size [mm]

t – Time [s]

t_{inj} – Time of carbon injection cessation [s]

t_{res} – Residence time of carbon particle in slag [s]

T – Temperature

u – Induced net gas velocity away from carbon surface [m s^{-1}]

V – Volume [m^3]

V_g^s – Superficial gas velocity [m s^{-1}]

w – Mass [kg]

X_i – Mole fraction of species i

X_i^e – Equivalent cation fraction of species i

z – Thickness of gas film [mm]

α – Parameter that quantifies dependence of slag rate constant on oxygen potential, or void fraction of slag foam

χ – Experimental parameter used to account for post-combustion

Δ_{Fe} – Decrease in iron concentration in the slag over the time of carbon injection [mol %]

ε – Volumetric fraction of solid particles in slag

γ_i – Activity coefficient of species i

ρ – Density [kg m^{-3}]

Φ_1 – Temperature-dependent carbon rate parameter [atm^{-1} min^{-1}]

Φ_2 – Temperature-dependent carbon rate parameter [atm^{-1} min^{-1}]

ϕ_{CO} – Temperature-dependent carbon rate parameter related to surface poisoning by CO [atm]

θ – Porosity

Γ_i – Surface concentration of species i

Λ – Optical basicity of slag

Σ – Foaming index [s]

μ – Viscosity of slag [Pa s]

μ_{eff} – Effective viscosity of slag [Pa s]

σ – Surface tension of slag [N m^{-1}]

Chapter 1: Introduction

1.1 Electric Arc Furnace Steelmaking

Over the past 40 years, electric arc furnace (EAF) steelmaking has undergone tremendous growth, now accounting for almost 34 percent of world-wide steel production and 41 percent of Canada's steel production. Concurrently, the sophistication of the EAF process has increased dramatically, utilizing oxy-fuel burners, lances and carbon injection along with electrical power supplied to the electrodes. Foamy slag, an established technique in modern EAF operations, serves to increase the electrical and thermal efficiency of the furnace by shielding the furnace walls and roof from the electric arc and by providing a thermal insulation layer. Slag foaming also decreases electrode consumption and increases furnace lining service life. Foamy slag is achieved by injecting particulate carbon, in the form of coal or coke, beneath the slag surface using a carrier gas. This can be done through a moveable lance pipe or fixed injection ports around the periphery of the furnace, usually during the late stages of scrap melting and in the subsequent steel refining period in an EAF heat. The carbon reacts with iron oxide in the slag, generating carbon monoxide and carbon dioxide at a rate sufficient to give a high volume fraction of bubbles. With appropriate slag physical properties, foam 30 to 50 cm deep is created and maintained for tens of minutes, surrounding and shielding the arc and lower electrodes.

1.2 Situation of the Subject

Most EAF operations are stable and repeatable from day to day. This, however, does not mean they are optimized. The EAF is a very harsh environment, making direct observations and measurements inside the furnace difficult. So, although the EAF is a very successful process, knowledge of what is actually happening inside the furnace is mainly empirical. It is desirable to have a better fundamental understanding of EAF operation in order to take the process to a higher level of maturity.

Much research has been done in the last two decades towards an understanding of slag foaming (Ito and Fruehan, 1989; Jiang and Fruehan, 1991; Zhang, 1992; Ogawa et al., 1993; Zhang and Fruehan, 1995; Ozturk and Fruehan, 1995; Jung and Fruehan, 2000; Lahiri and Seetharaman, 2002; Lotun and Pilon, 2005). The mechanisms and kinetics of the carbon-CO-CO_2 reaction are reasonably well-understood, having been studied by numerous researchers (Gulbransen et al., 1965; Turkdogan et al., 1968; Turkdogan and Vinters, 1969 and 1970; Tien and Turkdogan, 1970; Story et al., 1998; Fruehan et al., 2000; Story and Fruehan, 2000; Warczok and Utigard, 2000). The slag-CO-CO_2 reaction has been researched extensively (Sasaki et al., 1984; El-Rahaiby et al., 1986; Sun, 1988; Mori et al., 1996; Li et al., 2000; Li and Ratchev, 2002; Matsuura et al., 2004; Barati and Coley, 2005 and 2006). The carbon-H_2-H_2O and slag-H_2-H_2O reactions may be of importance if higher volatile coal is used as the carbon source. A number of studies have been carried out on the slag-H_2-H_2O reaction

(Hayes, 1979; Meschter and Grabke, 1979; Sasaki and Belton, 1983 and 1986; Ban-ya et al., 1984; Nagasaka, 1985; Glaws and Belton, 1990; Nagasaka et al., 2000; Xie and Belton, 2003), but the only work that has been done regarding the carbon-H_2-H_2O reaction in the correct temperature and composition range for steelmaking is that by Story and Fruehan (2000). More comprehensive investigations of carbon injection into EAF slags have been carried out by at least four groups: Morales et al. (1995, 1997 and 2001) and Rodriguez et al. (2001), Oltmann and Pretorius, Sahajwalla et al. (2006), and the group at McMaster University (Ji et al., 2002, 2003, 2004, 2005a and 2005b; Irons, 2005a and 2005b).

Chapter 2: Literature Review

2.1 Main Reactions during Carbon Injection into EAF Slags

Some slag foaming occurs naturally in the EAF as a result of CO and CO_2 generated by oxidation of carbon in the steel by the slag; however, it is desirable to increase and sustain foaming beyond what the system can naturally provide. Therefore oxygen is injected into the steel to form additional iron oxide, which floats into the slag. Because of this it is typical to have a large amount of iron oxide in the slag at the time in the heat when carbon is injected to foam the slag, in the range of 20 – 45 wt% 'FeO'. A particulate source of carbon (coal or coke) is injected into the slag to react with the iron oxide; carbon and hydrogen in the coal or coke are oxidized which results in production of CO, CO_2, H_2, and H_2O. The kinetics of the carbon-CO_2 and carbon-H_2O reactions are analogous (Story and Fruehan, 2000) and metallurgical carbon sources typically used in the EAF are mainly carbon, so in this discussion only the carbon-CO-CO_2 system will be referred to.

The slag-carbon reaction occurs by the following mechanism. The overall reaction (2.1) occurs via two reactions involving gaseous intermediates, (2.2) at the slag-gas interface and (2.3) at the carbon-gas interface.

$$C(s) + O(slag) = CO(g) \qquad\qquad (2.1)$$

$$(2Fe^{3+}, 3O^{2-} \text{ or } Fe^{2+}, O^{2-}) + CO(g) = (2Fe^{2+}, 2O^{2-} \text{ or } Fe(l)) + CO_2(g) \quad (2.2)$$

$$CO_2(g) + C(s) = 2CO(g) \quad (2.3)$$
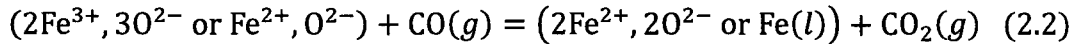
2.2 Possible Rate Determining Steps

The most likely rate-limiting steps for reaction (2.1) are given by Story et al. (1998) as the following:

1) Diffusion of 'FeO' (Fe^{3+} or Fe^{2+} and O^{2-} ions) from the bulk slag to the slag-gas interface (liquid phase mass transport).

2) Chemical reaction at the slag-gas interface, reaction (2.2).

3) Diffusion of CO_2 from the slag-gas interface to the carbon-gas interface (gas phase mass transport).

4) Chemical reaction at the carbon-gas interface, reaction (2.3).

The overall rate constant, adapted from Min et al. (1999), is expressed by equation (2.4),

$$k_0 = \cfrac{1}{\cfrac{1}{k_c} + \cfrac{1}{k_a} + \cfrac{1}{k_{gmt}} + \cfrac{1}{k_{lmt}}} \quad (2.4)$$

where k_c and k_a are rate constants for the carbon-gas and slag-gas reactions and k_{gmt} and k_{lmt} are rate constants for gas and liquid phase mass transport, respectively.

For the case of coke reacting with slag of higher 'FeO' contents, liquid phase mass transport (LPMT) and gas phase mass transport (GPMT) become less important to the overall rate of reaction due to higher rates of gas evolution and the resulting stirring effect (Story et al., 1998). This is shown in Figure 2.1, where the lines show the maximum rate achievable assuming each of the steps in turn is rate-limiting, and the line labelled "overall" shows the calculated rate assuming mixed control by all four of the possible rate-limiting steps. The open circles show data points from Sarma et al. (1996). This analysis has been confirmed by Min et al. (1999).
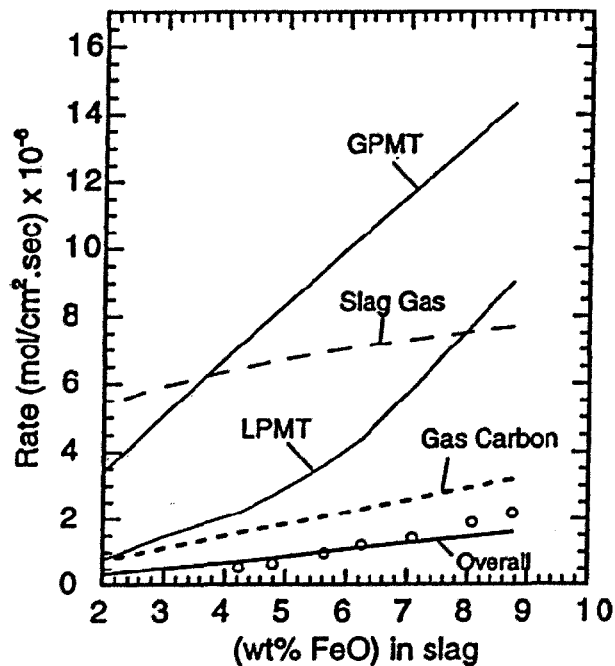
Figure 2.1 - Comparison of experimental measurements with rate model predictions for stationary 2.5 cm diameter coke rods (Story et al., 1998)

2.3 Liquid Phase Mass Transport

A model to describe mass transport in the liquid slag has been developed by Sarma et al. (1996) for the case in which reaction (2.1) is limited only by the diffusion of FeO from the bulk slag to the slag-gas interface and the activity coefficient of FeO, γ_{FeO}, is independent of FeO concentration. The reaction rate of FeO is expressed by equation (2.5),

$$-J_{FeO} = J_{CO} = \frac{m_s \rho}{100 \, M_{FeO}} (\text{pct FeO}^b - \text{pct FeO}^e) \qquad (2.5)$$

where J_i is the reaction rate [mol cm^{-2} s^{-1}] of species i, m_s is the mass transfer coefficient [cm s^{-1}], M_{FeO} is the molecular weight of FeO [g mol^{-1}], ρ is the slag density [g cm^{-3}], and pct FeO^b and pct FeO^e are the FeO content [wt %] in the slag bulk and at the slag-gas interface respectively.

The experiments carried out by Sarma et al. (1996) used a rotating carbon rod immersed in CaO-SiO$_2$-Al$_2$O$_3$-FeO slags. They found that the reaction rate increased with increasing FeO content and with increasing rod rotation speed.

2.4 Gas Phase Mass Transport

The slag-carbon reaction is known to proceed with gaseous intermediates between the carbon and slag (Sarma et al., 1996; Min et al. 1999). As soon as the carbon is wetted by the slag and the reaction begins, a gas film is formed. If the thickness of this film is greater than a few millimetres, it is possible that gas-phase

mass transport is the rate determining step, since the gas diffusion rate decreases linearly with increasing film thickness (Min et al., 1999).

Min et al. (1999) calculated the rate of CO_2 transfer in the gas phase as follows. If inter-diffusion of CO_2-CO in the gas film is rate determining the CO_2 flux, J_{CO_2}, can be expressed as

$$J_{CO_2} = -\frac{DP_{tot}}{RT} \times \frac{dX_{CO_2}}{dx} + \left(J_{CO} + J_{CO_2}\right)X_{CO_2} \qquad (2.6)$$

where D and X_{CO_2} are the diffusivity [cm^2 s^{-1}] and mole fraction of CO_2, respectively, dX_{CO_2}/dx is the concentration gradient in the gas film, and P_{tot} is the total pressure of the system.

The slag-gas reaction (2.2) and carbon-gas reaction (2.3) are at equilibrium if CO_2-CO mass transport is rate-limiting. According to the mass balance of equation (2.3), $J_{CO} = -2J_{CO_2}$, so equation (2.6) can be expressed as

$$J_{CO_2} = -\frac{DP_{tot}}{zRT} \times \ln\frac{1 + p_{CO_2}^s}{1 + p_{CO_2}^C} \qquad (2.7)$$

where $p_{CO_2}^s$ and $p_{CO_2}^C$ are the equilibrium partial pressures of CO_2 at the slag-gas and carbon-gas interfaces, respectively, and z is the thickness of the gas film. Assuming the thickness of the gas film was 1 mm, Min et al. (1999) calculated the inter-diffusivity of CO_2 to be $D = 3.6$ cm^2 s^{-1} using an equation by Fuller (Geiger and Poirier, 1937).

2.5 Carbon Oxidation

The carbon oxidation reaction is given by equation (2.3). Work on the topic of carbon oxidation in CO_2-CO gas mixtures has been done by Turkdogan and his colleagues (Turkdogan et al., 1968; Turkdogan and Vinters, 1969 and 1970; Tien and Turkdogan, 1970) and more recently by Story and Fruehan (2000) and Warczok and Utigard (2000).

There exist three distinct regimes of carbon oxidation behaviour, referred to by Turkdogan et al. as complete internal burning, partial internal burning, and external burning. The size of the carbon particle, temperature and gas pressure determine the extent of pore diffusion and therefore the extent of internal burning.

The effect of pore structure on the rate of carbon oxidation is very complex. The rate constant is strongly dependent on the available reaction area and hence is dependent on the type of carbonaceous material. The porosity of the reacted layer, not the initial (unreacted) available specific internal surface area, determines the observed rate (Story et al., 1998). Depending on the rate control regime, the reacted layer may extend throughout the entire particle (complete internal burning), may exist only on the surface of the particle (partial internal burning), or may not exist at all (external burning). The reacted layer increases in porosity as the reaction progresses, and its pore structure is also temperature-dependent. In addition, if the carbonaceous material contains ash and is reacted at

high temperatures, the ash may melt, becoming a slag which covers pore surface area and decreases the surface area available for reaction.

Turkdogan and Vinters (1970) found that CO retards the rate of oxidation because of its strong surface poisoning effect, and that it changes the rate control mechanism. They performed a detailed analysis of the chemical reaction kinetics for the case of complete internal burning, deriving rate equations from fundamental principles and experimentally verifying them (Turkdogan and Vinters, 1969 and 1970). Tien and Turkdogan (1970) carried out a mathematical investigation of the kinetics in the partial internal burning regime for different carbon particle geometries and limiting cases of rate control.

Carbon oxidation has mainly been studied at temperatures below 1300°C due to gas-phase mass transport limitations (Fruehan et al., 2000). By employing an impinging jet technique which eliminated or allowed correction for external gas-phase mass transport to the carbon surface, Story and Fruehan (2000) studied the kinetics of carbon oxidation by CO_2 and H_2O at higher temperatures than other investigations. Their experimental design ensured that carbon reaction behaviour was within the limited mixed regime, in which oxidation takes place inside the particle but pore diffusion is incomplete, equivalent to Turkdogan's partial internal burning regime. They suggested a mechanism for the carbon oxidation reaction and a corresponding Langmuir-type rate equation, and also performed experimental work in the partial internal burning regime and used a

rate equation applicable to that regime to gain useful insights into the fundamentals.

Warczok and Utigard (2000) investigated the oxidation of solid graphite rods in pure CO_2 in the external burning regime. They derived a rate equation, taking into consideration the effect of the net gas flow away from the carbon surface due to the extra mole of gas produced per mole of carbon consumed, and found excellent agreement with experimental results.

2.5.1 Rate Control Regimes

Turkdogan et al. (1968) investigated the effects of size, pressure and temperature on the extent of internal burning of carbon particles in pure CO_2. As temperature, gas pressure or size of the carbon particle increase, the diffusion of gaseous species in and out of the pores of the carbon may become sufficiently slow, compared to chemical reaction at the gas – pore surface interface, that a gas composition gradient develops across the carbon particle. There exist three cases of rate control: 1) complete internal burning, 2) partial internal burning and 3) external burning.

1) Complete internal burning exists when diffusion through the pores of the carbon is complete. No concentration gradient exists, and the composition of the gas in the pores is the same as that of the bulk gas outside the particle. This case occurs at moderate temperatures (800-900°C, increasing with smaller particle size) and small particle sizes (less than about 1 cm diameter).

The rate of oxidation is controlled by chemical reaction at the gas – pore surface interface, and the rate is directly proportional to the mass of carbon. The rate constant is proportional to the pore surface area per unit mass of carbon. The apparent activation energy of the process is the true activation energy of the reaction (Story and Fruehan, 2000).

2) Partial internal burning exists when diffusion through the pores of the carbon is incomplete. At some finite distance within the particle the concentration of CO_2 approaches its equilibrium value. The rate of oxidation is controlled by both chemical reaction and pore diffusion. This case occurs at higher temperatures (1000-1300°C, or other ranges depending on particle size, pressure and gas velocity). According to Thiele's analysis (Thiele, 1939) based on a simple model for a first-order type reaction, when the rate is controlled by a pore diffusion/chemical reaction dual process the rate is directly proportional to the external surface area of the carbon particle. The apparent activation energy is equivalent to one-half the true activation energy (Story and Fruehan, 2000).

3) External burning exists when the rate of chemical reaction exceeds that of pore diffusion to such an extent that there is no diffusion into the pores. Oxidation is completely external to the surface of the carbon. This case occurs at sufficiently high temperatures depending on particle size, pressure and gas velocity. The rate of oxidation is controlled by a gas-film diffusion process and is proportional to the external surface area of the carbon particle. Bulk

diffusion processes have low activation energies, so the apparent activation energy is very small (Story and Fruehan, 2000).

The effect of particle size on the rate of oxidation is expected to be as shown in Figure 2.2 for a given temperature and pressure of CO_2. As rate is proportional to the mass of the carbon particle in chemical reaction control, rate plotted against particle diameter on a log-log plot should yield a slope of 3:1. In pore diffusion control, where rate is proportional to the external surface area of the particle, the slope of rate versus diameter on a log-log plot should be 2:1. The experimental results of Turkdogan et al. (1968) agreed well with this prediction. The critical dimensions for electrode graphite were estimated and are given in Table 2.1.

The temperature dependence of the rate of oxidation of small graphite particles, exhibiting nearly complete pore diffusion, was studied by Turkdogan et al. (1968). The apparent activation energy of the reaction $CO_2 + C = 2CO$ was found to be 305 kJ mol^{-1} CO_2. The apparent activation energy for the reaction $CO_2 + C = 2CO$ in the temperature range 900 to 950°C was estimated to decrease from 305 kJ mol^{-1} CO_2 at $p_{CO_2} = 0.24$ atm to 205 kJ mol^{-1} CO_2 at $p_{CO_2} = 30$ atm, which is an indication of incomplete pore diffusion as the predominant rate-controlling mechanism at high pressures.
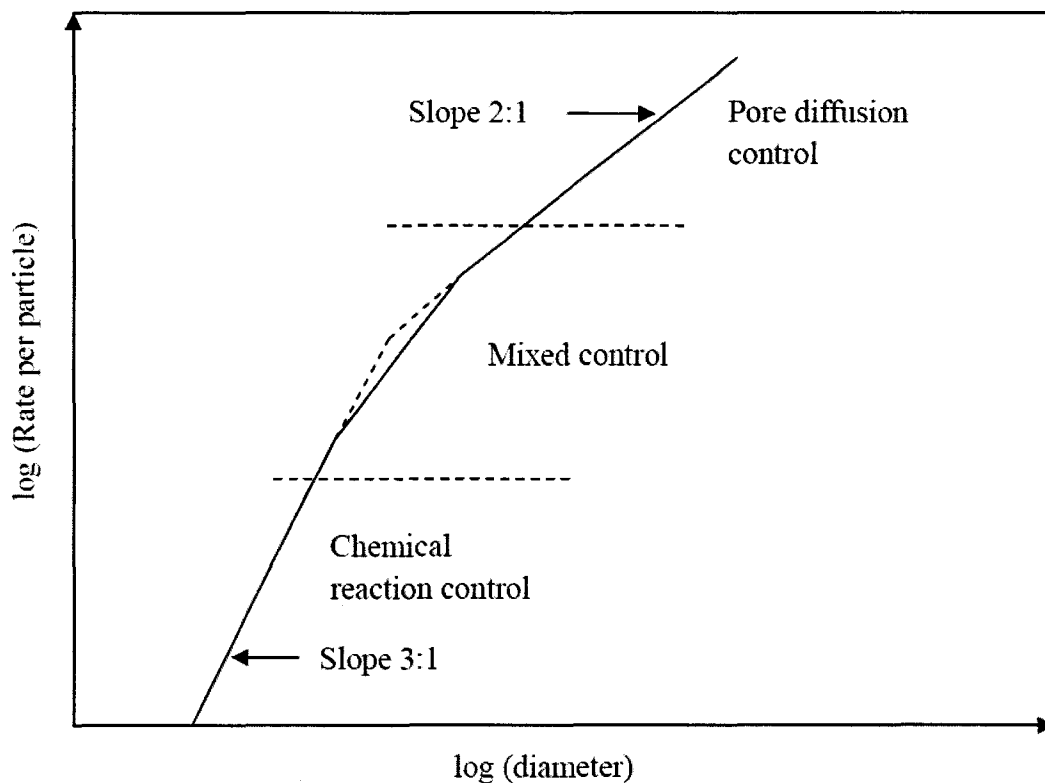
Figure 2.2 - Effect of particle size on rate limiting mechanism (Turkdogan et al., 1968)

Table 2.1 - Estimated critical electrode graphite sphere diameter (Turkdogan et al., 1968)

Temperature [°C]	Estimated critical electrode graphite sphere diameter [cm]	
	Chemical reaction control	Pore diffusion control
900	<0.6	>2
1000	<0.3	>1
1100	<0.2	>0.7

2.5.2 Reaction Kinetics

2.5.2.1 Complete Internal Burning

A retardation of oxidation rate by CO, or by increasing pressure at fixed p_{CO_2}/p_{CO} ratios, was observed by Turkdogan and Vinters (1970) and is caused by:

1) Dilution of CO_2 (the oxidizing agent)

2) The reverse reaction, $2CO = CO_2 + C$

3) Poisoning of the carbon surface

They observed that in the case of complete pore diffusion, the rate of oxidation of carbon in CO_2-CO gas mixtures is controlled by two consecutive reactions in series. Considering the observed dependence of the rate on p_{CO_2}, they postulated that:

A) The rate of carbon oxidation with CO present is proportional to p_{CO_2}. The activated complex for the reaction involves two atoms of oxygen (one molecule of CO_2) and the rate-controlling reaction is the dissociation of CO_2 on the carbon surface:

$$CO_2(g) = CO_2(ads) = (CO_2)^{\ddagger} \rightarrow products~[C(s) + 2O(ads)] \qquad (2.8)$$
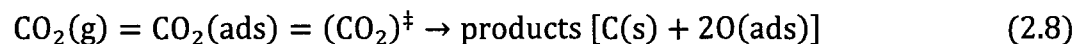
B) The rate of carbon oxidation with no CO present is proportional to $\sqrt{p_{CO_2}}$. The activated complex for the reaction involves one atom of oxygen (half a

molecule of CO_2) and the rate-controlling reaction is the formation of CO on the surface of carbon:

$$O(ads) + C(s) = (CO)^{\ddagger} \rightarrow products \qquad (2.9)$$

With sufficient CO present for dissociation of CO_2 to be the rate-controlling step, Turkdogan and Vinters (1970) gave the rate in units of [min^{-1}] as

$$v_C = -\frac{1}{w}\left(\frac{dw}{dt}\right) = \frac{\Phi_1}{1 + \left(\frac{p_{CO}}{\phi_{CO}}\right)}\left[p_{CO_2} - p_{CO_2}^C\right] \qquad (2.10)$$

where w is the mass of carbon [g], Φ_1 [atm^{-1} min^{-1}] and ϕ_{CO} [atm] are temperature-dependent parameters, and $p_{CO_2}^C$ is the equilibrium partial pressure of CO_2 at the carbon-gas interface.

With sufficiently low CO content for formation of CO to be the rate-controlling step, Turkdogan and Vinters (1970) gave the rate in units of [min^{-1}] as

$$v_C = \frac{\Phi_2}{1 + \left(\frac{p_{CO}}{\phi_{CO}}\right)}\left[\left(p_{CO_2}\right)^{1/2} - \left(p_{CO_2}^C\right)^{1/2}\right] \qquad (2.11)$$

where Φ_2 [atm^{-1} min^{-1}] is a temperature-dependent parameter. For the limiting case of $p_{CO} \rightarrow 0$, equation (2.11) simplifies to

$$v_C = \Phi_2\left(p_{CO_2}\right)^{1/2} \qquad (2.12)$$

The temperature-dependent parameters are given by Turkdogan and Vinters (1970) in units of [atm^{-1} min^{-1}] as follows.

For coconut charcoal:

$$\log \Phi_1 = -\frac{13200}{T} + 9.68 \qquad (2.13)$$

$$\log \Phi_2 = -\frac{15000}{T} + 11.00 \qquad (2.14)$$

For metallurgical coke:

$$\log \Phi_1 = -\frac{13200}{T} + 8.60 \qquad (2.15)$$

$$\log \Phi_2 = -\frac{15000}{T} + 9.98 \qquad (2.16)$$

For electrode graphite:

$$\log \Phi_1 = -\frac{13200}{T} + 7.68 \qquad (2.17)$$

$$\log \Phi_2 = -\frac{15000}{T} + 8.75 \qquad (2.18)$$

For metallurgical coke and electrode graphite:

$$\log \phi_{CO} = -\frac{5940}{T} + 3.46 \qquad (2.19)$$

Story and Fruehan (2000) suggested that the steps of the carbon oxidation reaction consist of a reversible oxygen exchange step and an irreversible carbon gasification step,

$$CO_2 + [.]_C \leftrightarrow [O]_C + CO(g) \tag{2.20}$$

$$[O]_C \rightarrow CO(g) + [.]_C \tag{2.21}$$

where $[.]_C$ represents a vacant carbon reaction site and $[O]_C$ represents an oxygen atom adsorbed on the carbon surface. This mechanism is consistent with a Langmuir rate equation,

$$v_C = \frac{k_1 p_r}{1 + k_2 p_p + k_3 p_r} \tag{2.22}$$

where p_r and p_p are the partial pressures of the reactant gas and product gas, respectively, and $k_1 = j_1([.]_C + [O]_C)$, $k_2 = j_{-1}/j_2$ and $k_3 = j_1/j_2$, where j_1 and j_2 represent the specific rate constants in the forward direction of reactions (2.20) and (2.21), respectively, and j_{-1} represents the specific rate constant in the backward direction of reaction (2.20).

At reduced partial pressures of CO_2 ($p_{CO_2} < 0.1$ atm), the denominator of the Langmuir rate equation approaches unity, so that rate becomes proportional to the partial pressure of CO_2; thus the kinetics are first order with respect to CO_2 at reduced partial pressures of CO_2. At high temperatures (> 1200°C), k_2 and k_3 decrease exponentially to negligibly small values and k_1 increases strongly with

increasing temperature, so again the denominator of the Langmuir rate equation approaches unity and rate becomes proportional to the partial pressure of CO_2; thus the kinetics are first order with respect to CO_2 at high temperatures. Therefore at high temperatures and/or reduced partial pressure of CO_2, the chemical reaction kinetics are first order with respect to p_{CO_2} (Story and Fruehan, 2000).

2.5.2.2 Partial Internal Burning

The investigation of the kinetics in the partial internal burning regime by Tien and Turkdogan (1970) considered the effects of particle size, temperature and pressure on the rate of oxidation of graphite and coke for the case of dual control (chemical reaction and incomplete pore diffusion) and was based on a mathematical analysis. A limiting case exists in which pore diffusion is rate-limiting to the extent that external burning is approached, and it is reached when p_{CO_2} at the center of the particle approaches that in equilibrium with CO and carbon at the given temperature and prevailing total pressure, the difference between p_{CO_2} at the center and p_{CO_2} near the outer surface of the particle is small enough to be approximated as zero, and the rate of oxidation is completely diffusion-controlled. In this situation, the rate equation for oxidation in 100 % CO_2 simplifies to:

$$v_C = \frac{5}{2}\sqrt{\frac{D_e}{R}\frac{P_{tot}K_1}{TK_2}} \qquad (2.23)$$

where v_C is the rate of oxidation, D_e is the effective diffusivity, P_{tot} is the total

pressure, $K_1 = \Phi_1 \cdot p/(12 \times 60)$ and $K_2 = 1/\phi_{CO}$. Equation (2.23) reveals

characteristic features of pore diffusion rate control (Tien and Turkdogan, 1970):

1) The rate per particle is proportional to the external geometrical surface area of

   the particle.

2) Most of the diffusive flux in the pores is by molecular diffusion at and above

   atmospheric pressure; therefore $D_e P$ is a constant and the rate of oxidation is

   independent of pressure.

Story and Fruehan (2000) used equation (2.24) (found in Fruehan et al.,

2000) to calculate the reaction rate in the partial internal burning (limited mixed)

regime.

$$v_C = \frac{(D_e \rho S k)^{1/2}}{RT} p^s \qquad (2.24)$$

As given by Chen (2005), the partial internal burning rate constant, k_{PI}, may be

expressed as

$$k_{PI} = \frac{(D_e \rho S k_i)^{1/2}}{RT} \qquad (2.25)$$

where D_e is the effective diffusivity, ρ is the density of the reacting layer (density

of carbon), S is the pore surface area per unit mass (specific internal surface area),

p^s is the pressure of the reacting gas at the external surface, and k_i is the intrinsic

rate constant expressed per unit total pore surface area. To compare their results

with those by Turkdogan, Story and Fruehan (2000) calculated the values of the intrinsic rate constant in their experiments by:

$$k_i = \frac{(k_{PI}RT)^2}{D_e \rho S} \tag{2.26}$$

The effective diffusivity may be estimated using the equation given by Weisz and Schwartz (1962),

$$D_e = \frac{\theta^2}{\sqrt{3}} D_p \tag{2.27}$$

where θ is the porosity and D_p is the average pore diffusivity. Assuming the effect of back-diffusion of CO is negligible, the average pore diffusivity may be calculated by the equation given by Pollard and Present (1948),

$$\frac{1}{D_p} = \frac{1}{D_k} + \frac{1}{D_m} \tag{2.28}$$

where D_k is the Knudsen diffusivity and D_m is the molecular inter-diffusivity. According to Youngquist (1970), D_k may be expressed as

$$D_k = 9700r \sqrt{\frac{T}{M_i}} \tag{2.29}$$

where r is the average pore radius and M_i is the molecular mass of the reacting gas species. An average pore radius on the order of 5 µm is reasonable for a typical carbonaceous material of larger pore size. The remaining quantities were

estimated by values found in literature; refer to the work by Story and Fruehan (2000) for references. The average bulk density (ρ) and porosity of the reacted layer (θ) were estimated to be 1.1 g cm^{-3} and 0.5, respectively. The internal surface area per unit mass value used was 21.4 m^2 g^{-1}.

The extrapolation of Turkdogan's data to higher temperatures agreed well with data from Story and Fruehan (2000) and from Gulbransen et al. (1965), however, the apparent activation energy of the graphite-CO_2 reaction found by Story and Fruehan was 172 kJ mol^{-1} compared to 305 kJ mol^{-1} by Turkdogan. An activation energy of 172 kJ mol^{-1} is consistent with the intrinsic (chemical reaction-limited) rate being controlled by the rate of CO_2 dissociation on the carbon surface, which was also the rate control step suggested by Turkdogan for the carbon oxidation reaction in the presence of CO. The difference in apparent activation energies may be explained by considering that Turkdogan's data was obtained in a lower temperature range, and that the apparent activation energy will be different in different temperature ranges making it difficult to compare the temperature dependence of rates taken over different temperature ranges (Story and Fruehan, 2000). The activation energy for dissociation of CO_2 on carbon given by Story and Fruehan (2000) is consistent with that found on slag surfaces, as in the work by Barati and Coley (2005).

2.5.2.3 External Burning

Warczok and Utigard (2000) undertook research to measure the rate of oxidation of solid graphite rods. Their experiments were performed at moderate to high temperatures (1020-1510°C) on large carbon particles (rods) in pure CO_2. The net production of one mole of gas as the carbon gasification reaction proceeds in the forward direction creates a net gas flow away from the carbon surface. This inhibits pore diffusion and the external mass transport of CO_2. It was observed that rate per unit area was independent of rod diameter, indicating that reaction took place mainly on the outer surface of the rod and that a negligible amount of pore diffusion occurred, likely due to the high temperatures and large carbon size. Therefore rate was controlled either by chemical reaction at the rod surface or by external mass transport of CO_2 to the surface. It was found that two rate-control mechanisms exist which operate in different temperature ranges:

$T \leq 1170°C$, rate is controlled by chemical reaction at the surface

$T \geq 1170°C$, rate is controlled by external mass transport to the surface

According to Warczok and Utigard (2000), the rate of CO_2 diffusion to the surface of carbon [mol m^{-2} s^{-1}] is

$$rate = -D\frac{d[CO_2]}{dx} - u[CO_2] \tag{2.30}$$

where D is the diffusion coefficient of CO_2 in the gas phase [m^2 s^{-1}], u is the induced net gas velocity away from the carbon surface [m s^{-1}] and [CO_2] is the

molar concentration of CO_2 [mol m^{-3}]. The ideal gas law was used to relate the velocity u to the rate of reaction,

$$u = \frac{RT}{P} \cdot rate \tag{2.31}$$

Combining equations (2.30) and (2.31), the rate was expressed as

$$rate = \frac{-D \frac{d[CO_2]}{dx}}{1 + \frac{RT}{P}[CO_2]} \tag{2.32}$$

Upon integration across a distance z (film thickness), the rate expression became

$$rate = \frac{DP}{RTz} \ln\left(\frac{1 + X_{CO_2,b}}{1 + X_{CO_2,c}}\right) \tag{2.33}$$

where $X_{CO_2,b}$ and $X_{CO_2,c}$ are the mole fractions of CO_2 in the bulk gas and in the gas in contact with the carbon, respectively. Under mass transport control, $X_{CO_2,c}$ is small enough to approximate as zero, and under chemical reaction control, $X_{CO_2,c}$ is essentially equal to $X_{CO_2,b}$.

2.6 Slag Reduction

There have been many studies done in the last few decades on the chemical reaction rate of iron oxide-containing slags with CO_2-CO gas mixtures (Sasaki et al., 1984; El-Rahaiby et al., 1986; Sun, 1988; Mori et al., 1996; Li et al., 2000; Li and Ratchev, 2002; Matsuura et al., 2004; Barati and Coley, 2005 and 2006). There is agreement on the basic form of the rate equation, yet

inconsistencies persist regarding the effects of slag characteristics (oxygen potential, iron oxide content and bulk slag composition) on the rate. Barati and Coley (2005) have measured the rate of interfacial reaction between CO_2-CO and CaO-SiO_2-FeO_x slags using the $^{13}CO_2$-CO isotope exchange technique for a wide range of slag iron oxide contents and basicities, investigating the effects of temperature and equilibrium oxygen potential on the apparent rate constant. From knowledge gained through this investigation they were able to develop a comprehensive kinetic model to predict the rate of reaction of CO_2-CO with FeO_x-containing slags (Barati and Coley, 2006) which resolves some inconsistencies.

2.6.1 Reaction Kinetics

The interfacial chemical reaction between slag and CO_2-CO is one of the following:

$$(Fe^{3+}, 1.5O^{2-}) + 0.5CO = (Fe^{2+}, O^{2-}) + 0.5CO_2 \qquad (2.34)$$

$$(Fe^{2+}, O^{2-}) + CO = Fe + CO_2 \qquad (2.35)$$
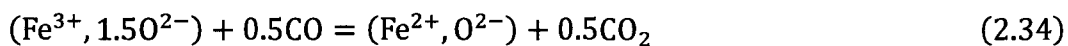
The reaction between slag and CO_2-CO gas mixtures can be written in its simplest form as

$$CO(g) + O(slag) = CO_2(g) \qquad (2.36)$$
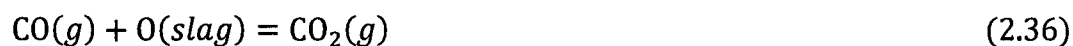
From left to right is the slag reduction reaction (*red*); from right to left is the slag oxidation reaction (*ox*).

There is general agreement in the literature that the rate equation for oxygen transfer with molten slag is of the form

$$v_O = k_a^\circ \left(p_{CO} \cdot a_O^{1-\alpha} - p_{CO_2} \cdot a_O^{-\alpha} \right) \tag{2.37}$$

where k_a° is a temperature-dependent constant for a given slag composition [mol O cm^{-2} atm^{-1} s^{-1}], α is an empirical parameter that quantifies the degree of dependence of the rate constant on the oxygen potential, and a_O is the oxygen activity of the melt, defined as in equation (2.38) as the equilibrium CO_2/CO ratio at the slag-gas interface with standard state $CO_2/CO = 1$.

$$a_O = \left(\frac{p_{CO_2}}{p_{CO}} \right)_{eq,s-g} \tag{2.38}$$

The rate equation may also be written in the form

$$v_O = k_a \left(p_{CO} \cdot a_O - p_{CO_2} \right) \tag{2.39}$$

where k_a is the apparent rate constant [mol O cm^{-2} atm^{-1} s^{-1}]. The apparent rate constant is a complex function of the oxygen potential a_O, the slag iron oxide content and basicity, and temperature.

2.6.1.1 Effect of Oxygen Potential

The apparent rate constants of the slag reduction and slag oxidation reactions can be derived from equation (2.37) as

$$k_a^{red} = k_a^\circ (a_O)^{1-\alpha} \tag{2.40}$$

and

$$k_a^{ox} = k_a^{\circ}(a_O)^{-\alpha} \qquad \qquad (2.41)$$

There is discrepancy in the literature as to the value of α. Barati and Coley (2005) observed that the dependence of α on the iron oxide content in CaO-SiO_2-FeO_x melts with unit CaO/SiO_2 can be expressed as

$$\alpha = 0.004 \times wt\,\% \; FeO + 0.5088 \qquad \qquad (2.42)$$

Li et al. (2000) give the value of α as 0.80 for the oxidation reaction and 0.82 for the reduction reaction at 1773 K with pure liquid iron oxide. Because the values of α are nearly equal for the reduction and oxidation reactions, it is reasonable to conclude that the first-order (with respect to the partial pressure of reacting gases) reaction between iron oxide and CO_2-CO is microscopically reversible (Li et al., 2000). El-Rahaiby et al. (1986) observed the value of α to be 0.75 at 1693 K and 0.86 at 1793 K for slags with 5 mol % 'FeO' and unit CaO/SiO_2.

Sasaki et al. (1984) suggested a charge transfer model to explain the observed inverse relationship between the apparent rate constant and the oxygen activity a_O, and it was summarised and expanded upon by Barati and Coley (2005). Because oxygen exists in the molten slag as a charged ion, dissociation of CO_2 at the surface of this ionic melt will involve charge transfer. Assuming the intermediate complex in the dissociation reaction is a doubly-charged CO_2 ion

(CO_2^{2-}), introducing oxygen ions (O^{2-}) into the slag (the slag oxidation reaction) involves the following elementary reactions:

$$CO_2(g) + \blacksquare = CO_2(ads) \tag{2.43}$$

$$CO_2(ads) + 2e^- \rightarrow CO_2^{2-}(ads) \tag{2.44}$$

$$CO_2^{2-}(ads) \rightarrow CO(ads) + O^{2-} \tag{2.45}$$

The symbol $\blacksquare$ in equation (2.43) represents a suitable site for adsorption of CO_2. The surface concentration of CO_2^{2-}, $\Gamma_{CO_2^{2-}}$, can be expressed as a function of p_{CO_2} by assuming adsorbed CO_2 to be in equilibrium with CO_2 in the gas phase as in equation (2.43) and considering the virtual redox equilibria

$$CO_2(ads) + 2Fe^{2+} = CO_2^{2-}(ads) + 2Fe^{3+} \tag{2.46}$$
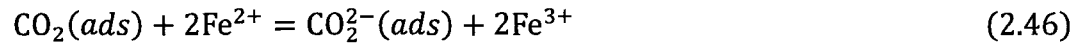
Then,

$$\Gamma_{CO_2^{2-}} \propto p_{CO_2} \left(\frac{Fe^{2+}}{Fe^{3+}} \right)^2 \tag{2.47}$$

If either reaction (2.44) or (2.45) is the rate determining step, the rate law for the slag oxidation reaction is

$$v = k p_{CO_2} \left(\frac{Fe^{2+}}{Fe^{3+}} \right)^2 \tag{2.48}$$

where k is the rate constant for the slag oxidation reaction for a given number of reaction sites. If the redox reaction of iron oxides in slags may be written as in equation (2.34), the redox equilibrium is expressed by

$$\frac{Fe^{3+}}{Fe^{2+}} \propto \frac{\gamma_{FeO}}{\gamma_{FeO_{1.5}}} \left(\frac{p_{CO_2}}{p_{CO}}\right)^{0.5} \tag{2.49}$$

If the ratio $\gamma_{FeO}/\gamma_{FeO_{1.5}}$ remains "ideally" constant, α has its ideal value of 1. However, the value of α is observed to deviate from 1, and Barati and Coley (2005) suggest that this deviation may be due one or both of the following reasons:

1) The redox equilibrium of iron oxide does not follow ideal behaviour.

2) The rate-controlling reaction involves transfer of a single charge. Dissociation of CO_2 on the slag surface may involve the formation of singly- or doubly-charged ions or a combination of both. The value of α, varying between 0.5 and 1, is related to the relative stability of intermediate complexes CO_2^- and CO_2^{2-} at different conditions.

2.6.1.2 Effect of Iron Oxide Content

The work by Barati and Coley (2005) presents clearly the effect of iron oxide content on the apparent rate constant. The comparison reproduced in Figure 2.3 includes the results of the studies by Li and Ratchev (2002), Mori et al. (1996), Sun (1988), and Barati and Coley (2005). It shows that increasing the iron oxide content up to 30 wt % has little impact on the rate, while increasing it from

30 to 100 wt % drastically increases the rate. Differences in the absolute values of rate constant between the different studies can be attributed to differences in slag basicity and temperature. On the other hand, El-Rahaiby et al. (1986) observed that changing iron oxide content from 5 to 100 mol % does not affect the apparent rate constant in calcium iron silicate slags with unit CaO/SiO_2.

The data of Barati and Coley (2005), measured using the $^{13}CO_2$-CO isotope exchange technique, agree closely with that of Li and Ratchev (2002) which was measured using a thermo-gravimetric technique. According to Barati and Coley (2005), the dependence of the apparent rate constant on iron oxide content at 1773 K, unit CaO/SiO_2 and $CO_2/CO = 1$ can be represented by equation (2.50),

$$k_a = 0.11 \cdot \exp(0.0383 \times wt\,\%\,FeO) \tag{2.50}$$

The increase in the value of the rate constant with increasing iron oxide content may be explained by considering the charge transfer mechanism, which requires adsorption of CO_2 on the surface of the melt and its subsequent dissociation as shown in equations (2.43), (2.44) and (2.45). The suitable site for adsorption as represented by the symbol ■ in equation (2.43) must be located on two Fe^{2+} sites because these sites are used in two ways in the reaction: to provide electrons for the formation of activated charged complexes and to coordinate with the resulting oxygen ion in the oxidized melt structure (Barati and Coley, 2006). Therefore

increasing the iron oxide content will increase the concentration of available

ferrous sites for the adsorption of CO_2 and its subsequent dissociation reaction.
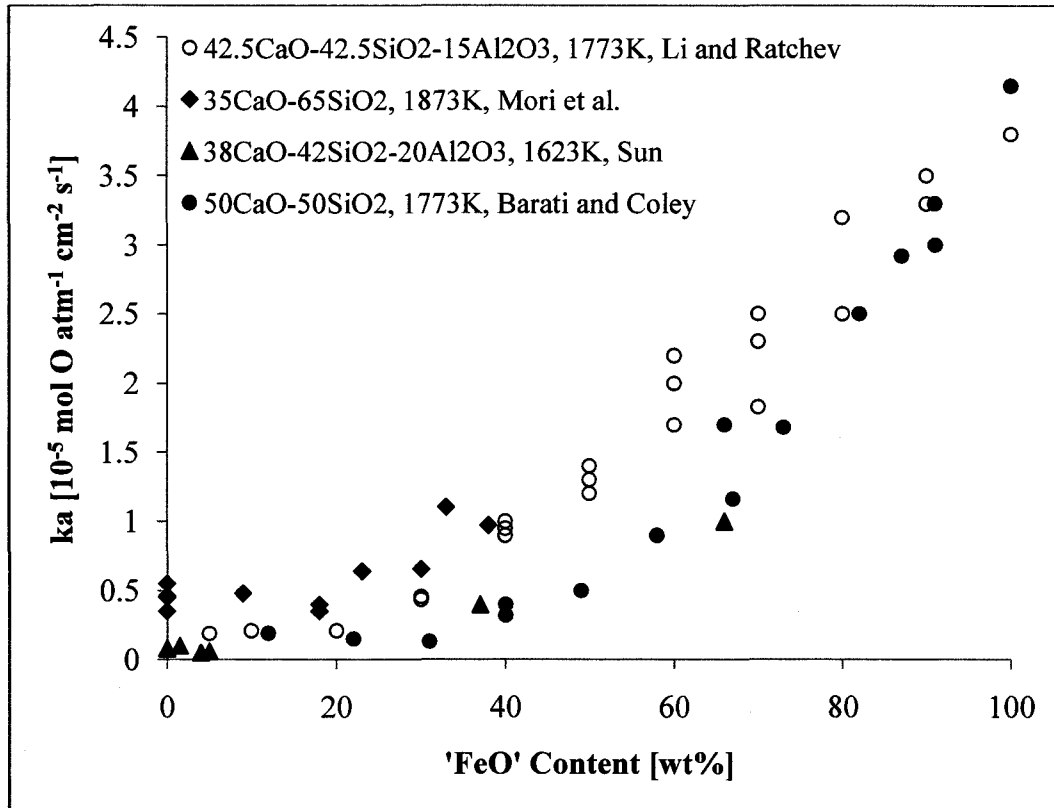
Figure 2.3 - Apparent rate constant of oxidation and reduction reaction as a function of iron oxide content, at unit CO_2/CO (Barati and Coley, 2005)

2.6.1.3 Effect of Bulk Slag Composition

Barati and Coley (2005) investigated the effect of slag basicity on the

apparent rate constant and compared their results with those of El-Rahaiby et al.

(1986), Li and Ratchev (2002), Mori et al. (1996). The data is reproduced in

Figure 2.4. All the results show that increasing basicity causes a considerable

increase in rate. Li and Ratchev (2002) and Barati and Coley (2005) explain this effect by considering the charge transfer mechanism. With reaction (2.44) as the rate-controlling step, the rate is proportional to the density of free electrons at the surface of the molten slag. Stronger basic oxides have a higher Fermi energy (Mullins, 1992), indicating a greater electrochemical potential of free electrons. Basic oxides cause an increase in rate, in proportion to their segregation at the slag surface and their degree of basicity, by causing a higher availability of electrons for the reaction.
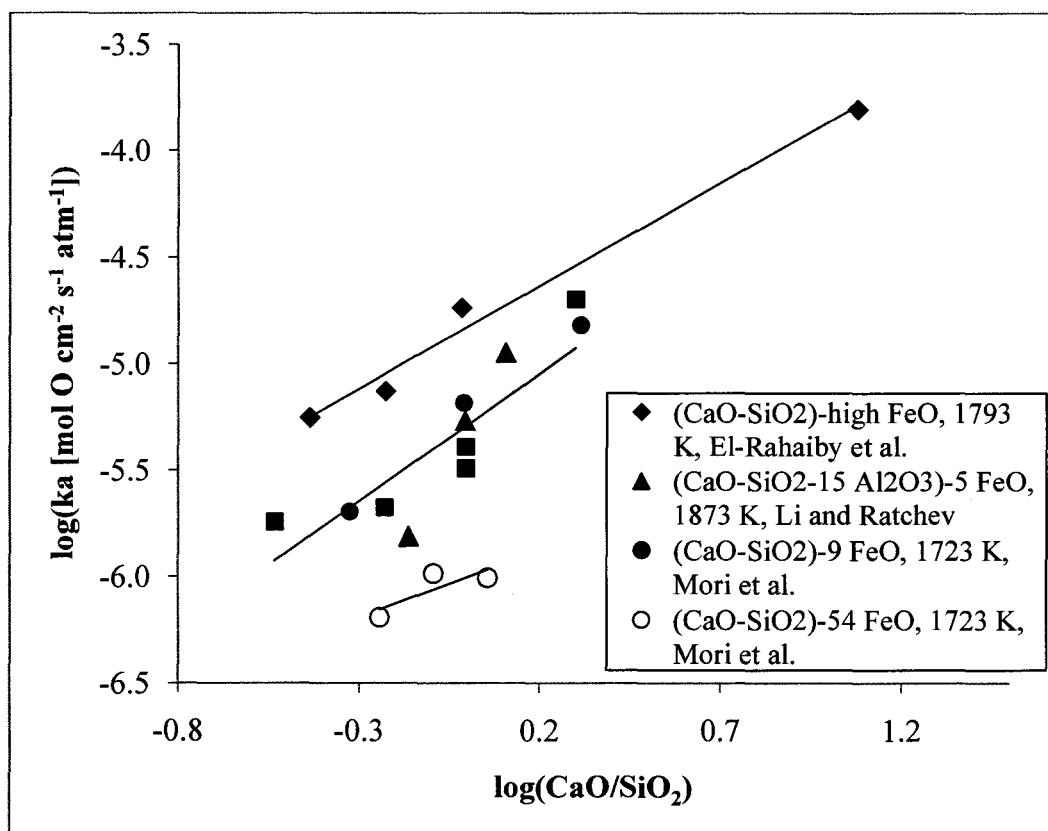
Figure 2.4 - Dependence of the apparent rate constant on the slag basicity at unit CO₂/CO (FeO in wt %) (Barati and Coley, 2005)

El-Rahaiby et al. (1986) suggest that surface-active species in the molten slag may affect the rate by blocking surface sites at higher concentrations. This decreases the number of surface sites available for CO_2 to adsorb and undergo charge transfer and thus decreases the rate of reaction. They investigated the influence of silica, a surface-active component in oxide melts, on the apparent rate constant in calcium iron silicates with unit CaO/'FeO' and found that increasing the concentration of silica caused a substantial decrease in the rate constant. This blockage of reaction sites by surface-active species is not by itself sufficient to explain the effect of bulk slag composition on the apparent rate constant, as the increase in electrochemical potential of free electrons caused by the addition of basic oxides is much more important. However, it may be useful to consider the surface morphology when highly surface-active species are present.

2.6.1.4 Effect of Temperature

El-Rahaiby et al. (1986) observed the apparent rate constant to depend on temperature according to equation (2.51) for slags of equimolar CaO and SiO_2 and with 'FeO' content ranging from 5 to 100 mol %.

$$\log k_a = -\frac{6900}{T} - 0.88 \tag{2.51}$$

From this equation the activation energy was calculated as 132 kJ mol^{-1}.

For slag with composition 40.4CaO-40.4SiO$_2$-14.2Al$_2$O$_3$-5'FeO' (wt %), Li and Ratchev (2002) observed the following dependence of the apparent rate constant on temperature:

$$\ln k_a = -\frac{19820}{T} - 1.699 \qquad (2.52)$$

From this equation the activation energy was calculated to be 165 kJ mol^{-1}.

Barati and Coley (2005) observed the activation energy to be 178 kJ mol^{-1} in slags with unit CaO/SiO$_2$, independent of iron oxide content. In slags with fixed 'FeO' content, increasing the molar basicity from 0.3 to 2.0 decreased the activation energy from 197 to 146 kJ mol^{-1}, which agreed with other studies and showed that increasing slag basicity decreases the activation energy of the reaction. This may also be explained in terms of the charge transfer mechanism (Barati and Coley, 2005). The adsorption of CO_3^{2-} ions is strengthened by the addition of basic oxides, decreasing the activation energy required for the formation of the CO_3^{2-} ion.

2.6.2 Kinetic Model

Barati and Coley (2006) have developed a comprehensive model for the prediction of the rate of reaction of CO$_2$-CO with CaO-SiO$_2$-FeO$_x$ slags. It is consistent with the observed effects of slag oxygen potential, iron oxide content, basicity and temperature on the rate as discussed above. It was developed considering the following reaction mechanism: CO$_2$ adsorption at the slag surface,

charge transfer to the adsorbed CO_2, and dissociation of CO_2^-. The rate determining step was the charge transfer and formation of the CO_2^- molecule. The apparent rate constant is related to temperature by an Arrhenius-type correlation with the pre-exponential and activation energy terms being functions of slag chemistry. The model was verified using experimental data from Li and Ratchev (2002), Matsuura et al. (2004) and Barati and Coley (2005) and the agreement was excellent considering different measurement techniques and experimental error. The model gives the apparent rate constant in units of [mol O cm^{-2} atm^{-1} s^{-1}] as

$$k_a = 2.67 \times 10^{-4} (C_{Fe})^2 \frac{1}{r(1+r)^2} \exp\left(\frac{-(475.7 - 452.4\Lambda)}{RT}\right) \qquad (2.53)$$

where C_{Fe} is the total iron concentration in the bulk slag in mol %, $r = Fe^{3+}/Fe^{2+}$ and Λ is the optical basicity of the slag.

2.7 Slag Foaming

Slag foaming is a case of one-dimensional two-phase flow, with liquid slag and gas bubbles flowing in the vertical direction in the steelmaking furnace. In EAF operation, the gas is a mixture of CO and CO_2 created by the reaction of iron oxide in the slag with carbon in the metal or solid carbon injected into the slag. It is important to achieve an optimum slag foam level early in the EAF heat and sustain the foam at the optimum level throughout the heat. Slag foaming has been extensively studied over the past two decades (Ito and Fruehan, 1989; Jiang

and Fruehan, 1991; Zhang, 1992; Ogawa et al., 1993; Zhang and Fruehan, 1995; Ozturk and Fruehan, 1995; Jung and Fruehan, 2000; Lahiri and Seetharaman, 2002; Lotun and Pilon, 2005) with the goal of quantifying the phenomenon and developing useful models that can be applied to optimize slag foaming in industry.

2.7.1 Foaming Index

Ito and Fruehan (1989) studied CaO-SiO$_2$-FeO slags in the temperature range of 1523 to 1673 K. This work instigated the application of the foaming index to metallurgical slags which has since been widely used in the modeling of slag foaming. The foaming index is defined as the ratio of foam height to superficial gas velocity. The superficial gas velocity is given by

$$V_g^s = \frac{Q_g}{A_c}$$

(2.54)

and foaming index by

$$\Sigma = \frac{\Delta h}{V_g^s}$$

(2.55)

where Q_g is the flow rate of gas through the slag and A_c is the cross-sectional area of the container. The foam height, Δh, is defined as the change in slag height from flat bath to steady-state foamed condition. The foaming index has units of seconds.

In order to make use of the foaming index it must be assumed that the foam height is linearly dependent on the superficial gas velocity. Ito and Fruehan (1989) observed the foaming index to be constant above a superficial gas velocity of 1.0 cm s^{-1} for 28.1CaO-41.9SiO$_2$-30FeO slags (wt %) at 1573 K for a range of crucible diameters from 25 to 50 mm, and concluded that the foaming index is a function of slag properties and independent of the superficial gas velocity. This conclusion was confirmed by the work of Ozturk and Fruehan (1995) and Zhang and Fruehan (1995). Ozturk and Fruehan (1995) found foam height to be linearly dependent on superficial gas velocity for 48CaO-32SiO$_2$-10-Al$_2$O$_3$-10FeO (wt %) slags at 1873 K with superficial gas velocities ranging from 0.50 to 1.50 cm s^{-1}. Zhang and Fruehan (1995) observed foam height to be linearly dependent on superficial gas velocity for slags with unit CaO/SiO$_2$ and 5 to 15 wt % FeO at 1773 K with gas injected through single- and multi-orifice nozzles for superficial gas velocities ranging from 0 to 6 cm s^{-1}.

The validity of the foaming index as an intrinsic property of the foaming solution has been questioned by Lotun and Pilon (2005). They argue that previous investigations into foaming index were performed for a limited range of physical and chemical properties and operating conditions, and that the foaming index does not account for the fact that slag foaming does not occur below a minimum superficial gas velocity.

2.7.2 Influence of System Properties on Foaming

Slag foam height and stability are heavily influenced by the viscosity and surface tension of the slag. Increasing slag viscosity slows the rate of liquid drainage from the foam, giving longer bubble residence time and increased foam height and stability. Reducing slag surface tension reduces the internal energy of the foam, which increases its stability and results in the formation of a larger number of small spherical bubbles as opposed to fewer, larger, polyhedral bubbles.

2.7.2.1 Bubble Type and Size

Bubbles may be formed by injection of gas into the slag through an aperture of given diameter, or more realistically, they may nucleate at a slag-metal or slag-solid carbon interface as the result of a gas-producing reaction. Zhang and Fruehan (1995) observed experimentally two distinct types of bubbles in slag foam: spherical and polyhedral. Bubbles generated by slag-metal interfacial reaction were small and spherical and those generated by argon gas injection through single- and multi-orifice nozzles were large and polyhedral. The foaming index increased with decreasing average bubble size as reproduced in Figure 2.5. Zhang and Fruehan (1995) altered the size of bubbles generated by slag-metal interfacial reaction by changing the concentration of sulphur, a highly surface-active species, in the metal. As sulphur content in the metal was increased, the surface tension in the metal decreased, increasing the contact angle for bubble nucleation and hence increasing bubble size. If bubbles are formed by chemical

reaction in the liquid, they tend to be small, spherical, and of uniform size and dispersion; if bubbles are formed by gas injection through a nozzle or perforated surface, the aperture at the formation site will determine their size (Lotun and Pilon, 2005).
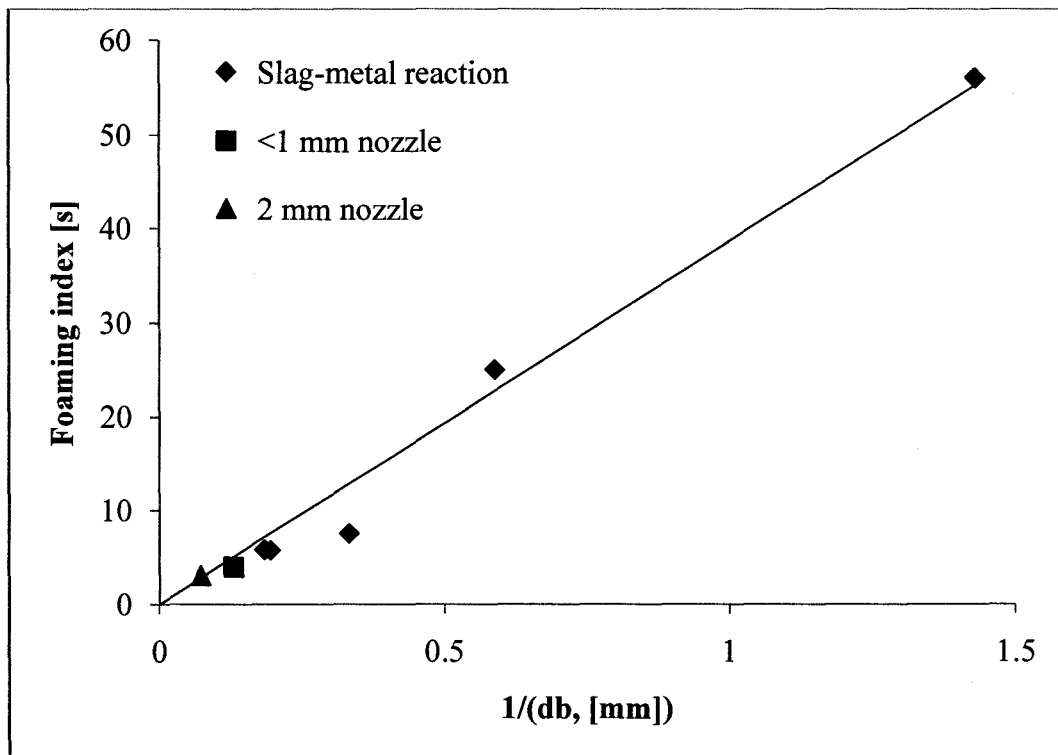
Figure 2.5 - Foaming index as a function of the reciprocal of average bubble diameter (Zhang and Fruehan, 1995)

Bubble size is related to the slag surface tension, so they should not be treated as independent variables. Reducing the surface tension of the slag reduces the internal energy of the foam and the energy required for bubble formation, resulting in a greater number of small spherical bubbles in slags with low surface

tension, as opposed to fewer, larger, polyhedron-shaped bubbles in slags with high surface tension. Lotun and Pilon (2005) collected data from a number of earlier studies and observed a clear dependency of average bubble size on surface tension as reproduced in Figure 2.6.
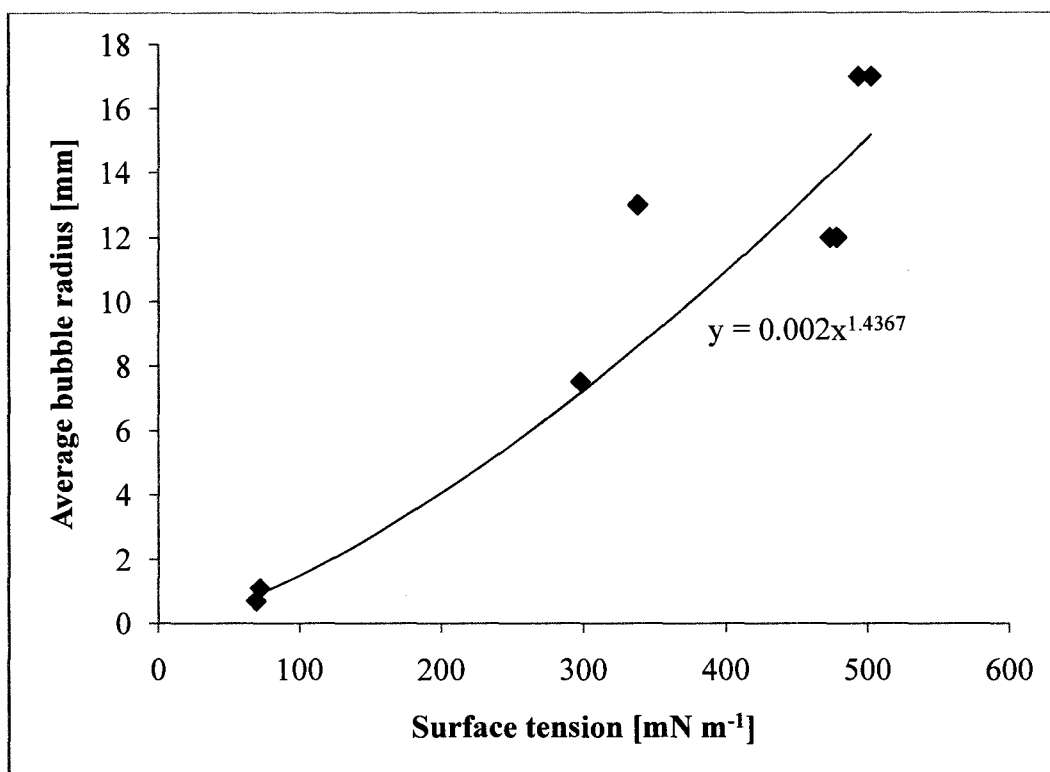
Figure 2.6 - Variation of the average bubble radius with surface tension (Lotun and Pilon, 2005)

2.7.2.2 Temperature

The effect of temperature on slag foaming was studied by Ozturk and Fruehan (1995) using a slag with composition $48CaO-32SiO_2-10Al_2O_3-10FeO$ (wt %) and bubbles generated by injection of argon gas through an alumina tube

with an aperture diameter of 1.57 mm. The temperature coefficient for surface tension of the slag was found to be positive and that for viscosity of the slag was found to be negative. Figure 2.7 shows that the natural logarithms of both foaming index and viscosity decrease linearly with temperature. Viscosity of the slag was calculated using Urbain's model (Urbain, 1987). From the data given in Figure 2.7, Ozturk and Fruehan (1995) determined the temperature dependence of the foaming index for their slag and experimental conditions to be:

$$\Sigma = 1.78 \times 10^{-5} \exp\left[\frac{16797}{T}\right] \tag{2.56}$$

From equation (2.56) the apparent activation energy for the decay of foam was calculated as 139.6 kJ mol^{-1}. The activation energy for the viscous flow was calculated from the slope of the line for viscosity in Figure 2.7 as 144.7 kJ mol^{-1}, which was within experimental error of the value for foam decay.
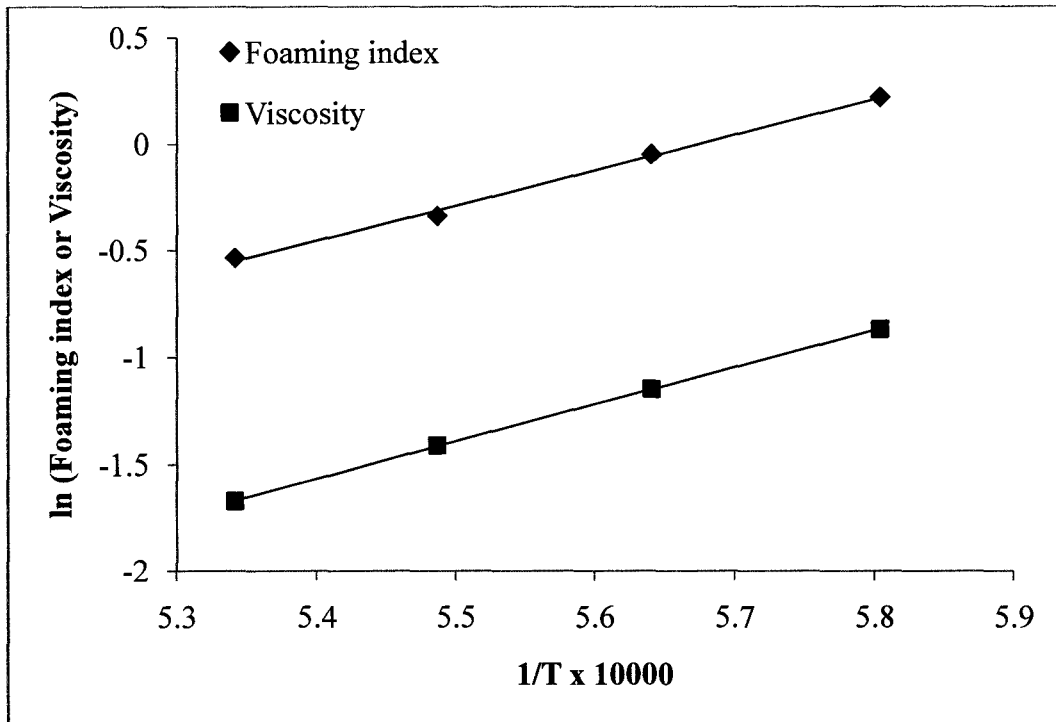
Figure 2.7 - Temperature dependency of foaming index and viscosity (Ozturk and Fruehan, 1995)

2.7.2.3 Slag Composition

Ito and Fruehan (1989) found that foaming index decreased with increasing basicity, with basicity defined as $CaO/(SiO_2 + Al_2O_3)$ in wt %. They explained this in terms of slag surface tension and viscosity. In CaO-SiO_2-Al_2O_3-FeO slags, higher basicity results in higher surface tension and lower viscosity, increasing liquid drainage rate and de-stabilizing the foam. Also, the addition of a small amount of a highly surface-active species such as P_2O_5, Cr_2O_3, or V_2O_5 to slag will increase the foaming index significantly by reducing the bulk surface tension of the slag.

Ito and Fruehan (1989) also noted that the foaming index increased with increasing concentration of second-phase particles, either added or precipitated. They concluded that this was due to an increase in effective viscosity of the slag. One of the following modified Einstein equations given by Brinkman (1952) and Happel (1957), respectively, may be used to determine the effective viscosity of the slag, μ_{eff}, as a function of volumetric fraction of second-phase particles, where μ is the viscosity of the liquid slag and ε is the volumetric fraction of solid particles.

$$\mu_{eff} = \mu(1 + 5.5\varepsilon) \tag{2.57}$$

$$\mu_{eff} = \mu(1 - \varepsilon)^{-2.5} \tag{2.58}$$

Solid phase particles such as $2CaO \cdot SiO_2$ precipitate at higher CaO contents, and thus at higher basicity. Ito and Fruehan (1989) found that increasing basicity decreased the foaming index until the liquidus composition of the slag was reached, and at CaO/SiO_2 ratios above the liquidus composition the foaming index increased due to higher effective viscosity caused by precipitation of solid particles.

In CaO-SiO_2-FeO slags, increasing FeO concentration lowers viscosity and decreases the volume fraction of precipitated second phase particles by changing the liquidus composition, both of which decrease the foaming index. However, from the broader perspective of the entire EAF process, the effect of

iron oxide content on slag foaming is more complex as demonstrated by a simulation performed by Ito and Fruehan (1989). FeO is a reactant in the gas production reaction, so increasing FeO content increases the rate of gas generation (provided there is sufficient carbon for the reaction) and in turn increases the foaming height. When a lack of carbon begins to inhibit gas production at higher FeO contents, increasing FeO content will no longer increase gas generation and the foaming height will decrease due to decreasing foaming index. Through their simulation, assuming that the reduction of FeO by carbon determines the gas velocity in the furnace, Ito and Fruehan (1989) found that maximum foaming height occurred at an iron oxide content of 25-30 wt % in a slag with CaO/SiO_2 equal to 3.0 and a temperature of 1873 K. This is illustrated in Figure 2.8, where S is the slag-carbon interfacial area and the A is cross-sectional area of the vessel.
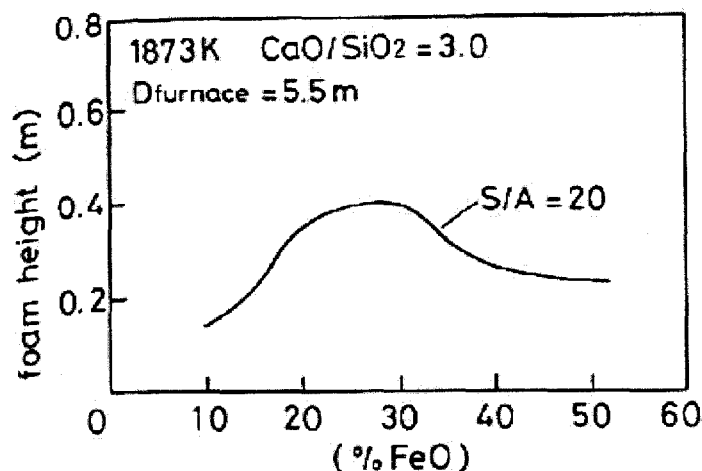
Figure 2.8 - Anticipated foaming height of the slag for an EAF operation as a function of FeO concentration (Ito and Fruehan, 1989)

2.7.3 Foaming Models

Using dimensional analysis, Ito and Fruehan (1989) developed the empirical relation for the foaming index given by equation (2.59). It is applicable to CaO-SiO$_2$-Al$_2$O$_3$-FeO slags with FeO content ranging from 10 to 60 wt % at temperatures from 1523 to 1673 K.

$$\Sigma = 570 \frac{\mu}{\sqrt{\sigma\rho}} \tag{2.59}$$

The terms μ, σ and ρ are slag viscosity, surface tension and density, respectively.

Jiang and Fruehan (1991) performed a dimensional analysis using their experimental results with bath smelting slags (CaO-SiO$_2$-MgO-Al$_2$O$_3$-FeO) at 1773 K as well as the results of Ito and Fruehan (1989). The relation developed is similar to the one from Ito and Fruehan and is given by equation (2.60).

$$\Sigma = 115 \frac{\mu}{\sqrt{\sigma\rho}} \tag{2.60}$$

Ogawa et al. (1993) developed a physical model from the results of cold and hot foaming experiments. It is quite complex, consisting of three separate models for 1) calculating the size of bubbles evolved at the slag-metal interface, 2) estimating the distribution of bubbles in the foam and 3) calculating the rate of film rupture at the top surface of the slag. Its purpose was to gain a more quantitative understanding of the phenomena involved in foam formation, not to predict foam heights in practice.

Zhang and Fruehan (1995) also used dimensional analysis and developed the following relation for foaming index:

$$\Sigma = 115 \frac{\mu^{1.2}}{\sigma^{0.2} \rho d_b^{0.9}} \qquad (2.61)$$

where d_b is the average bubble diameter. This relation gave good predictions over a foaming index range of 1 to 100 seconds for CaO-SiO_2-Al_2O_3-FeO slags with unit CaO/SiO_2 and FeO content ranging from 5 to 15 wt %, at temperatures of 1723 to 1773 K.

After concluding that the foaming index is not applicable in all situations, Lotun and Pilon (2005) developed a relation for the foam height Δh in terms of liquid properties and superficial gas velocity. They also utilized dimensional analysis and derived the following equation:

$$\frac{\Delta h}{0.5 d_b} = 2617 \frac{\mu^{0.73} j_r^{0.79} \sigma^{1.01}}{\rho^{1.74} g^{1.77} (0.5 d_b)^{3.51}} \qquad (2.62)$$

where d_b is the average bubble diameter at the bottom of the foam layer, g is the specific gravity of the liquid, and j_r is the reduced superficial gas velocity, defined as the difference between the superficial gas velocity and the minimum superficial gas velocity required for foam formation. The minimum superficial gas velocity can be estimated as a function of liquid properties (Pilon and Viskanta, 2004). Lotun and Pilon (2005) verified equation (2.62) using the experimental

data of a number of earlier studies on the foaming of high viscosity liquids and found agreement within 35% over a range of foam heights from 10 to 1000 mm.

Taking a different approach by not utilizing dimensional analysis, Lahiri and Seetharaman (2002) derived a mathematical model for the foaming index from the mechanism of liquid drainage and bubble rupture. They optimized the constant in their equation using least-squares fitting to the data of Zhang and Fruehan (1995) and Jung and Fruehan (2000). The final equation was:

$$\Sigma = 150\frac{\mu}{\rho d_b} \qquad (2.63)$$

This model predicted the foaming index very much like the relation from Zhang and Fruehan (1995).

2.8 Slag Physical Properties

2.8.1 Viscosity

A number of models for predicting the viscosity of metallurgical slags have been proposed for different slag systems (Riboud et al., 1981; Urbain et al., 1981; Urbain, 1987; Zhang and Jahanshahi, 1998; Iida et al., 2000; Kondratiev and Jak, 2001). Urbain's model (Urbain, 1987) has withstood the test of time, and has proven to be accurate for complex slag systems. It classifies all cations into three kinds of behaviour: network former, modifier, and amphoteric. This classification is empirical, but ensures the model's robustness over a wide range of possible slag systems. The viscosity is related to temperature by a simplified

expression based on the Weymann-Frenkel equation, given in (2.64), where A and B are empirical parameters. The models by Iida et al. (2000) and Kondratiev and Jak (2001) also make use of this formalism.

$$\mu = AT\exp\left[\frac{1000B}{T}\right] \tag{2.64}$$

The model by Urbain (1987) is summarised as follows. Network formers are cations which form polyanions in the tetrahedral position and include Si^{4+} and P^{5+}. Modifiers are associated with polyanions in the melt through charge balance and include cations Na^+, K^+, Mg^{2+}, Ca^{2+}, Fe^{2+}, Cr^{3+} and Ti^{4+}. Amphoteric cations may act as either network formers or modifiers depending on melt composition, and include Al^{3+} and Fe^{3+}. The viscosity μ in units of poise (0.1 Pa·s) is given by equation (2.64). The parameter A is related empirically to B through equation (2.65).

$$-\ln A = 0.29B + 11.57 \tag{2.65}$$

The parameter B is found by calculating the value of B for each of three ternary systems, SiO_2-Al_2O_3-MO where M is Mg, Ca or Mn, and computing a weighted average of these values with the mole fractions of the respective components in the real system. Thus,

$$B = \frac{X_{MgO}B_{MgO} + X_{CaO}B_{CaO} + X_{MnO}B_{MnO}}{X_{MgO} + X_{CaO} + X_{MnO}} \tag{2.66}$$

where

$$B_{\text{MgO}} = B_{0,\text{MgO}} + B_{1,\text{MgO}} \cdot X_g + B_{2,\text{MgO}} \cdot X_g^2 + B_{3,\text{MgO}} \cdot X_g^3 \qquad (2.67)$$

$$B_{i,\text{MgO}} = a(i)_{\text{Mg}} + b(i)_{\text{Mg}} \cdot \alpha + c(i)_{\text{Mg}} \cdot \alpha^2 \qquad i = 0, 1, 2, 3 \qquad (2.68)$$

$$B_{\text{CaO}} = B_{0,\text{CaO}} + B_{1,\text{CaO}} \cdot X_g + B_{2,\text{CaO}} \cdot X_g^2 + B_{3,\text{CaO}} \cdot X_g^3 \qquad (2.69)$$

$$B_{i,\text{CaO}} = a(i)_{\text{Ca}} + b(i)_{\text{Ca}} \cdot \alpha + c(i)_{\text{Ca}} \cdot \alpha^2 \qquad i = 0, 1, 2, 3 \qquad (2.70)$$

$$B_{\text{MnO}} = B_{0,\text{MnO}} + B_{1,\text{MnO}} \cdot X_g + B_{2,\text{MnO}} \cdot X_g^2 + B_{3,\text{MnO}} \cdot X_g^3 \qquad (2.71)$$

$$B_{i,\text{MnO}} = a(i)_{\text{Mn}} + b(i)_{\text{Mn}} \cdot \alpha + c(i)_{\text{Mn}} \cdot \alpha^2 \qquad i = 0, 1, 2, 3 \qquad (2.72)$$

The term X_g is the network former mole fraction, and the term α is related to the modifier mole fraction X_m and the amphoteric mole fraction X_a by:

$$\alpha = \frac{X_m}{X_m + X_a} \qquad (2.73)$$

The network former, modifier and amphoteric mole fractions are given by the following:

$$X_g = \frac{X_{\text{SiO}_2} + \frac{8}{5} X_{\text{P}_2\text{O}_5}}{X_{\text{SiO}_2} + \frac{8}{5} X_{\text{P}_2\text{O}_5} + X_{\text{CaO}} + X_{\text{MgO}} + X_{\text{FeO}} + X_{\text{MnO}} + X_{\text{Al}_2\text{O}_3} + X_{\text{Fe}_2\text{O}_3}} \qquad (2.74)$$

$$X_m = \frac{X_{\text{CaO}} + X_{\text{MgO}} + X_{\text{FeO}} + X_{\text{MnO}}}{X_{\text{SiO}_2} + \frac{8}{5} X_{\text{P}_2\text{O}_5} + X_{\text{CaO}} + X_{\text{MgO}} + X_{\text{FeO}} + X_{\text{MnO}} + X_{\text{Al}_2\text{O}_3} + X_{\text{Fe}_2\text{O}_3}} \qquad (2.75)$$

$$X_a = \frac{X_{Al_2O_3} + X_{Fe_2O_3}}{X_{SiO_2} + \frac{8}{5}X_{P_2O_5} + X_{CaO} + X_{MgO} + X_{FeO} + X_{MnO} + X_{Al_2O_3} + X_{Fe_2O_3}} \quad (2.76)$$

Table 2.2 lists the parameters a, b and c for the Mg, Ca and Mn systems.

Table 2.2 - Parameters a, b and c for the Mg, Ca and Mn systems (Urbain, 1987)

i	a(i)			b(i)			c(i)		
	Mg	Ca	Mn	Mg	Ca	Mn	Mg	Ca	Mn
0	13.2	13.2	13.2	15.9	41.5	20	-18.6	-45	-25.6
1	30.5	30.5	30.5	-54.1	-117.2	26	33	130	-56
2	-40.4	-40.4	-40.4	138	232.1	-110.3	-112	-298.6	186.2
3	60.8	60.8	60.8	-99.8	-156.4	64.3	97.6	213.6	-104.6

2.8.2 Surface Tension

Mills and Keene (1987) have developed a model for estimating the surface tension of slags based on the addition of partial molar contributions to surface tension by individual components. The partial molar surface tension of non-surface-active components may be assumed constant at a given temperature, and the partial molar surface tension of surface-active components can be modeled as functions of their composition. The slag surface tension σ is given by

$$\sigma = \sum_{i=1}^{n} X_i \bar{\sigma}_i \quad (2.77)$$

where X_i is the mole fraction of component i and $\bar{\sigma}_i$ is the partial molar surface tension of component i. Table 2.3 lists the partial molar surface tensions of non-surface-active components at 1773 K and Table 2.4 lists the equations for calculating the partial molar surface tension of surface-active components at 1773 K.

Table 2.3 - Partial molar surface tension for slag components at 1773 K (Mills and Keene, 1987)

Oxide	Al_2O_3	CaO	FeO	MgO	MnO	SiO_2	TiO_2
$\bar{\sigma}_i$ [mN m^{-1}]	655	625	645	635	645	260	360

Table 2.4 - Equations for calculating partial molar surface tension for selected surface-active slag components at 1773 K (Mills and Keene, 1987)

Oxide	$X_i\bar{\sigma}_i$ for X_i < N	N	$X_i\bar{\sigma}_i$ for X_i > N
Fe_2O_3	$-3.7 - 2972X_i + 14312X_i^2$	0.125	$-216.2 + 516.2X_i$
P_2O_5	$-5.2 - 3454X_i + 22178X_i^2$	0.12	$-142.4 + 167.5X_i$

The reported values of $d\sigma/dT$ for various slag systems were examined by Mills and Keene (1987) and a mean value of 0.15 mN m^{-1} K^{-1} was given as a temperature coefficient. Thus for temperatures other than 1773 K the surface tension in units of [N m^{-1}] is given by

$$\sigma = \sigma_{1773} + \left[\frac{0.15}{1000}(T - 1773)\right] \tag{2.78}$$

2.8.3 Density

The slag density can be calculated using the model given by Mills and Keene (1987) as follows. The molar volume of the slag can be calculated from the partial molar volume of each component:

$$V = \sum_{i=1}^{n} X_i \bar{V}_i \qquad\qquad (2.79)$$

where V is the molar volume of the slag, X_i is the mole fraction of component i, and $\bar{V}_i$ is the partial molar volume of component i. Slags containing SiO_2, Al_2O_3 and P_2O_5 consist of chains, rings and complexes. The structure, and therefore the molar volume, of these slags is dependent on the amount of the cations present. Thus the partial molar volume of these oxides must depend on composition. Using experimental data for change in molar volume with composition, Mills and Keene (1987) developed correlations for SiO_2 and Al_2O_3. The molar volume of P_2O_5 was found to be approximately independent of composition. Table 2.5 lists the recommended values for partial molar volume of various slag constituents at 1773 K.

Table 2.5 - Recommended values for partial molar volumes of various slag constituents at 1773 K (Mills and Keene, 1987)

Constituent	$\bar{V}$ [cm^3 mol^{-1}]
Al_2O_3	$28.31 + 32X_{Al_2O_3} - 31.45X_{Al_2O_3}^2$
CaF_2	31.3
CaO	20.7
FeO	15.8
Fe_2O_3	38.4
K_2O	51.8
MgO	16.1
MnO	15.6
Na_2O	33.0
P_2O_5	65.7
SiO_2	$19.55 + 7.966X_{SiO_2}$
TiO_2	24.0

To provide a temperature coefficient for molar volume values, Mills and Keene (1987) examined the temperature dependencies of the molar volumes (dV/dT) of a number of slag systems and adopted a mean value of 0.01% K^{-1}. Thus for temperatures other than 1773 K molar volume is given by

$$V = V_{1773} + \left[\frac{V_{1773}}{0.0001}(T - 1773) \right] \qquad (2.80)$$

Knowing the molar volume, the slag density ρ can then be calculated by the following expression:

$$\rho = \frac{\sum_{i=1}^{n} M_i x_i}{V} \tag{2.81}$$

where M_i is the molecular weight of component i.

2.9 Optical Basicity

The optical basicity of a slag is defined as the ratio of the electron donor power of the slag to the electron donor power of pure CaO. The optical basicity of a mixture of oxides can be easily calculated by adding the contribution from each component. The problem arises of accurately measuring the optical basicity of a component, and there is a fair degree of uncertainty in the literature about the correct value for many components, notably the oxides of transition metals.

The optical basicity of any slag can be calculated using an expression given by Sommerville and Yang (2001):

$$\Lambda = \sum_i X_i^e \Lambda_i \tag{2.82}$$

where X_i^e is the equivalent cation fraction and Λ_i is the optical basicity of oxide i. The equivalent cation fraction can be calculated as described by Sosinsky and Sommerville (1986) as follows:

$$X_i^e = \frac{X_i \times \text{number of oxygen atoms in molecule of oxide } i}{\sum_i (X_i \times \text{number of oxygen atoms in molecule of oxide } i)} \tag{2.83}$$

where X_i is the mole fraction of oxide i.

The optical basicity values of oxides from different scales taken from the review by Sommerville and Yang (2001) are summarized in Table 2.6. Barati and Coley (2006) approximated the optical basicity of 'FeO', the mixture of Fe_2O_3 and FeO, as 0.65.

Table 2.6 - Values of optical basicity of oxides (Sommerville and Yang, 2001)

Oxide	Λ derived from Pauling electronegativity	Λ derived from average electron density	Λ recommended by Sommerville and Yang
K_2O	1.40	1.15	1.40
Na_2O	1.15	1.10	1.20
Li_2O	1.07	1.05	1.05
BaO	1.15	1.08	1.10
SrO	1.07	1.04	1.05
CaO	1.00	1.00	1.00
MnO	0.59	0.95	0.95
FeO	0.51	0.93	0.93
MgO	0.78	0.92	0.85
Cr_2O_3	0.55	0.69	0.69
Fe_2O_3	0.48	0.69	0.69
Al_2O_3	0.61	0.68	0.65
TiO_2	0.61	0.64	0.65
B_2O_3	0.42	0.42	0.42
SiO_2	0.48	0.47	0.48
P_2O_5	0.40	0.38	0.40

2.10 Critical Assessment of the Literature

The slag-carbon reaction is described by equation (2.1) and the overall rate constant of the slag-carbon reaction is expressed by equation (2.4).

For the case of carbon reacting with slag of higher 'FeO' contents, liquid phase and gas phase mass transport become less important to the overall rate of reaction due to higher rates of gas evolution and the resulting stirring effect. Since the current work investigated systems which underwent violent stirring due to the gas-producing reaction, with slag containing at least 21 wt% 'FeO', it is probable that both gas phase and liquid phase mass transport had negligible effects on the rate.

Models for the carbon oxidation reaction have been presented by Turkdogan et al. and Story and Fruehan which show good agreement in their description of the intrinsic reaction kinetics. Story and Fruehan's model is applicable in the partial internal burning regime, which occurs at higher temperatures and larger carbon particle sizes. The current work was performed at relatively high temperatures ($\geq$ 1600°C) but with very small carbon particles (on the order of 0.2 mm), so it is likely that the carbon oxidation behaviour is described most accurately by Turkdogan's model in the complete internal burning regime.

The model proposed by Barati and Coley for the kinetics of CO_2-CO reacting with iron oxide-containing slags accurately predicts experimental data

over a wide range of conditions and was developed with thorough consideration of previous studies. The main drawback in applying this model to the current work is that it requires knowledge of the Fe^{3+}/Fe^{2+} ratio in the slag, which is difficult to measure experimentally and thus must be estimated using another model (Guo, 1984). Also, there is uncertainty in the literature about the optical basicity values of some slag components, which leads to some uncertainty about the model's accuracy.

Slag foaming is well-understood at least qualitatively. Numerous models for foam height have been developed which are applicable to steelmaking slags at appropriate temperatures, and under these conditions it appears that the foaming index is a useful parameter. The model by Lahiri and Seetharaman was derived from first principles instead of dimensional analysis and predicts experimental measurements well. For these reasons it is likely the best candidate for application to the current work.

Chapter 3: Experimental Work

3.1 Coal Injection Experiments

The experimental setup for the coal injection experiments is shown in Figure 3.1.

A – Gas sample port; B – Filter; C – Lance; D – Lid; E – Ceramic fibreboard; F – Steel rod; G – Slag; H – Steel; I – Feeder; J – Load cell; K – Flow rate transducer; L – Flow meter; M – A/D card terminal; N – High-MgO Crucible; O – Computer; P – Pressure transducer; Q – Graphite ring
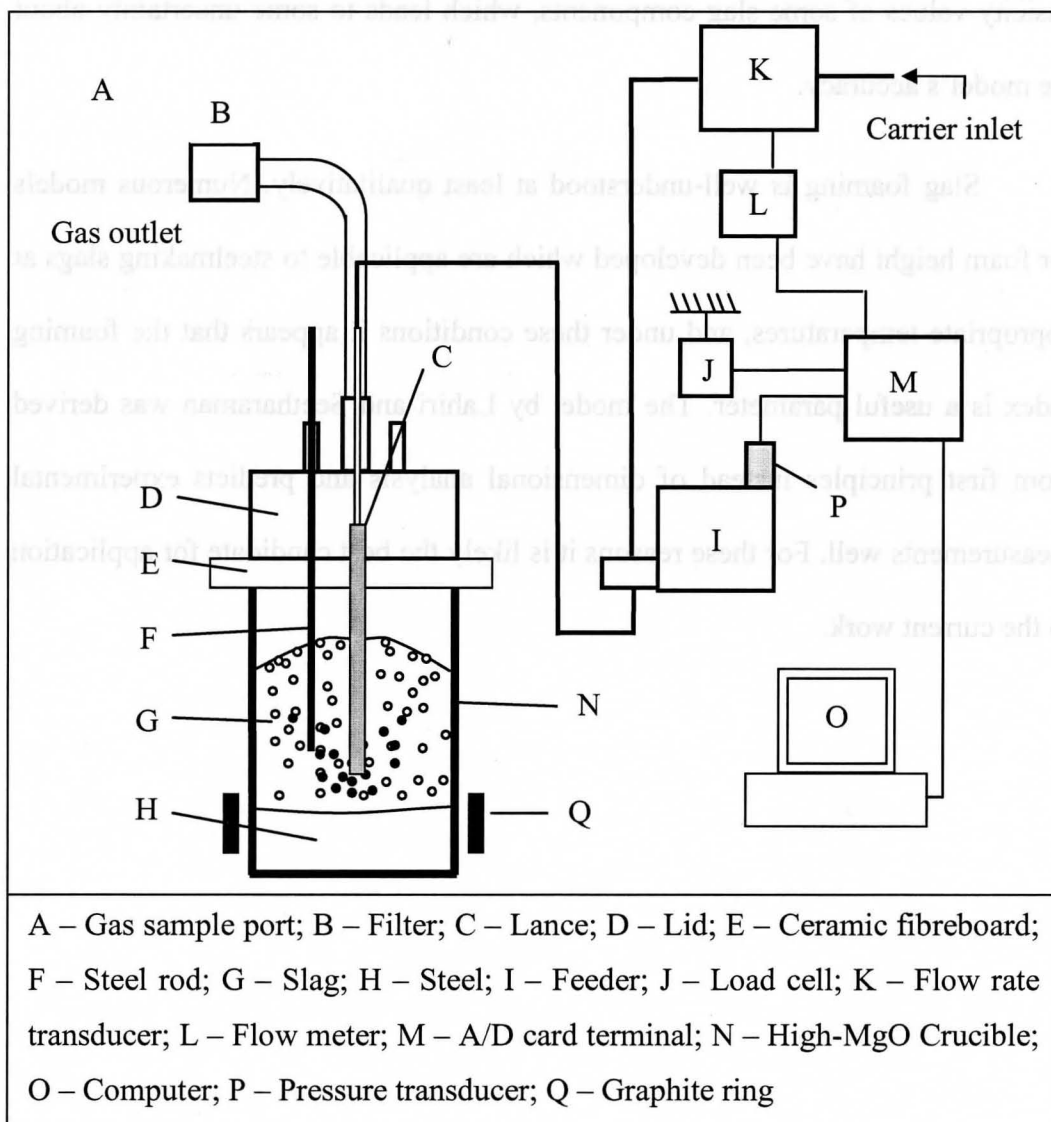
Figure 3.1 - Experimental setup

Experiments were carried out in a 75 kW induction furnace. A high-MgO crucible with interior diameter 191 mm and height 295 mm was used. Between 15 and 17 kg of steel was placed in the crucible and melted. When the temperature reached about 1600°C the slag powder was added gradually to create molten slag. After the slag was completely melted the ceramic fibreboard and stainless steel lid were set in place over the crucible. The lance was then introduced into the crucible through holes in the lid and fibreboard for preheating while about 1 Nl/min was passed through it to purge the freeboard. A steel rod was placed in contact with the surface of the slag bath to measure the height of the slag upon foaming. Immediately before the injection started, the nitrogen flow rate was increased to between 6.75 and 10.2 Nl/min. During injection, nitrogen was passed through a flow meter and was then introduced into the coal feeder. The feeder was suspended from a load cell to monitor the mass of injected coal. The pressure in the feeder was monitored by a pressure transducer mounted on the cover of the feeder. Gas from the crucible was exhausted through a single outlet. Gas samples were withdrawn using gas-tight syringes through a port mounted on the outgoing gas line. A filter fitted with a fine screen and glass wool was used for collecting dust. The first gas sample was taken when the carrier gas flow rate reached steady state. Coal injection was started after the first gas sample was taken. After coal injection had started, gas samples were taken as often as possible. Metal and slag samples were taken before, during and after injection. To investigate the vertical distribution of carbon in the slag, slag samples were taken at different depths

simultaneously. The signals of carrier gas flow rate, outgoing gas composition ($\%CO_2$, $\%CO$, and $\%O_2$) measured by another set of gas analysers, internal pressure of the feeder, and weight of coal were collected by a computer at 0.5 second intervals.

3.2 Experimental Materials

3.2.1 Metal

The metal used was low carbon steel, 0.003 wt % C, obtained from Dofasco in Hamilton, Ontario, Canada.

3.2.2 Slag

The slag was prepared by mixing oxide powders, namely calcium oxide, mill scale, calcined alumina, magnesite, and silica quartz sand. The composition of the oxide powders is given in Table 3.1. After the oxides were weighed they were mixed carefully and kept in a dry container.

Table 3.1 - Oxide powder detailed compositions

Wt %	Calcium oxide	Mill scale	Calcined Alumina	Magnesite	Silica quartz sand
CaO	> 98.24	–	–	1.68	–
Al_2O_3	–	–	99.5	0.99	–
MgO	–	–	–	93.66	–
SiO_2	–	–	0.05	2.38	99
Iron (Fe)	< 0.1	–	–	–	–
FeO	–	51.8	–	–	–
Fe_3O_4	–	45.9	–	–	–
Fe_2O_3	–	–	0.05	1.29	–
Chloride (Cl)	< 0.005	–	–	–	–
Nitrate (NO_3)	< 0.05	–	–	–	–
Sulphate (SO_4)	< 0.1	–	–	–	–
Heavy metals (as Pb)	< 0.004	–	–	–	–
Na_2O	–	–	0.35	–	–

3.2.3 Coal

3.2.3.1 Dofasco Coal

The coal used for injection experiments 16, 22, 24, 32, 33 and 34R was obtained from Dofasco in Hamilton, Ontario, Canada. Its composition, as shown in Table 3.2, was analysed by F.-Z. Ji at McMaster University using the method given by Harrison (1979). The volatile composition was approximated using a typical coke oven gas composition as given by Platts on the American Coke and

Coal Chemicals Institute website, shown in Table 3.3. Applying this volatile composition it was possible to calculate the detailed coal composition, given in Table 3.4.

   Table 3.5 gives the size distribution of the Dofasco coal, obtained via mesh screening by F.-Z. Ji at McMaster University in June 2001.

Table 3.2 - Dofasco coal composition as analysed

	Fixed Carbon	Volatile	Ash	Sulphur	Moisture
wt %	90.52	3.88	3.96	0.49	1.15

Table 3.3 - Coke oven gas composition used to approximate volatile composition (Platts)

	Actual composition (water saturated at 176°F) [%]	Dry basis [%]
Water vapour (H_2O)	47	0
Hydrogen (H_2)	29	55
Methane (CH_4)	13	25
Nitrogen (N_2)	5	10
Carbon Monoxide (CO)	3	6
Carbon Dioxide (CO_2)	2	3
Hydrocarbons (C_2H_6, C_3H_8)	1	2

Table 3.4 - Detailed composition of Dofasco coal

	Carbon	H_2	N_2	CO	CO_2	Ash	Sulphur	Moisture
wt %	91.72	0.75	0.93	0.56	0.44	3.96	0.49	1.15

Table 3.5 - Dofasco coal size distribution

Mesh	SI, mm	Mass % (screening time 5 min.)	Mass % (screening time 20 min.)	Mean Mass %	Cumulative Mean Mass %
<200	<0.074	4.36	4.54	4.45	4.45
200-140	0.074-0.104	6.03	6.30	6.17	10.62
140-80	0.104-0.177	24.01	24.14	24.08	34.69
80-50	0.177-0.297	49.08	47.58	48.33	83.02
50-30	**0.297-0.595**	**9.95**	**10.79**	**10.37**	**93.39**
30-16	0.595-1.190	1.97	2.04	2.01	95.40
16-8	1.190-2.360	4.60	3.08	3.84	99.24
>8	>2.360	0	1.53	0.77	100.00

3.2.3.2 Nucor Coal

The coal used for injection experiment "Nucor 1" was obtained from Nucor Steel in Auburn, New York, USA. Its composition was provided by Nucor Steel and its detailed composition was calculated using a typical coke oven gas composition (Platts) in the same manner as for the Dofasco coal. Its detailed composition is given in Table 3.6 and its size distribution, also obtained via mesh screening by F.-Z. Ji at McMaster University, is given in Table 3.7.

Table 3.6 - Detailed composition of Nucor coal

	Carbon	H_2	N_2	CO	CO_2	Ash	Sulphur	Moisture
wt %	82.81	1.46	1.81	1.09	0.85	8.74	1.85	1.38

Table 3.7 - Nucor coal size distribution

Mesh	SI, mm	Mass [g]	Mass %	Cumulative Mass %
<200	<0.074	9.8093	6.344	6.344
200-120	0.074-0.125	15.2357	9.853	16.196
120-80	0.125-0.18	35.4601	22.932	39.128
80-48	0.18-0.3	27.4106	17.726	56.854
48-28	**0.3-0.59**	**16.0665**	**10.390**	**67.244**
28-14	0.59-1.19	25.8986	16.748	83.992
14-8	1.19-2.36	20.2578	13.100	97.092
>8	>2.36	4.4961	2.908	100.000

3.2.3.3 Average Coal Size

For injection experiments 16, 22, 24, 32, 33 and 34R, in which the Dofasco coal was used, coal smaller than 30 mesh (< 0.595 mm) was used. For injection experiment "Nucor 1", in which the Nucor coal was used, coal smaller than 28 mesh (< 0.59 mm) was used.

The average injected particle diameter d_p° was estimated by dividing the summation of the average mesh size multiplied by the mass % at that size by the summation of the mass % of all sizes, as expressed in the following formula:

$$d_p^\circ = \frac{\sum \left(\frac{SI_1 - SI_2}{2}\right) \times mass\,\%}{\sum mass\,\%}$$

(3.1)

The average injected particle size was calculated to be 0.216 mm for the Dofasco coal and 0.202 mm for the Nucor coal.

3.2.4 Carrier Gas

The carrier gas was HP Plus (99.998 % N_2) nitrogen.

3.3 Gas and Slag Analysis

Gas samples taken by syringe were analyzed using a Perkin Elmer Autosystem XL Gas Chromatograph. Chemical analysis of the slag was carried out using an X-ray fluorescence (XRF) technique or, for later experiments, an ICP-OES system.

3.4 Experimental Errors

It was observed in the injection experiments that the coal injection rate was not always constant over time. The injection lance sometimes became blocked by frozen slag or by sticking coal, resulting in a pressure build-up in the feeder and a sudden large influx of carbon into the slag when the pressure became great enough to blow out the blockage. This would result in a lower rate of carbon gasification than expected during the blockage and a spike in the gasification rate when the sudden large influx of coal occurred. Since a constant injection rate was assumed, this uncertainty in the actual injection rate made it difficult to experimentally determine the residual amount of carbon in the slag.

Flotation of injected coal on the top of the slag was also observed. Coal is not easily wetted by slag and thus if it is not injected into a sufficient volume of

liquid slag it will not be immersed. This especially may be an issue if the slag is highly foamed with a large void fraction, which always was the case after a spike in gasification rate caused by blocking and clearing of the injection lance. Floating coal would react at a much slower rate in the inert (relative to the carbon) atmosphere in the freeboard compared to coal immersed in the slag. This would result in lower gasification rates and higher residual carbon amounts than expected.

Uncertainties were present in the amount of carbon injected, represented by $\delta(\text{C Inj})$. The coal volatile composition was not known and was estimated by a typical coke oven gas composition. Also, a small amount of the injected carbon was lost, before reacting with the slag, because it reacted with the steel or was blown out of the crucible with the off-gas. It was estimated that 0.3 g of coal reacted with the steel and 0.2 g of coal was lost to the off-gas for each experiment.

There was a small amount of error inherent in the analysis of the gas and slag samples. The uncertainties in the gas sample analysis are represented by $\delta(\%CO_2)$, $\delta(\%O_2)$, $\delta(\%N_2)$, $\delta(\%CO)$, and $\delta(\%H_2)$. The uncertainty in the flow rate of the carrier gas is represented by $\delta(Q_{N_2})$.

The uncertainty in the measurement of the carbon gasification rate may be expressed by

$$\delta(Q_C) = \left| \frac{\partial(Q_C)}{\partial(C \, Inj)} \right| \delta(C \, Inj) + \left| \frac{\partial(Q_C)}{\partial(Q_{N_2})} \right| \delta(Q_{N_2}) + \left| \frac{\partial(Q_C)}{\partial(\%CO_2)} \right| \delta(\%CO_2)$$

$$+ \left| \frac{\partial(Q_C)}{\partial(\%O_2)} \right| \delta(\%O_2) + \left| \frac{\partial(Q_C)}{\partial(\%N_2)} \right| \delta(\%N_2) + \left| \frac{\partial(Q_C)}{\partial(\%CO)} \right| \delta(\%CO)$$

$$+ \left| \frac{\partial(Q_C)}{\partial(\%H_2)} \right| \delta(\%H_2) \qquad\qquad (3.2)$$

The calculated uncertainty in the carbon gasification rate is about 5%. This degree of uncertainty is consistent with observed experimental scatter.

The estimated uncertainty in the measured slag foam height is 15% and the estimated uncertainty in the measured average slag bubble diameter is 20%.

Chapter 4: Experimental Analysis and Results

4.1 Slag-Carbon Reaction Mechanism

The slag-carbon reaction mechanism is shown schematically in Figure 4.1. The carbon becomes entrained in the slag and a gas film or possibly a number of gas bubbles develop around the carbon particle from the gas-producing reaction. It is not clear whether the bubble or bubbles remain attached to the carbon particle for its entire lifetime in the slag.
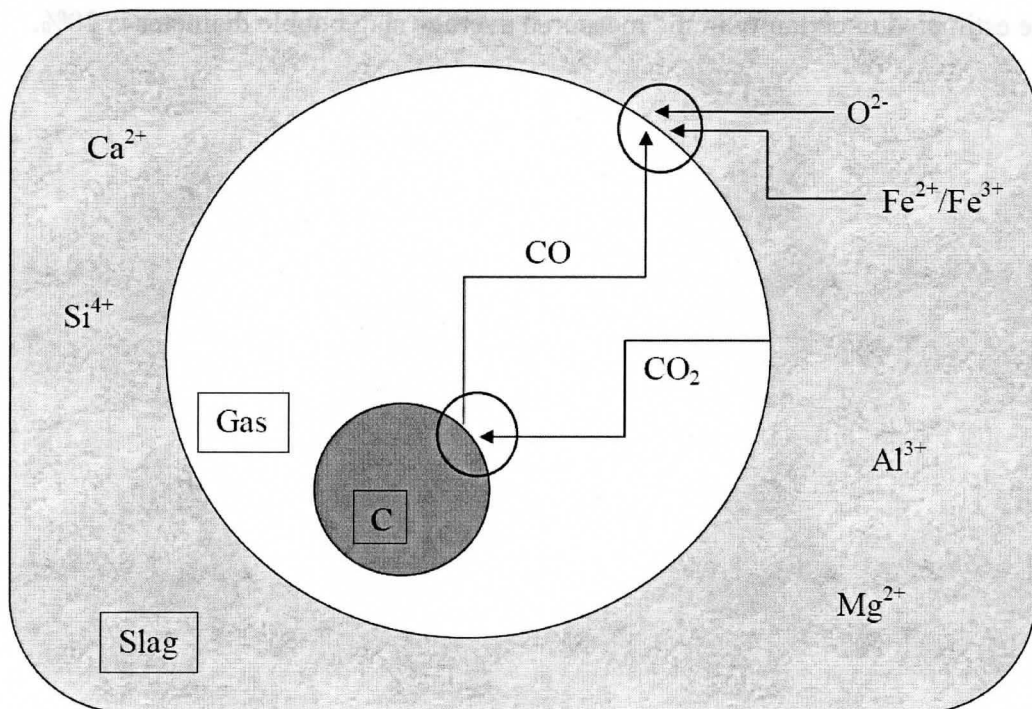
Figure 4.1 - Schematic representation of the carbon-gas and slag-gas reactions

4.2 Calculation of the Slag-Carbon Reaction Rate

Assuming some degree of post-combustion, according to the reaction

$CO + 0.5O_2 = CO_2$, occurs in the lid before the gas reaches the analysis

equipment it is necessary to determine the composition of the gas reacting with

the carbon and slag before post-combustion. If the overall slag-carbon reaction is

under mixed control by the chemical reactions at the slag-gas and carbon-gas

interfaces, the partial pressures of reacting gases (CO_2 and CO) in the gas film

between the solid carbon and slag should be somewhere between their equilibrium

values at the slag-gas and carbon-gas interfaces.

4.2.1 The χ Parameter

The concept and method of application of the χ parameter was developed

by Ji et al. and discussed in their publications (Ji et al., 2002, 2003, 2004, 2005a

and 2005b). Their work is summarised here.

At the slag-gas interface the reaction is given by either equation (4.1) or

(4.2),

$$(Fe^{3+}, 1.5O^{2-}) + 0.5CO = (Fe^{2+}, O^{2-}) + 0.5CO_2 \qquad p_{CO_2}^s \qquad (4.1)$$

$$(Fe^{2+}, O^{2-}) + CO = Fe + CO_2 \qquad p_{CO_2}^s \qquad (4.2)$$
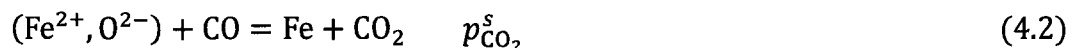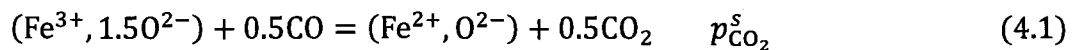
Equilibrium between Fe^{2+} and Fe, as described by equation (4.2), exists at the

steel-slag interface or at the interface between slag and iron droplets in the slag.

The reaction time between the carbon particles and the slag is relatively short, so

it is unlikely that Fe is reduced out of the slag. This has been confirmed experimentally by melting a small amount of copper into the metal bath as a tracer. Metal droplets found in the slag invariably contained copper, indicating that they originated from the metal bath and were entrained in the slag possibly as a result of violent foaming. Thus it is reasonable to assume that the equilibrium at the slag-gas interface is between Fe^{3+}, Fe^{2+}, CO and CO_2 as described by equation (4.1).

At the carbon-gas interface the reaction is:

$$C + CO_2 = 2CO \qquad p_{CO_2}^C \tag{4.3}$$

Reactions at the slag-gas and carbon-gas interfaces cannot both be at equilibrium. Reaction time is relatively short, being limited by the residence time of the carbon particle in the slag, so probably neither is at equilibrium. The actual partial pressure of CO_2 in the gas phase, here referred to as $p_{CO_2}^\chi$, should be between the two equilibrium partial pressures and closer to that of the faster of the two reactions. Assuming the gas phase is uniform, the parameter χ is introduced:

$$p_{CO_2}^\chi = \chi p_{CO_2}^s + (1 - \chi) p_{CO_2}^C \tag{4.4}$$

Isolating for χ yields:

$$\chi = \frac{p_{CO_2}^\chi - p_{CO_2}^C}{p_{CO_2}^s - p_{CO_2}^C} \tag{4.5}$$

The equilibrium CO_2/CO ratio at the carbon-gas interface, $p_{CO_2}^C/p_{CO}^C$, is a function

of temperature. Assuming that the slag-gas reaction is given by equation (4.1), the

equilibrium CO_2/CO ratio at the slag-gas interface, $p_{CO_2}^S/p_{CO}^S$, is a function of

temperature, Fe^{3+}/Fe^{2+} ratio in the slag and bulk slag composition. The parameter

χ at a fixed temperature can be interpreted schematically as in Figure 4.2.
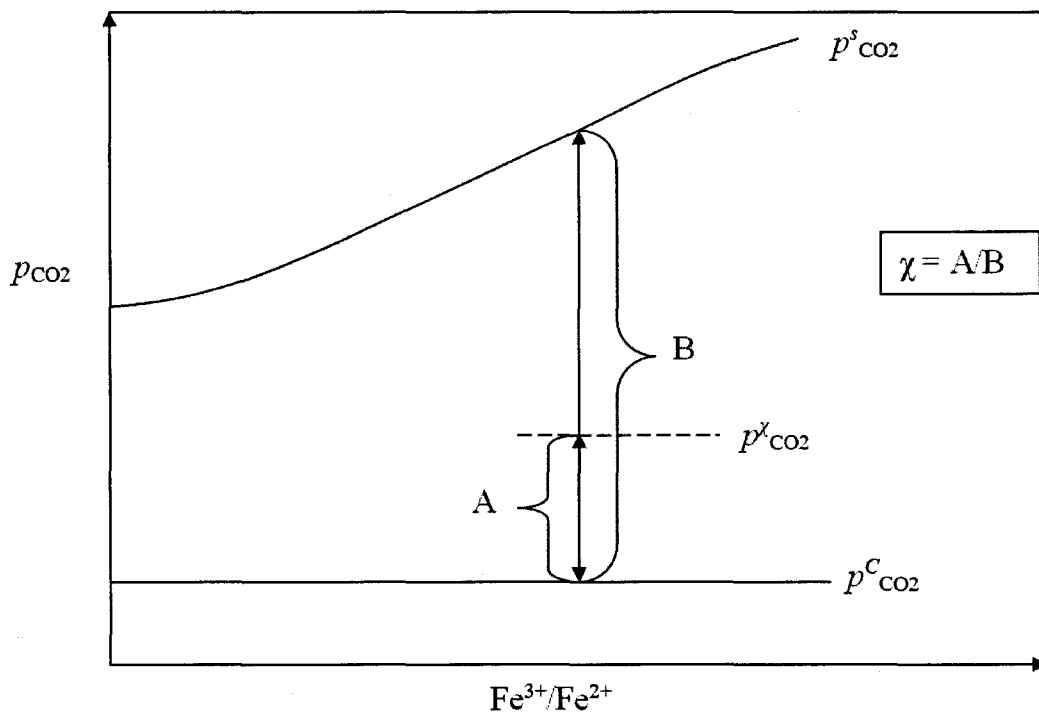
Figure 4.2 - Schematic interpretation of the χ parameter

4.2.2 Model for the Fe^{3+}/Fe^{2+} Ratio in the Slag (Guo, 1984)

A model which describes the Fe^{3+}/Fe^{2+} ratio as a function of temperature

and slag composition has been developed by Guo (1984) for a system very similar

to the experimental conditions under investigation here. At a fixed temperature,

the ratio of Fe_2O_3/FeO in wt % can be shown to be a linear function of CaO

content in pure iron oxide slags and a linear function of SiO_2 content in iron oxide

slags saturated with CaO (Guo, 1984). According to Guo (1984) the influence of

the concentration of slag components on the ratio Fe_2O_3/FeO can be expressed as

$$\frac{Fe_2O_3\ (wt\ \%)}{FeO\ (wt\ \%)} = A + \sum_i B_i(C_i\ (wt\ \%)) \tag{4.6}$$

The term A gives the ratio of Fe_2O_3/FeO in pure iron oxide as a function of

temperature. It is determined by the following equations.

$$\frac{X_O}{X_{Fe}} = 0.8541 + \frac{296.7}{T} \tag{4.7}$$

$$\frac{X_{Fe_2O_3}}{X_{FeO}} = \frac{\frac{X_O}{X_{Fe}} - 1}{3 - 2\frac{X_O}{X_{Fe}}} \tag{4.8}$$

$$A = \left(\frac{Fe_2O_3}{FeO}\right)_{iron\ oxide} = \frac{X_{Fe_2O_3}}{X_{FeO}} \times \frac{M_{Fe_2O_3}}{M_{FeO}} \tag{4.9}$$

Thus,

$$A = \frac{\left(0.8541 + \frac{296.7}{T}\right) - 1}{3 - 2\left(0.8541 + \frac{296.7}{T}\right)} \times \frac{M_{Fe_2O_3}}{M_{FeO}} \tag{4.10}$$

The values of B_i for different slag components are given in Table 4.1.

Table 4.1 - B_i values for different slag components (Guo, 1984)

Component	B_i
CaO	0.0073
MgO	0.0066
MnO	0.001
SiO$_2$	-0.007
P$_2$O$_5$	-0.0074

The experimental data of Winkler and Chipman (1946) were used by Guo (1984) to examine the validity of the model, and the agreement is quite good as shown in Figure 4.3. The experimental setup of Winkler and Chipman (1946) was very similar to the one used in the current work, which establishes confidence that the model given by Guo (1984) can be successfully applied to the current situation. The experimental heats of Winkler and Chipman (1946) were made by melting 65 lbs of ingot iron by radiant heat from an arc drawn between two carbon electrodes suspended within the crucible above the bath, in a vacuum to reduce the carbon content to below 0.01 %. The crucible used was MgO. A mixture of oxides was added to create a synthetic slag which covered the surface of the metal bath. A nitrogen atmosphere at positive pressure was maintained in the furnace. Slag and metal samples were taken by split steel molds dipped into the bath. The setup is similar to the conditions in this work in that an MgO crucible was used, the slag was in equilibrium with liquid iron at the metal-slag interface, and the atmosphere was nitrogen at positive pressure.
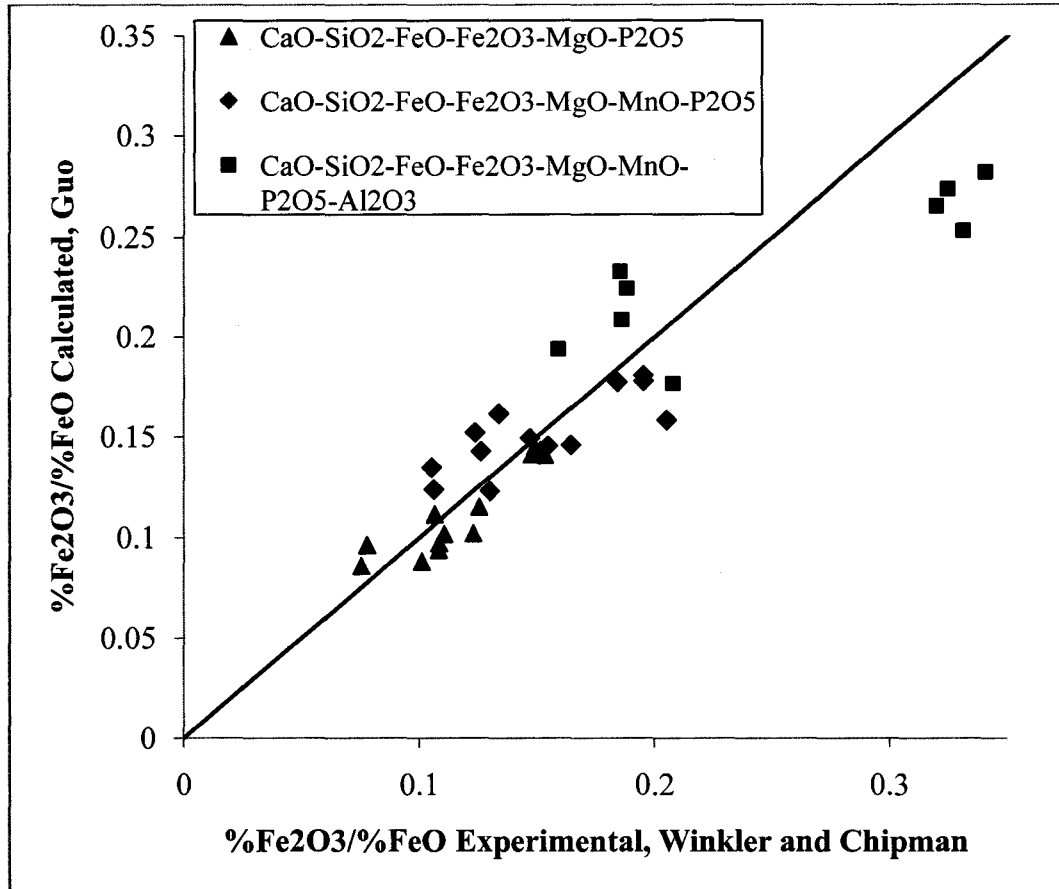
Figure 4.3 - Comparison of calculated and experimentally observed values of %Fe₂O₃/%FeO (Guo, 1984; Winkler and Chipman, 1946)

4.2.3 Model for Equilibrium CO₂/CO at the Slag-Gas Interface (Goel and Kellogg, 1984)

The thermochemical model proposed by Goel and Kellogg (1984) may be used to predict the iron redox equilibrium in iron-silicate slags containing lime. To use this model for the current application it must be assumed that minor slag constituents Al_2O_3, MgO, MnO, P_2O_3, etc. have negligible effect on the iron redox equilibrium.

The redox reaction of iron oxides in slags may be written as in equation (4.1), according to which the CO_2/CO ratio may be expressed by

$$\frac{p_{CO_2}}{p_{CO}} = \left(K \cdot \frac{Fe^{3+}}{Fe^{2+}} \cdot \frac{\gamma_{FeO_{1.5}}}{\gamma_{FeO}} \right)^2 \tag{4.11}$$

where K is the equilibrium constant of the slag-gas reaction.

The thermochemical model by Goel and Kellogg (1984) is summarised as follows. Formation equilibria for species are given by equations (4.12) to (4.17). Lines over the top denote hypothetical species.

$$Fe(l) + \frac{3}{4}O_2(g) = \overline{FeO_{1.5}} \qquad \ln K_1 = -12.8846 + \frac{44760}{T} \tag{4.12}$$

$$Fe(l) + \frac{1}{2}O_2(g) = \overline{FeO} \qquad \ln K_2 = -6.3763 + \frac{29471}{T} \tag{4.13}$$

$$Fe(l) = \overline{Fe} \qquad \ln K_3 = 0.0 \tag{4.14}$$

$$SiO_2(c) = \overline{SiO_2} \qquad \ln K_4 = 0.96864 - \frac{5970}{T} \tag{4.15}$$

$$CaO(c) = \overline{CaO} \qquad \ln K_5 = 0.6777 - \frac{3247}{T} \tag{4.16}$$

$$2CaO(c) + SiO_2(c) = \overline{(CaO)_2SiO_2} \qquad \ln K_6 = 4.4872 + \frac{4677}{T} \tag{4.17}$$
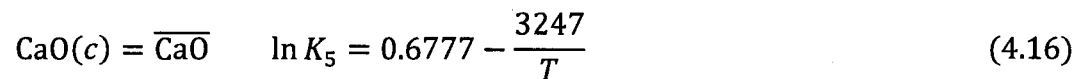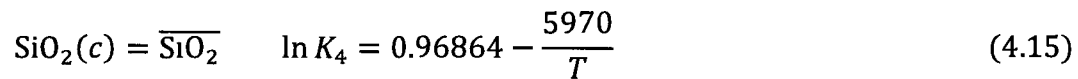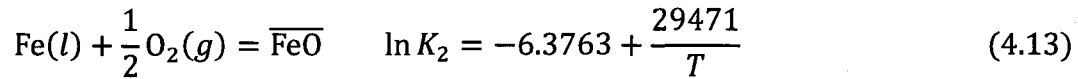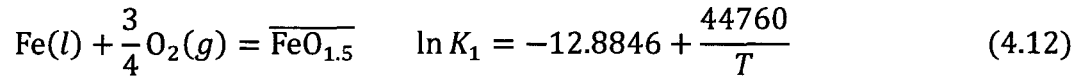
The non-ideal behaviour of the species is described by the three-suffix Margules equations with zero ternary interactions in the form

$$\ln \gamma_i = \frac{1}{2}\sum_j (k_{ij} + k_{ji})X_j - \frac{1}{2}\sum_j \sum_p k_{jp}X_j X_p + \sum_j (k_{ij} - k_{ji})X_j \left(\frac{X_j}{2} - X_i\right)$$

$$+ \sum_j \sum_p (k_{jp} - k_{pj})X_p X_j^2 \qquad (4.18)$$

where $k_{ii} = k_{jj} = k_{pp} = 0.0$, and the summations are carried over all species. These equations are fully consistent with the Gibbs-Duhem equation and obey Raoult's and Henry's laws as limiting laws. The temperature dependence of the Margules constants is described by the relation

$$k_{ij} = \frac{c_{ij}}{T} \qquad (4.19)$$

Table 4.2 lists the Margules constants c_{ij}.

Table 4.2 - Margules constants c_{ij} (Goel and Kellogg, 1984)

i/j	$\overline{FeO_{1.5}}$	$\overline{FeO}$	$\overline{Fe}$	$\overline{SiO_2}$	$\overline{CaO}$	$\overline{(CaO)_2SiO_2}$
$\overline{FeO_{1.5}}$	0	-1173	9882	-445	-7655	-5270
$\overline{FeO}$	-2461	0	9199	-11115	115	-129
$\overline{Fe}$	9882	7188	0	7376	8242	7376
$\overline{SiO_2}$	-147	-4165	7376	0	-18700	-13614
$\overline{CaO}$	-7655	115	8242	-29000	0	-344
$\overline{(CaO)_2SiO_2}$	-5270	-129	7376	-13614	-344	0

The model can be applied to calculate the Fe^{3+}/Fe^{2+} ratio as follows. From equation (4.13),

$$\overline{\text{FeO}} = \text{Fe}(l) + \frac{1}{2}\text{O}_2(g) \qquad \ln K_7 = 6.3763 - \frac{29471}{T} \tag{4.20}$$
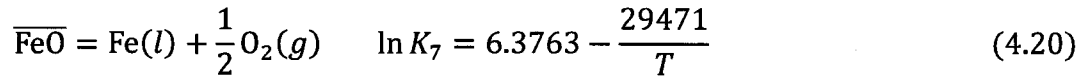
Gaskell (2003) gives the following formation equilibria for carbon monoxide and carbon dioxide:

$$\frac{1}{2}\text{C}(s) + \frac{1}{4}\text{O}_2(g) = \frac{1}{2}\text{CO}(g) \qquad \ln K_8 = 5.271 + \frac{6717.26}{T} \tag{4.21}$$

$$\frac{1}{2}\text{CO}_2(g) = \frac{1}{2}\text{C}(s) + \frac{1}{2}\text{O}_2(g) \qquad \ln K_9 = -0.0505 - \frac{23699.8}{T} \tag{4.22}$$
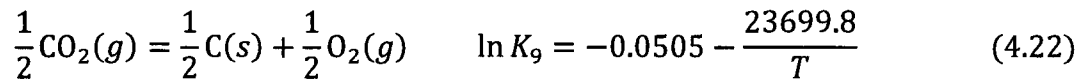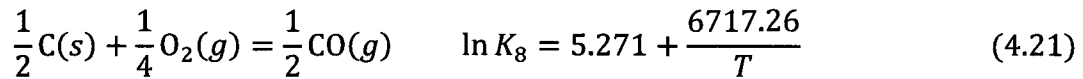
Combining equations (4.12), (4.20), (4.21) and (4.22) yields

$$\overline{\text{FeO}} + \frac{1}{2}\text{CO}_2(g) = \overline{\text{FeO}_{1.5}} + \frac{1}{2}\text{CO}(g) \qquad \ln\left(\frac{1}{K}\right) = -1.2878 - \frac{1693.54}{T} \tag{4.23}$$
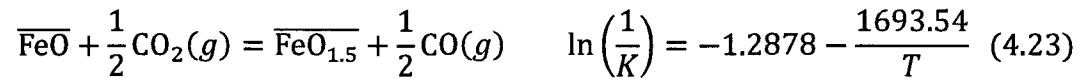
$$K = \exp\left[1.2878 + \frac{1693.54}{T}\right] \tag{4.24}$$

The activity coefficients of the oxides of iron, $\gamma_{\text{FeO}_{1.5}}$ and γ_{FeO}, may be calculated using the Margules equations. It is assumed that $p_{\text{CO}_2} + p_{\text{CO}} = 1$ in the gas phase at the slag-gas interface. Thus, equation (4.11) may be used to calculate p_{CO_2} at the slag-gas interface, that is, $p_{\text{CO}_2}^s$.

4.2.4 Accounting for Post-Combustion and the Carbon Mass Balance

The following method of analysing the off-gas composition to determine the carbon-slag reaction rate was developed by Ji et al. and is discussed briefly in a number of their publications (Ji et al., 2002, 2003, 2004 and 2005b), and in

more detail in one publication (Ji et al., 2005a). It has been expanded upon in this work.

It is assumed that the post-combustion reaction is given by equation (4.25), and that no hydrogen is reacted in post-combustion.

$$CO + 0.5O_2 = CO_2 \qquad (4.25)$$

The χ parameter is used to express the CO_2 content of the gas before post-combustion, $\%CO_2^\chi$, as given in equation (4.26),

$$\%CO_2^\chi = 100 \cdot p_{CO_2}^\chi = 100\left[\chi p_{CO_2}^S + (1 - \chi)p_{CO_2}^C\right] \qquad (4.26)$$

The term $\Delta\%CO_2$ is introduced and is defined as the difference between $\%CO_2$ after post-combustion and $\%CO_2$ before post-combustion, that is, the difference between the measured $\%CO_2$ in the off-gas and that calculated using the χ parameter:

$$\Delta\%CO_2 = \%CO_2 - \%CO_2^\chi \qquad (4.27)$$

After coal injection begins, the gas compositions before post-combustion should be:

$$O_2' = \frac{\%O_2 + 0.5\Delta\%CO_2}{\%CO + 1.5\Delta\%CO_2 + \%O_2 + \%N_2 + \%CO_2^\chi + \%H_2} \qquad (4.28)$$

$$N_2' = \frac{\%N_2}{\%CO + 1.5\Delta\%CO_2 + \%O_2 + \%N_2 + \%CO_2^\chi + \%H_2} \qquad (4.29)$$

$$CO' = \frac{\%CO + \Delta\%CO_2}{\%CO + 1.5\Delta\%CO_2 + \%O_2 + \%N_2 + \%CO_2^{\chi} + \%H_2} \tag{4.30}$$

$$CO_2' = \frac{\%CO_2^{\chi}}{\%CO + 1.5\Delta\%CO_2 + \%O_2 + \%N_2 + \%CO_2^{\chi} + \%H_2} \tag{4.31}$$

$$H_2' = \frac{\%H_2}{\%CO + 1.5\Delta\%CO_2 + \%O_2 + \%N_2 + \%CO_2^{\chi} + \%H_2} \tag{4.32}$$

where O_2', N_2', CO', CO_2', and H_2' are the modified volumetric fractions and $\%O_2$, $\%N_2$, $\%CO$, $\%CO_2$ and $\%H_2$ are the measured percentages in the gas sample.

At the hypothetical point after the gas has reacted with the slag and carbon but before it has undergone post-combustion the value of Q_C, the flow rate of CO + CO$_2$ from gasification of injected carbon, can be calculated as follows. The total gas flow rate, Q_Σ, is

$$Q_\Sigma = Q_{air} + Q_{N_2} + Q_C + Q_{H_2} \tag{4.33}$$

where Q_{air}, Q_{N_2} and Q_{H_2} are the flow rate of entrained air, the flow rate of N$_2$ from the coal and the carrier gas, and the flow rate of H$_2$ from the coal, respectively. It is assumed that the only source of O$_2$ in the system is entrained air, the only sources of N$_2$ in the system are entrained air, carrier gas and coal, and the only source of H$_2$ in the system is coal. Then the following can be written:

$$N_2' = \frac{0.79Q_{air} + Q_{N_2}}{Q_{air} + Q_{N_2} + Q_C + Q_{H_2}} \tag{4.34}$$

$$O_2' = \frac{0.21 Q_{air}}{Q_{air} + Q_{N_2} + Q_C + Q_{H_2}} \qquad (4.35)$$

From equation (4.34):

$$Q_{air} = \frac{Q_{N_2} - N_2'(Q_{N_2} + Q_C + Q_{H_2})}{N_2' - 0.79} \qquad (4.36)$$

From equation (4.35):

$$Q_{air} = \frac{O_2'(Q_{N_2} + Q_C + Q_{H_2})}{0.21 - O_2'} \qquad (4.37)$$

Combining equations (4.36) and (4.37) yields the rate of carbon gasification,

$$Q_C = \frac{0.21 Q_{N_2}[1 - O_2' - N_2'] + Q_{H_2}[0.79 O_2' - 0.21 N_2']}{0.21 N_2' - 0.79 O_2'} \qquad (4.38)$$

The parameter χ is calculated by closing the carbon balance, such that the cumulative amount of carbon gasified by the end of the experiment is equal to the total amount of carbon injected. By iterating over different values of χ, a value of χ is found for which the carbon is balanced. This is considered to be the experimental χ value.

4.3 Slag Foaming

4.3.1 Average Bubble Size Estimation

For most experiments, frozen slag samples were obtained from the walls of the crucible and from the injection lance. These were then photographed, with a

ruler for scaling, using a digital camera and a flatbed scanner. Figure 4.4, a picture of frozen slag on the injection lance from experiment 34R, shows typical slag bubbles. Volume-averaged slag bubble sizes were estimated by measuring the diameter of a number of randomly selected bubbles in the images, calculating their volumes and taking the average value, and then determining the average diameter from the average volume. It is recognized that this approach is not very precise but it was used in the absence of a more sophisticated method. In injection experiment 32, the slag was of a composition that caused it to become powder immediately upon cooling, making bubble size measurements impossible.
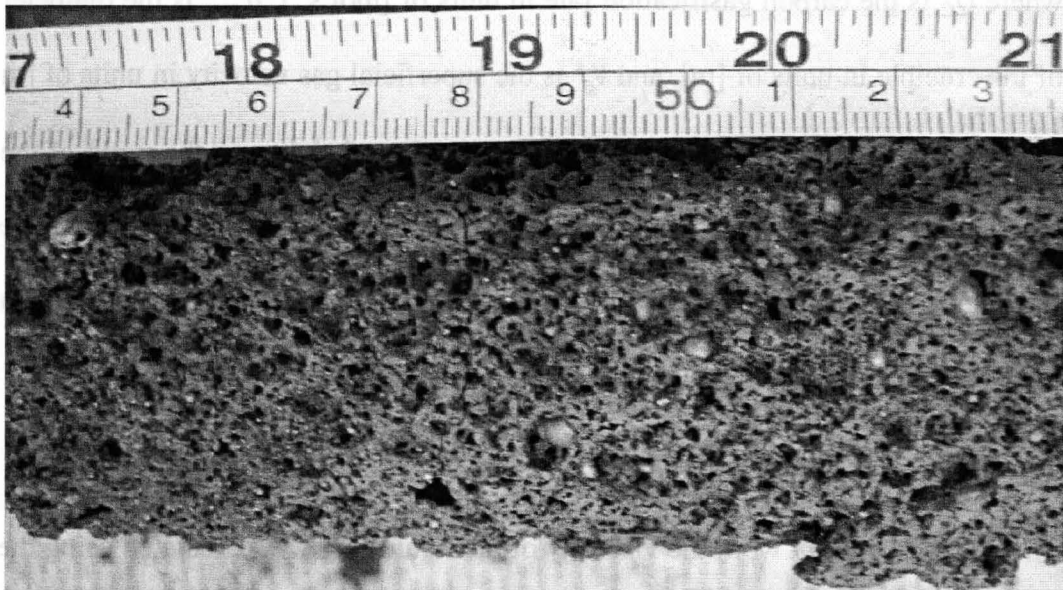
Figure 4.4 - Picture of frozen slag on injection lance from experiment 34R

4.3.2 Calculation of the Experimental Foaming Index

The slag foam height from the top of the static slag bath, Δh, was measured for each of the experiments in the present work. The foaming index is the ratio of Δh to the superficial gas velocity as defined in equation (2.55). The superficial gas velocity was calculated from the experimental carbon gasification rate by the following equation,

$$V_g^s = \frac{Q_g}{A_c} = \frac{\frac{22.414}{1000} Q_C}{\frac{\pi}{4} d_{cru}^2} \tag{4.39}$$

where Q_C is the carbon gasification rate in units of [mol s^{-1}], d_{cru} is the diameter of the crucible in units of [m], and V_g^s is the superficial gas velocity in units of [m s^{-1}]. It is reasonable to assume that the measured foam height was the result of the maximum carbon gasification rate, since any gasification rate smaller than the maximum would have resulted in a lower superficial gas velocity and hence a lower foam height than the one measured.

4.3.3 Slag Viscosity

In the current work the viscosity of the liquid slag was calculated using the model by Urbain (1987) as described in section 2.8.1. However, some slags were of a temperature and composition such that solid phase particles precipitated, altering the effective viscosity of the melt. The volume fraction of solid particles was calculated from a phase diagram for each experimental slag, and the relation

given by Brinkman (1952), presented here in equation (2.57), was used to calculate the effective viscosity.

Ito and Fruehan (1989) and Jiang and Fruehan (1991) used Urbain's slag viscosity model and then applied Brinkman's equation to calculate the effective slag viscosity, and developed their correlations for foaming index using the effective viscosity values. Zhang and Fruehan (1995) investigated slags that would not have contained any precipitated solids. It appears that Jung and Fruehan (2000) used Urbain's model alone to calculate the slag viscosity without considering solid phase particles. Lahiri and Seetharaman (2002) used the experimental data of Zhang and Fruehan (1995) and Jung and Fruehan (2000) in deriving their model, so it is reasonable to conclude that when applying their correlation, viscosities should be calculated using Urbain's model without considering solid phase particles as Jung and Fruehan (2000) did. When applying the other models (Ito and Fruehan, Jiang and Fruehan and Zhang and Fruehan) in the current work, solid phase particles were taken into account.

4.4 Experimental Results

The carbon injection rate, maximum carbon gasification rate, slag foam height, foaming index and average slag bubble diameter for injection experiments "Nucor 1", 34R, 33, 32, 24, 22 and 16 are listed in Table 4.3. The abbreviation "NCR 1" is used for "Nucor 1" and "R" for repeat, where repeat indicates that the original experiment failed and was repeated with the exact same conditions.

Detailed experimental conditions and results are given in the appendix, section A.1.

Table 4.3 - Experimental results

	NCR 1	34R	33	32	24	22	16
Carbon injection rate [mol s^{-1}]	0.0352	0.0749	0.0566	0.0391	0.0338	0.0359	0.0338
Maximum carbon gasification rate [mol s^{-1}]	0.0386	0.0987	0.0562	0.0318	0.0334	0.0512	0.0244
Slag foam height [m]	0.158	0.190	0.177	0.134	0.0767	0.0962	0.0508
Foaming index [s]	5.18	2.43	3.98	5.34	2.91	2.38	2.63
Average bubble diameter [mm]	1.6	1.5	1.0	-	1.7	1.9	1.3

A plot of the maximum carbon gasification rate versus the carbon injection rate is given in Figure 4.5, and Figure 4.6 is the slag foam height plotted against the superficial gas velocity. Figure 4.7 compares the experimental foaming indices with those calculated using correlations in the literature. The equation from Jiang and Fruehan (1991) was extrapolated to bubble sizes measured in the

current work, which were smaller than those used in developing the correlation, and the result is shown in Figure 4.8 along with the predictions of the model by Lahiri and Seetharaman (2002) for comparison. The natural logarithms of foaming index and slag viscosity are plotted against inverse temperature in Figure 4.9. In this plot the filled points represent those experiments in the current work that were within the range of linear dependency of foam height on superficial gas velocity and the unfilled points represent the experiments that were not.

Some trends are apparent in the experimental results, which are noted briefly here and discussed in more detail in Chapter 5. The carbon gasification rate was highly dependent on the injection rate, but was not observed to be influenced by temperature, iron oxide content of the slag or basicity of the slag. The slag foam height was dependent on the superficial gas velocity, which was in turn dependent on the carbon gasification rate and hence carbon injection rate. Figure 4.6 shows that foam height deviated from linear dependency on the superficial gas velocity above a critical foam height, where increasing the superficial gas velocity resulted in a diminishing increase in foam height. Two distinct groupings are seen in Figure 4.6, confirming that foam height was highly dependent on temperature, which is a major factor in determining slag viscosity. In Figure 4.7 it is observed that of the four correlations from the literature used to predict foaming index, the one from Lahiri and Seetharaman (2002) was most accurate under the current conditions. The one from Jiang and Fruehan (1991) was very inaccurate, and the other two gave fairly poor predictions. When the

relation from Jiang and Fruehan (1991) was extrapolated to the bubble sizes observed in the current work assuming an inverse dependency of foaming index on average bubble diameter, it gave much better predictions as shown in Figure 4.8. This indicates that bubble size is an important factor in determining foam height and stability. The relationships between foaming index, slag viscosity and temperature are illustrated in Figure 4.9. It is observed that foaming index and viscosity exhibited very similar temperature dependency, most notably for experiments with foam heights in the range where foaming index was independent of superficial gas velocity. The apparent activation energy for the decay of foam for those experiments was calculated to be 246 kJ mol^{-1}, and the activation energy for viscous flow of the slag was found to be 247 kJ mol^{-1}. The values of apparent activation energy for the decay of foam and activation energy for viscous flow of the slag were given by Ozturk and Fruehan (1995) as 139.6 kJ mol^{-1} and 144.7 kJ mol^{-1}, respectively.
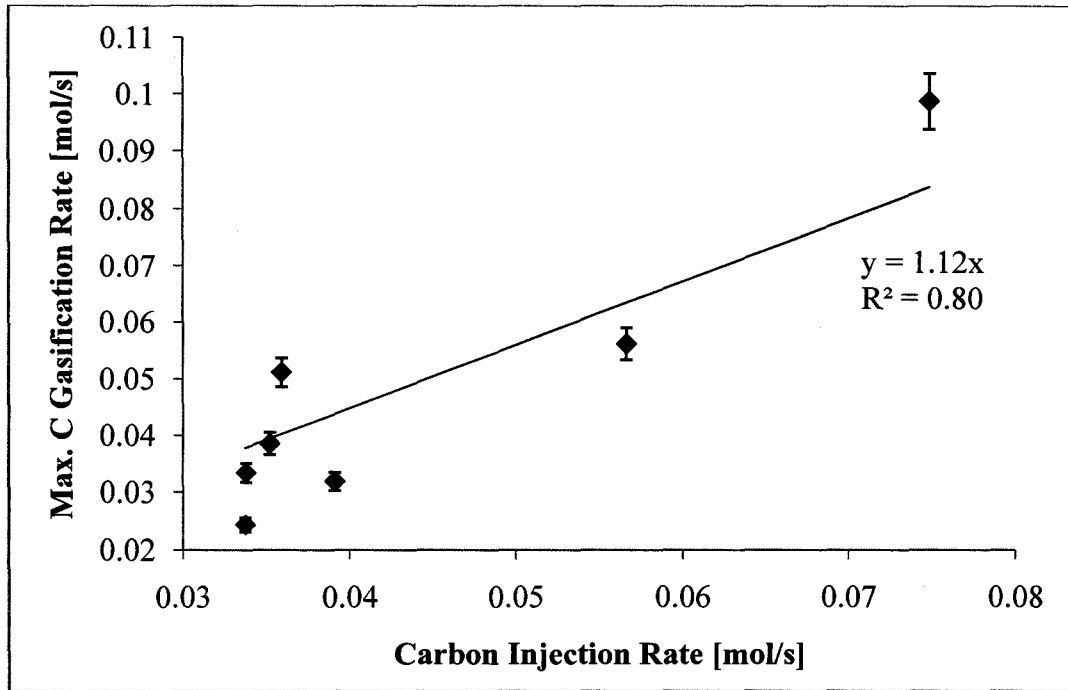
Figure 4.5 - Dependence of carbon gasification rate on carbon injection rate
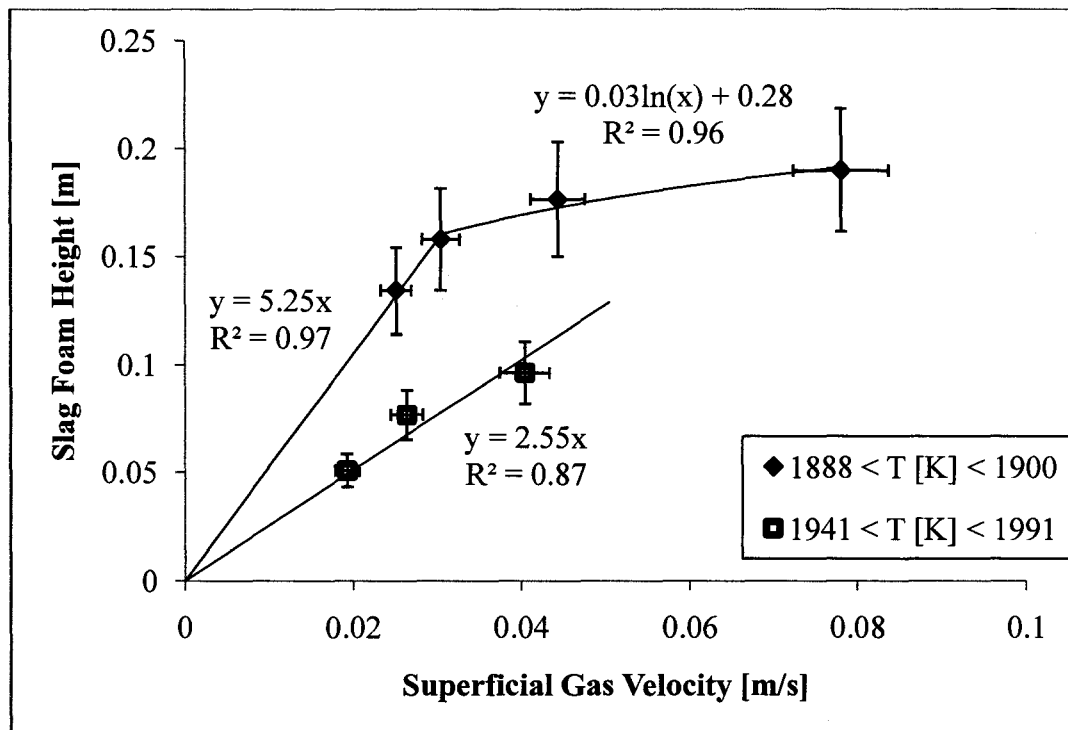
Figure 4.6 - Slag foam height vs. superficial gas velocity
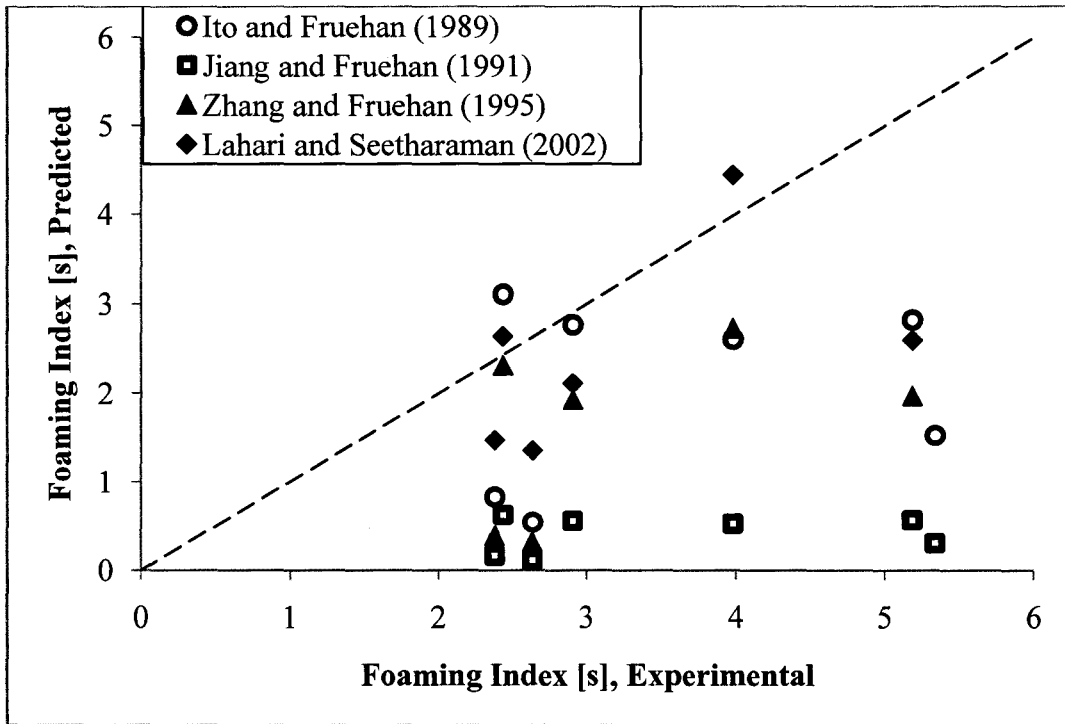
Figure 4.7 - Predicted vs. experimental foaming index
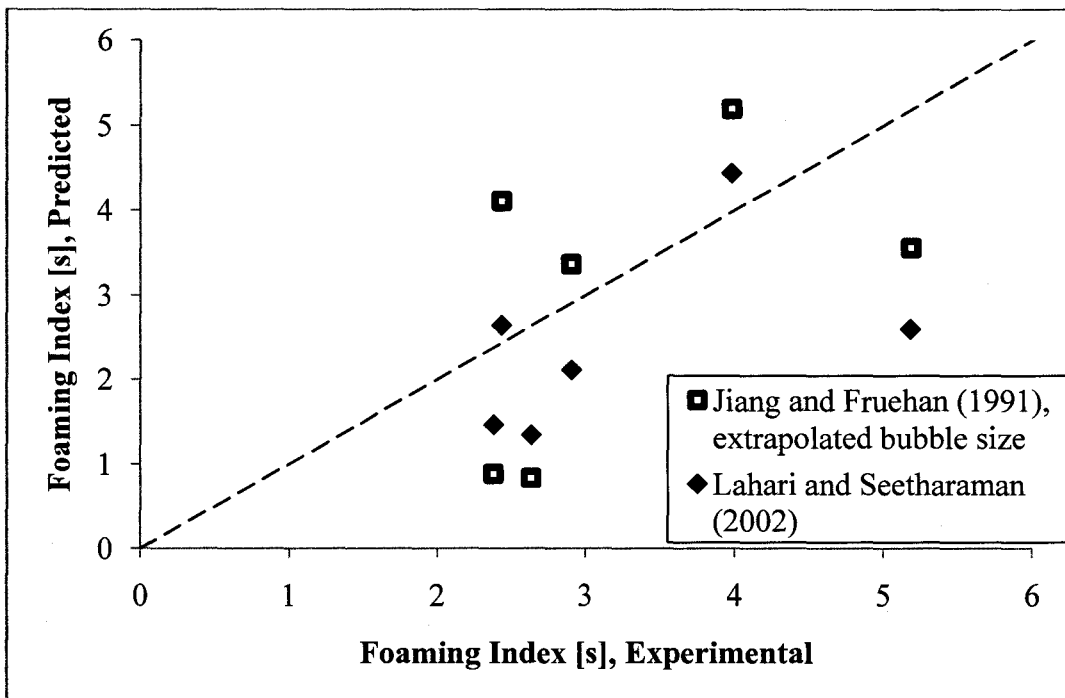
Figure 4.8 - Effect of bubble size on foaming index
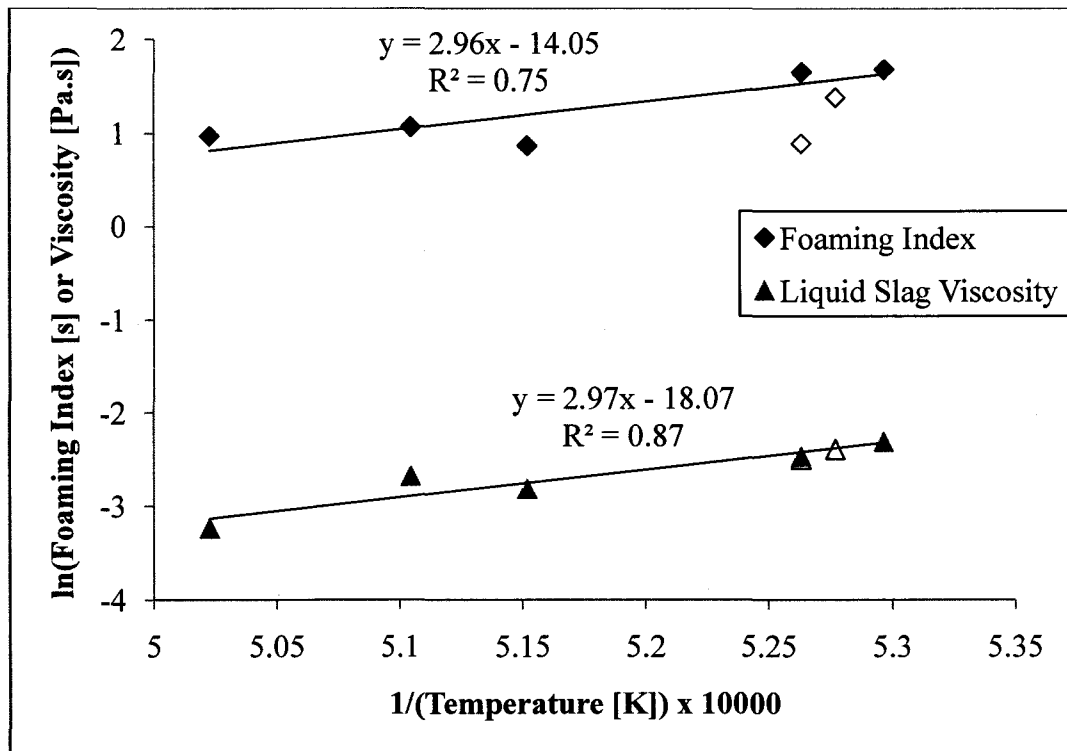
Figure 4.9 - Temperature dependency of foaming index and viscosity

Chapter 5: Discussion

5.1 Carbon-Slag Reaction Model

5.1.1 Overview

A model has been developed in this work that utilizes rate equations for the reactions at the slag-gas and carbon-gas interfaces given by Barati and Coley (2006) and Turkdogan and Vinters (1970), respectively, to predict reaction rate, amount of carbon, slag-gas interfacial area, bubble size, and gas composition as functions of reaction time. A system is assumed which consists of carbon particles each surrounded by a spherical gas halo suspended in a bath of molten slag. The reaction between carbon and slag proceeds via gaseous intermediates CO_2 and CO. This system is illustrated in Figure 5.1.
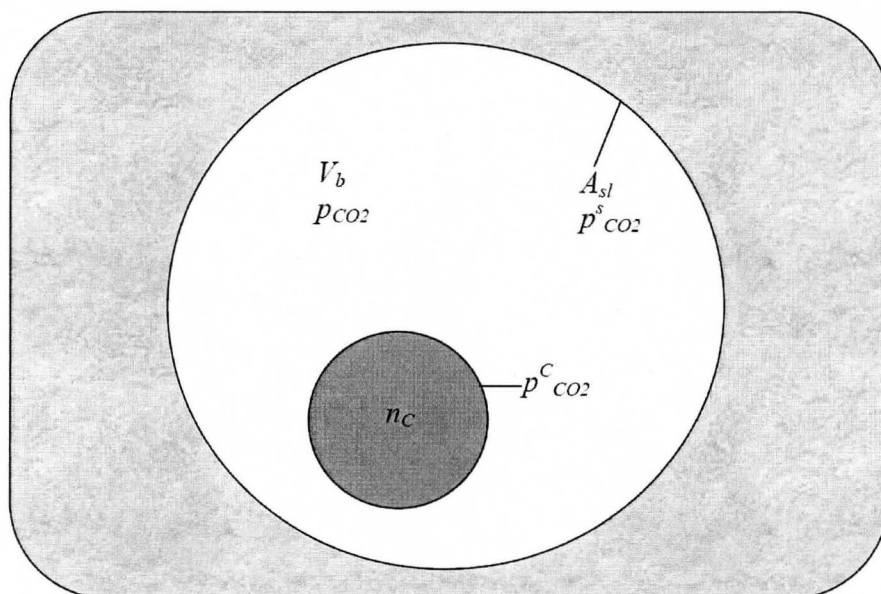
Figure 5.1 - Schematic diagram of carbon particle, gas bubble and slag

5.1.2 Assumptions

The assumptions adopted in development of the carbon-slag reaction model are:

1. The carbon reacts in the complete internal burning regime. An extrapolation of the data from Turkdogan et al. (1968) given in Table 2.1 showed that complete internal burning should occur in electrode graphite particles of diameter less than 0.2 mm at 1773 K. As temperature increases the critical particle diameter for chemical reaction control decreases, so that pore diffusion plays an increasingly important role.

2. The gas, slag, and solid carbon are each uniform in temperature and composition.

3. The reactivity of the carbon does not change with time.

4. The gas phase consists of only CO and CO_2. This is a valid assumption because even though the carbon particles are injected using nitrogen carrier gas, they do not begin to react until they contact the slag. When the carbon contacts the slag, it begins to generate a new gas bubble which would only contain CO and CO_2.

5. The total pressure in the gas phase is one atmosphere.

6. Each gas bubble is perfectly spherical. It is possible in highly foamed slag that bubbles may interact and assume a polyhedral shape when in contact with each other. Also, if there were a number of bubbles associated with each carbon particle, the bubbles in contact with each other would assume a

polyhedral shape. However, bubbles observed experimentally were generally spherical.

7. The volume of the solid carbon inside the bubble is negligible compared to the volume of the bubble. This is obviously not true at very early reaction times, but the bubble grows quickly and at 0.5 second is predicted to be over 4.5 times the diameter, and hence more than 95 times the volume, of the carbon particle.

8. Particulate carbon is injected into the slag at a constant rate.

9. All carbon particles have the same initial size and density.

5.1.3 Single Carbon Particle

5.1.3.1 Model Derivation

The overall reaction between carbon and slag is

$$C(s) + O(slag) = CO(g) \qquad (5.1)$$

By mass balance, the number of moles of CO produced is equal to the number of moles of solid carbon consumed which is also equal to the number of moles of oxygen consumed from the slag. The molar rate of carbon consumption is equal to the molar rate of oxygen consumption and equal to the negative of the molar rate of CO consumption:

$$\frac{dn_C}{dt} = \frac{dn_O}{dt} = -\frac{dn_{CO}}{dt} \qquad (5.2)$$

At the carbon-gas interface the rate of reaction in units of [mol C s^{-1}] may be expressed by the equation given by Turkdogan and Vinters (1970):

$$-\frac{dn_C}{dt} = n_C \frac{\Phi_1\left(p_{CO_2} - p_{CO_2}^C\right)}{1 + \left(\frac{p_{CO}}{\phi_{CO}}\right)} \tag{5.3}$$

It is assumed that the reactivity of the carbon does not change as the reaction proceeds, so the rate given by equation (5.3) is a function of n_C, p_{CO} and p_{CO_2}. At time $t = 0$, $n_C = n_C^\circ$ and at time $t = t$, $n_C = n_C$. Separating variables in equation (5.3) and integrating yields

$$n_C = n_C^\circ \cdot \exp\left[\frac{\Phi_1\left(p_{CO_2}^C - p_{CO_2}\right)}{1 + \left(\frac{p_{CO}}{\phi_{CO}}\right)} t\right] \tag{5.4}$$

Equation (5.4) describes the amount of carbon in the particle as a function of time and gas composition. Taking the derivative with respect to time in equation (5.4) yields an expression for the rate of reaction of carbon at the carbon-gas interface as a function of gas composition and time,

$$\left(\frac{dn_C}{dt}\right)_{c-g} = n_C^\circ \left(\frac{\Phi_1\left(p_{CO_2}^C - p_{CO_2}\right)}{1 + \left(\frac{p_{CO}}{\phi_{CO}}\right)}\right) \exp\left[\frac{\Phi_1\left(p_{CO_2}^C - p_{CO_2}\right)}{1 + \left(\frac{p_{CO}}{\phi_{CO}}\right)} t\right] \tag{5.5}$$

At the slag-gas interface the rate of reaction in units of [mol O s^{-1}] is given by the equation

$$-\frac{dn_O}{dt} = A_{sl} k_a \left(p_{CO} a_O - p_{CO_2} \right) \qquad (5.6)$$

The rate constant k_a is a function of temperature and slag composition and may be calculated using the model by Barati and Coley (2006) as discussed in section 2.6.2. It is assumed for the moment that the reactivity of the slag does not change as the reaction proceeds, so the rate given by equation (5.6) is a function of A_{sl}, p_{CO} and p_{CO_2}.

The slag-gas interfacial area, A_{sl}, may be expressed as a function of the extent of reaction as follows. Since it is assumed that the volume of solid carbon is negligible compared to the volume of the bubble, the volume of the bubble can be approximated as the volume of CO produced by the reaction,

$$V_b = \frac{M_{CO}}{\rho_{CO}} n_{CO} \qquad (5.7)$$

Differentiating equation (5.7) with respect to time yields an expression for the change in bubble volume with time in terms of the rate of reaction of CO,

$$\frac{dV_b}{dt} = \frac{M_{CO}}{\rho_{CO}} \frac{dn_{CO}}{dt} \qquad (5.8)$$

The volume of the bubble is related to its diameter by:

$$V_b = \frac{1}{6} \pi d_b{}^3 \qquad (5.9)$$

Differentiating equation (5.9) with respect to time gives an expression for the change in bubble volume in terms of the change in bubble diameter,

$$\frac{dV_b}{dt} = \frac{1}{2}\pi d_b{}^2 \frac{d(d_b)}{dt} \tag{5.10}$$

Combining equations (5.2), (5.8) and (5.10) results in an expression for the change in bubble diameter in terms of the rate of reaction of carbon,

$$\frac{d(d_b)}{dt} = -\frac{2}{\pi d_b{}^2}\frac{M_{CO}}{\rho_{CO}}\frac{dn_C}{dt} \tag{5.11}$$

The slag-gas interfacial area is related to the diameter of the gas bubble by:

$$A_{sl} = \pi d_b{}^2 \tag{5.12}$$

Differentiating equation (5.12) with respect to time results in an equation describing the change in slag-gas interfacial area in terms of the change in bubble diameter,

$$\frac{dA_{sl}}{dt} = 2\pi d_b \frac{d(d_b)}{dt} \tag{5.13}$$

Combining equations (5.11) and (5.13) and substituting for the bubble diameter from equation (5.12) yields

$$\frac{dA_{sl}}{dt} = -(16\pi)^{1/2}\frac{M_{CO}}{\rho_{CO}}\frac{1}{A_{sl}{}^{1/2}}\frac{dn_C}{dt} \tag{5.14}$$

Separating variables in equation (5.14) and integrating allows the slag-gas interfacial area to be expressed in terms of the amount of carbon n_C:

$$A_{sl} = (36\pi)^{1/3} \left(\frac{M_{CO}}{\rho_{CO}}\right)^{2/3} (n_C^\circ - n_C)^{2/3} \tag{5.15}$$

Now, combining equations (5.2), (5.6) and (5.15), separating variables and integrating from $t = 0$ to $t = t$ and $n_C = n_C^\circ$ to $n_C = n_C$, and taking the derivative with respect to time, the result is an equation for the rate of reaction of carbon at the slag-gas interface as a function of gas composition and time,

$$\left(\frac{dn_C}{dt}\right)_{s-g} = 4\pi \left(\frac{M_{CO}}{\rho_{CO}}\right)^2 k_a^3 (p_{CO_2} - p_{CO}a_O)^3 t^2 \tag{5.16}$$

Under the assumption that the gas bubble contains only CO and CO_2, it follows that

$$p_{CO_2} + p_{CO} = 1 \tag{5.17}$$

Therefore equations (5.4), (5.5) and (5.16) may be modified to:

$$n_C = n_C^\circ \cdot \exp\left[\frac{\Phi_1 \phi_{CO}\left(p_{CO_2}^C - p_{CO_2}\right)}{1 + \phi_{CO} - p_{CO_2}} t\right] \tag{5.18}$$

$$\left(\frac{dn_C}{dt}\right)_{c-g} = n_C^\circ \left(\frac{\Phi_1 \phi_{CO}\left(p_{CO_2}^C - p_{CO_2}\right)}{1 + \phi_{CO} - p_{CO_2}}\right) \exp\left[\frac{\Phi_1 \phi_{CO}\left(p_{CO_2}^C - p_{CO_2}\right)}{1 + \phi_{CO} - p_{CO_2}} t\right] \tag{5.19}$$

$$\left(\frac{dn_C}{dt}\right)_{s-g} = 4\pi \left(\frac{M_{CO}}{\rho_{CO}}\right)^2 k_a^3 \left(p_{CO_2}(1 + a_O) - a_O\right)^3 t^2 \tag{5.20}$$

Since the rate of reaction must be the same at the carbon-gas and slag-gas interfaces, the system of equations (5.19) and (5.20) may be solved at any instant in time for the rate of reaction and the pressure of CO_2 in the gas bubble, p_{CO_2}. This value of p_{CO_2} can be used in equation (5.18) to determine the amount of carbon in the particle at the given time.

The diameter of the gas bubble at any instant in time may be calculated by combining equations (5.12) and (5.15) to obtain equation (5.21), and using in equation (5.21) the value of n_C found by solving equation (5.18).

$$d_b = \left[\frac{(36\pi)^{1/3}}{\pi} \left(\frac{M_{CO}}{\rho_{CO}} \right)^{2/3} \left(n_C^\circ - n_C \right)^{2/3} \right]^{1/2} \tag{5.21}$$

5.1.3.2 Model Implementation

The initial number of moles of carbon in the particle, n_C°, may be calculated from the estimated average particle diameter, d_p°, via equations (5.22) and (5.23). The determination of d_p° using equation (3.1) has been described in section 3.2.3.3. An average bulk density of 1.1 g cm^{-3} was assumed for carbon (Story and Fruehan, 2000).

$$V_C^\circ = \frac{1}{6} \pi \left(d_p^\circ \right)^3 \tag{5.22}$$

$$n_C^\circ = V_C^\circ \frac{\rho_C}{M_C} \tag{5.23}$$

The term a_0 is the equilibrium CO_2/CO ratio at the slag-gas interface and may be calculated for a given temperature and slag composition as described in section 4.2.3. The equilibrium pressure of CO_2 at the slag-gas interface, $p_{CO_2}^s$, can be calculated from a_0 under the assumption that $p_{CO_2} + p_{CO} = 1$ at the slag-gas interface. The equilibrium pressure of CO_2 at the carbon-gas interface, $p_{CO_2}^C$, is a function of temperature and may be calculated using the data given by Gaskell (2003) presented here in equations (4.21) and (4.22), also under the assumption that $p_{CO_2} + p_{CO} = 1$ at the carbon-gas interface. The carbon-gas rate constant terms, Φ_1 and ϕ_{CO}, are given by Turkdogan and Vinters (1970) for coconut charcoal, metallurgical coke and electrode graphite and are presented here in equations (2.13), (2.15), (2.17) and (2.19). It has been assumed that the coal used in the present work is most like Turkdogan and Vinters' metallurgical coke, and thus Φ_1 and ϕ_{CO} are given by equations (2.15) and (2.19) respectively. The slag-gas rate constant, k_a, may be calculated for a given temperature and slag composition via the model by Barati and Coley (2006), given in equation (2.53). A density of 1.145 kg m^{-3} has been assumed for CO. For injection experiment "Nucor 1", the model parameters are given in Table 5.1.

Table 5.1 - Injection "Nucor 1" model parameters

d_p° [m]	2.02×10^{-4}
Temperature [K]	1900
a_O	0.265
$p_{CO_2}^C$ [atm]	3.81×10^{-5}
$p_{CO_2}^s$ [atm]	0.209
Φ_1 [atm^{-1} s^{-1}]	0.749
ϕ_{CO} [atm]	2.16
k_a [mol m^{-2} atm^{-1} s^{-1}]	0.437
ρ_C [kg m^{-3}]	1100
ρ_{CO} [kg m^{-3}]	1.145

The MATLAB code developed to run the single particle model is presented in the appendix, section A.2. The resultant predictions are given in Figure 5.2 to Figure 5.5.
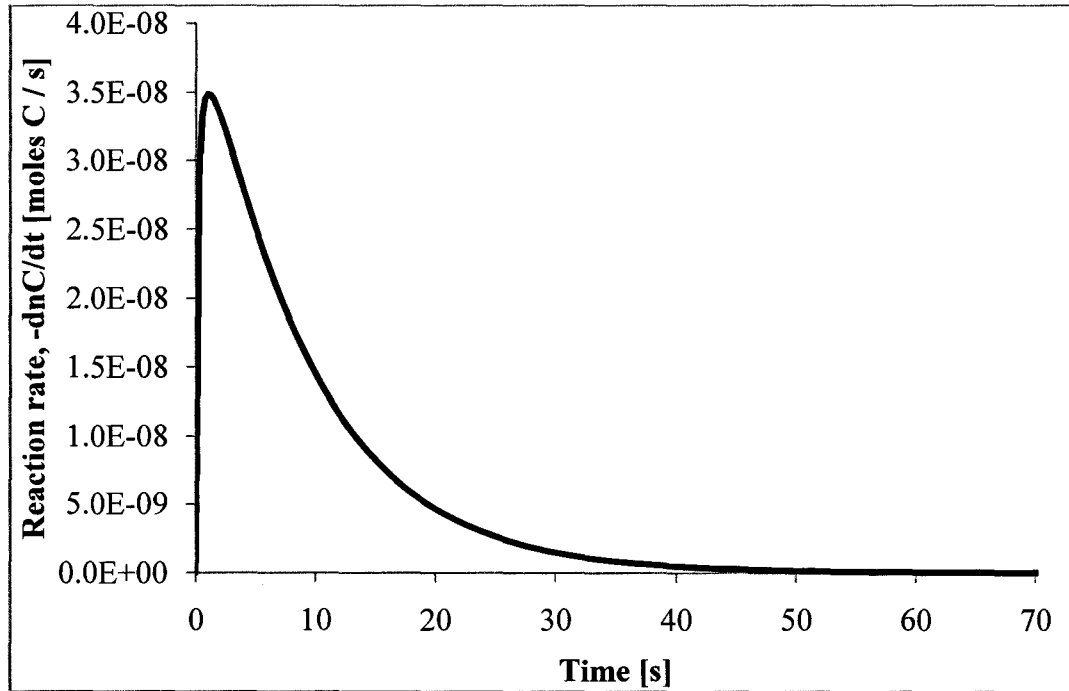
Figure 5.2 - Predicted rate of carbon consumption for a single carbon particle
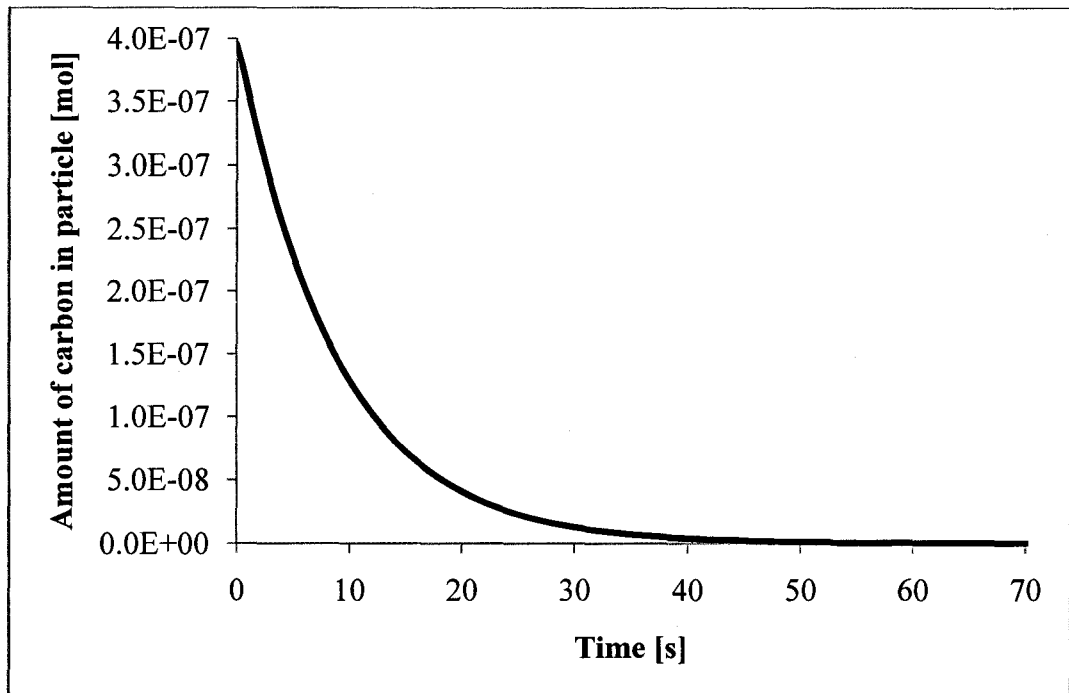
Figure 5.3 - Predicted amount of carbon for a single carbon particle
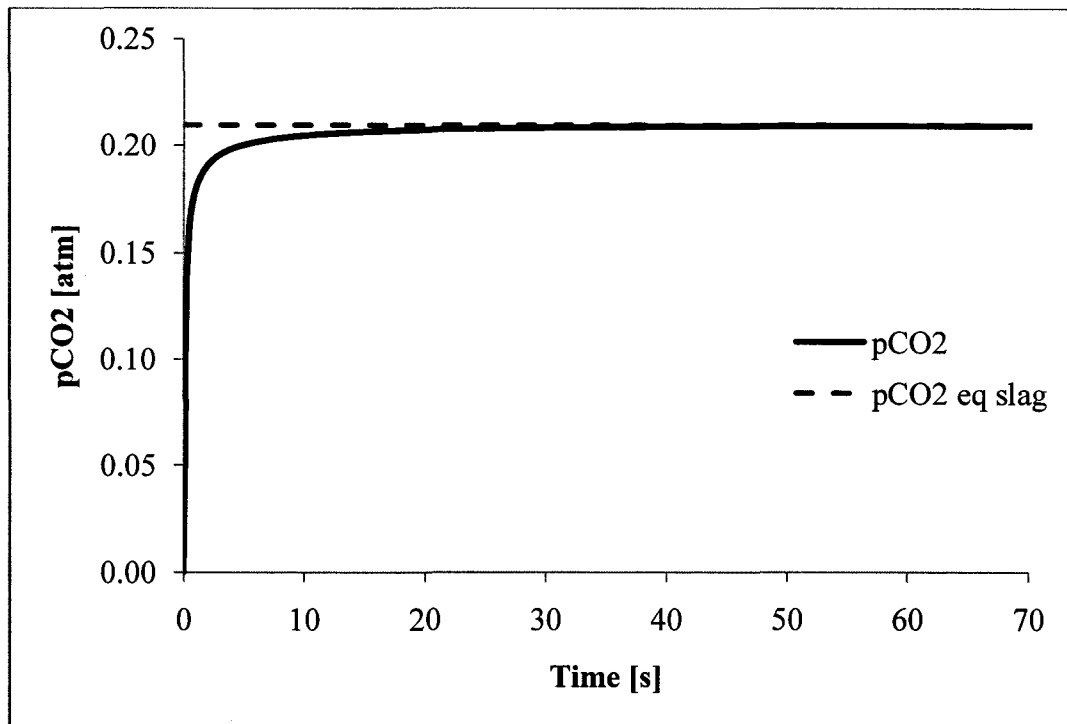
Figure 5.4 - Predicted pressure of CO_2 for a single carbon particle
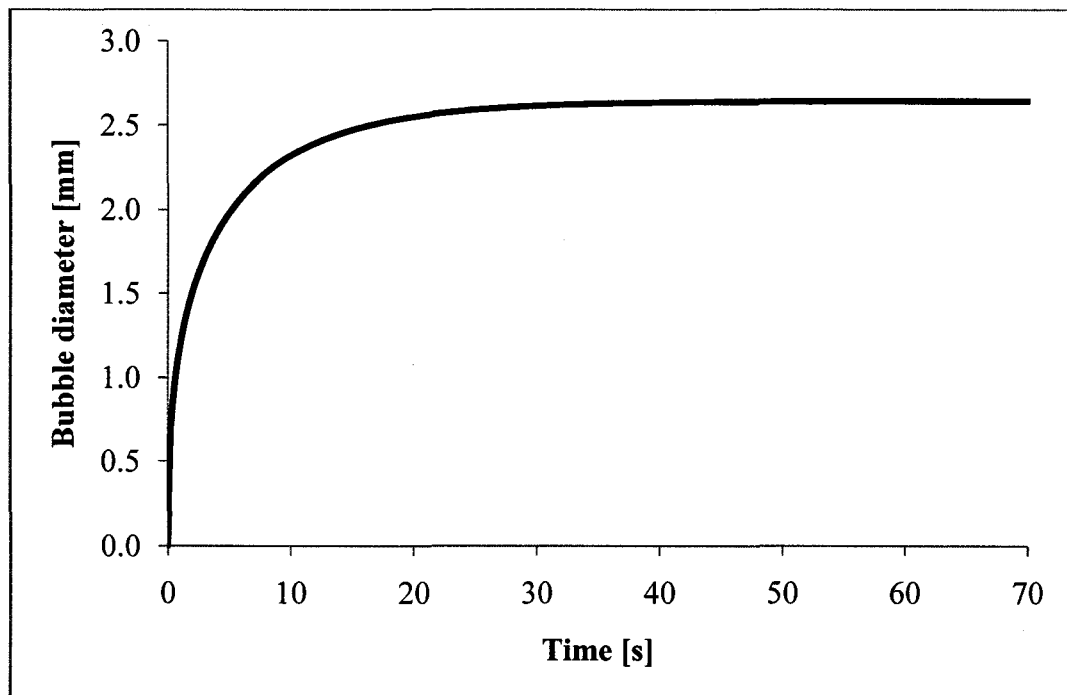
Figure 5.5 - Predicted bubble diameter for a single carbon particle

5.1.3.3 Discussion of Single Particle Model

At time zero, when the carbon particle has just become entrained in the slag, the reaction kinetics are controlled by the reaction at the slag-gas interface since the slag-gas interfacial area is very small. At this point p_{CO_2} is equal to its value at the carbon-gas interface, $p_{CO_2}^C$, because thermodynamic control is by the carbon. As the reaction progresses and the amount of carbon available for reaction, n_C, approaches zero, p_{CO_2} approaches its value at the slag-gas interface, $p_{CO_2}^S$. This is due to the carbon-gas reaction becoming infinitely slow as the amount of carbon approaches zero and the rate of the slag-gas reaction increasing as the slag-gas interfacial area increases, resulting in thermodynamic control shifting to the slag.

5.1.4 Multiple Carbon Particles injected over Time at a fixed Rate

5.1.4.1 Model Derivation

This model, henceforth referred to as the injection model, is an extension of the model for a single carbon particle derived above in section 5.1.3.1. It describes the entire injection process, including the overall reaction rate of carbon with slag, the amount of carbon in the slag, the composition of the gas phase, the slag-gas interfacial area (active and total areas), and the average bubble diameter as functions of time. The injection process involves a bath of molten slag into which carbon particles are injected at a constant rate beginning at time $t = 0$ and ceasing at time $t = t_{inj}$. After the injection of particles ends, the residual carbon

in the slag continues to react, so the injection process continues until all of the carbon has reacted.

Equations (5.18), (5.19) and (5.20) describe the amount of carbon and the rates of reaction at the carbon-gas and slag-gas interfaces as functions of time. Here these equations are adapted to express the amount of carbon and reaction rates in a single particle-bubble system in terms of the residence time of the particle in the slag, t_{res}, in equations (5.24), (5.25) and (5.26).

$$n_C = n_C^\circ \cdot \exp\left[\frac{\Phi_1 \phi_{CO}\left(p_{CO_2}^C - p_{CO_2}\right)}{1 + \phi_{CO} - p_{CO_2}} t_{res}\right] \tag{5.24}$$

$$\left(\frac{dn_C}{dt_{res}}\right)_{C-g} = n_C^\circ \left(\frac{\Phi_1 \phi_{CO}\left(p_{CO_2}^C - p_{CO_2}\right)}{1 + \phi_{CO} - p_{CO_2}}\right)$$

$$\cdot \exp\left[\frac{\Phi_1 \phi_{CO}\left(p_{CO_2}^C - p_{CO_2}\right)}{1 + \phi_{CO} - p_{CO_2}} t_{res}\right] \tag{5.25}$$

$$\left(\frac{dn_C}{dt_{res}}\right)_{s-g} = 4\pi \left(\frac{M_{CO}}{\rho_{CO}}\right)^2 k_a{}^3 \left(p_{CO_2}(1 + a_0) - a_0\right)^3 t_{res}{}^2 \tag{5.26}$$

The number of particles at a residence time, $N_p^{t_{res}}$, is given by equations (5.28) and (5.29), where R_p is the rate of injection of particles calculated via equation (5.27), R_i is the carbon injection rate in units of [mol s^{-1}], and dt_{res} is the time interval between possible residence times.

$$R_p = \frac{R_i}{n_C^\circ} \tag{5.27}$$

During particle injection, that is, for $t < t_{inj}$,

$$N_p^{t_{res}} = \begin{cases} R_p dt_{res} & \text{for all } t_{res} \text{ such that} & 0 \leq t_{res} \leq t \\ 0 & & \text{otherwise} \end{cases} \tag{5.28}$$

After particle injection has stopped, that is, for $t \geq t_{inj}$,

$$N_p^{t_{res}} = \begin{cases} R_p dt_{res} & \text{for all } t_{res} \text{ such that} & (t - t_{inj}) < t_{res} \leq t \\ 0 & & \text{otherwise} \end{cases} \tag{5.29}$$

The total rate of reaction at any time in the injection process may be calculated by multiplying the number of particles at a residence time by the rate of reaction of one particle at that residence time and then summing over all possible residence times at that time in the process. Similarly, the total amount of carbon in the slag at any time in the injection process may be calculated by multiplying the number of particles at a residence time by the amount of carbon in one particle at that residence time and then summing over all possible residence times. Thus, where the superscript *tot* denotes "total":

For $t < t_{inj}$,

$$\left(\frac{dn_C}{dt}\right)^{tot} = \sum_0^t N_p^{t_{res}} \frac{dn_C}{dt_{res}} = \sum_0^t R_p \left(\frac{dn_C}{dt_{res}}\right) dt_{res} \tag{5.30}$$

If dt_{res} is infinitesimal,

$$\left(\frac{dn_C}{dt}\right)^{tot} = R_p \int_0^t \left(\frac{dn_C}{dt_{res}}\right) dt_{res} \tag{5.31}$$

Similarly for n_C,

$$n_C{}^{tot} = \sum_0^t N_p^{tres} n_C = R_p \int_0^t n_C dt_{res} \qquad (5.32)$$

For $t \geq t_{inj}$,

$$\left(\frac{dn_C}{dt}\right)^{tot} = \sum_{(t-t_{inj})}^t N_p^{tres} \frac{dn_C}{dt_{res}} = R_p \int_{(t-t_{inj})}^t \left(\frac{dn_C}{dt_{res}}\right) dt_{res} \qquad (5.33)$$

$$n_C{}^{tot} = \sum_{(t-t_{inj})}^t N_p^{tres} n_C = R_p \int_{(t-t_{inj})}^t n_C dt_{res} \qquad (5.34)$$

Equations (5.25) and (5.26) may be combined with equation (5.31) or equation (5.33) and equation (5.24) with equation (5.32) or equation (5.34) to calculate the total rate at the carbon-gas and slag-gas interfaces and the total amount of carbon in the slag as functions of time and p_{CO_2}, as given in equations (5.35) to (5.40).

For $t < t_{inj}$,

$$\left(\frac{dn_C}{dt}\right)_{c-g}^{tot} = R_p n_C^{\circ} \left[-1 + \exp\left(\frac{\Phi_1 \phi_{CO}\left(p_{CO_2}^C - p_{CO_2}\right)}{1 + \phi_{CO} - p_{CO_2}} t\right)\right] \qquad (5.35)$$

$$\left(\frac{dn_C}{dt}\right)_{s-g}^{tot} = R_p \frac{4\pi}{3} \left(\frac{M_{CO}}{\rho_{CO}}\right)^2 k_a{}^3 \left(p_{CO_2}(1 + a_0) - a_0\right)^3 t^3 \qquad (5.36)$$

$$n_C{}^{tot} = R_p n_C^{\circ} \left(\frac{1 + \phi_{CO} - p_{CO_2}}{\Phi_1 \phi_{CO} (p_{CO_2}^C - p_{CO_2})} \right)$$

$$\cdot \left[-1 + \exp\left(\frac{\Phi_1 \phi_{CO} (p_{CO_2}^C - p_{CO_2})}{1 + \phi_{CO} - p_{CO_2}} t \right) \right] \tag{5.37}$$

For $t \geq t_{inj}$,

$$\left(\frac{dn_C}{dt} \right)_{C-g}^{tot} = R_p n_C^{\circ} \left[\exp\left(\frac{\Phi_1 \phi_{CO} (p_{CO_2}^C - p_{CO_2})}{1 + \phi_{CO} - p_{CO_2}} t \right) \right.$$

$$\left. - \exp\left(\frac{\Phi_1 \phi_{CO} (p_{CO_2}^C - p_{CO_2})}{1 + \phi_{CO} - p_{CO_2}} (t - t_{inj}) \right) \right] \tag{5.38}$$

$$\left(\frac{dn_C}{dt} \right)_{s-g}^{tot} = R_p \frac{4\pi}{3} \left(\frac{M_{CO}}{\rho_{CO}} \right)^2 k_a{}^3 \left(p_{CO_2}(1 + a_0) - a_0 \right)^3$$

$$\cdot \left(t^3 - (t - t_{inj})^3 \right) \tag{5.39}$$

$$n_C{}^{tot} = R_p n_C^{\circ} \left(\frac{1 + \phi_{CO} - p_{CO_2}}{\Phi_1 \phi_{CO} (p_{CO_2}^C - p_{CO_2})} \right) \left[\exp\left(\frac{\Phi_1 \phi_{CO} (p_{CO_2}^C - p_{CO_2})}{1 + \phi_{CO} - p_{CO_2}} t \right) \right.$$

$$\left. - \exp\left(\frac{\Phi_1 \phi_{CO} (p_{CO_2}^C - p_{CO_2})}{1 + \phi_{CO} - p_{CO_2}} (t - t_{inj}) \right) \right] \tag{5.40}$$

Since the total reaction rate must be the same at the slag-gas and carbon-gas interfaces, the systems of equations (5.35) and (5.36) or (5.38) and (5.39) may be solved at any instant in time for the rate of reaction and overall partial pressure of

CO_2 in the gas phase. The total amount of carbon may be found at any instant in time by solving equation (5.37) or equation (5.40) using the calculated partial pressure of CO_2.

Since the rate of reaction at the slag-gas interface is now known, it is possible to calculate the slag-gas interfacial area actively participating in the reaction. The slag-gas interfacial area is related to the rate of reaction by equation (5.6), which may be re-written in terms of the active slag-gas interfacial area, A_{sl}^{act}, and the total rate of reaction as:

$$\left(\frac{dn_C}{dt}\right)^{tot} = A_{sl}^{act} k_a \left(p_{CO_2}(1 + a_0) - a_0\right) \tag{5.41}$$

Also, the total slag-gas interfacial area, that is, the area of the slag-gas interface created by bubble formation and growth, may be estimated. Equation (5.15) relates the slag-gas interfacial area to the amount of carbon in one particle. In the case of many particles, the average amount of carbon in one particle at any instant in time may be calculated by dividing the total amount of carbon by the number of particles:

$$n_C{}^{avg} = \frac{n_C{}^{tot}}{N_p} \tag{5.42}$$

By using $n_C{}^{avg}$ in equation (5.15) and multiplying by the number of particles, an estimate is arrived at for the total slag-gas interfacial area, A_{sl}^{tot}:

$$A_{sl}^{tot} = N_p (36\pi)^{1/3} \left(\frac{M_{CO}}{\rho_{CO}}\right)^{2/3} \left(n_C^\circ - n_C{}^{avg}\right)^{2/3} \tag{5.43}$$

The fraction of slag-gas interfacial area actively participating in the reaction is the ratio of active slag-gas interfacial area to total slag-gas interfacial area.

The average bubble diameter, d_b^{avg}, may be calculated from the total slag-gas interfacial area by equation (5.44),

$$\frac{A_{sl}^{tot}}{N_p} = \pi \left(d_b^{avg}\right)^2 \tag{5.44}$$

It has been assumed that the reactivity of the carbon does not change over time, but it may be important to take into consideration the changing slag composition as iron oxide is consumed from the slag over time. This is only a concern for long carbon injection durations where there is no mechanism for replenishing the iron oxide in the slag. The experiments performed in the present work showed that practically no iron was reduced out of the slag for relatively short injection durations (less than 140 seconds) under the given conditions as discussed in section 4.2.1. The slag rate constant k_a is proportional to the square of the total iron concentration in the slag. Therefore as iron oxide is reduced out of the slag the slag-gas reaction rate should decrease, affecting the overall rate and shifting the rate control. The possibility of changing slag reactivity has been incorporated into the injection model very simply as follows. The slag rate

constant k_a is assumed to be a function of the square of the total iron concentration and a constant, q,

$$k_a = q(C_{Fe})^2 \qquad (5.45)$$

The constant q may be calculated by dividing the rate constant for the slag at time zero, $k_a^{t=0}$, by the square of the initial total iron concentration C_{Fe}°,

$$q = \frac{k_a^{t=0}}{\left(C_{Fe}^{\circ}\right)^2} \qquad (5.46)$$

The term C_{Fe} is modeled as a linear function of time by equation (5.47), where Δ_{Fe} is the estimated decrease in iron concentration in the slag over the course of the carbon injection.

$$C_{Fe} = C_{Fe}^{\circ} - \frac{\Delta_{Fe}}{t_{inj}} t \qquad (5.47)$$

5.1.4.2 Model Implementation

The model parameters were calculated here in the same way as described in section 5.1.3.2. Values of 1100 kg m^{-3} and 1.145 kg m^{-3} were again assumed for the densities of carbon and CO, respectively.

The model predictions for carbon gasification rate and amount of carbon were observed to be sensitive to changes in the carbon reactivity, described by the carbon rate constant term Φ_1. Therefore, predictions were calculated twice, once for Φ_1 as given by Turkdogan and Vinters (1970) for metallurgical coke and

again for Φ_1 adjusted to give a better fit to the experimental data. The term Φ_1 has the following form in units of [atm^{-1} s^{-1}],

$$\log(60\Phi_1) = -\frac{13200}{T} + y \qquad (5.48)$$

where the value of y was given as 8.60 for metallurgical coke and 7.68 for electrode graphite by Turkdogan and Vinters (1970). In the present work the model best described the experimental data with y values of 8.22 for the Nucor coal and 7.97 for the Dofasco coal.

The parameter ϕ_{CO} is calculated via equation (2.19).

The model parameters for injection experiments "Nucor 1", 34R, 33, 32, 24, 22 and 16 are given in Table 5.2.

Table 5.2 - Injection model parameters

	Nucor 1	34R	33	32
d_p° [m]	2.02×10^{-4}	2.16×10^{-4}	2.16×10^{-4}	2.16×10^{-4}
Temperature [K]	1900	1900	1895	1888
a_0	0.265	0.244	0.281	0.323
$p_{CO_2}^C$ [atm]	3.81×10^{-5}	3.81×10^{-5}	3.92×10^{-5}	4.08×10^{-5}
$p_{CO_2}^s$ [atm]	0.209	0.196	0.219	0.244
Adjusted y	8.22	7.97	7.97	7.97
$k_a^{t=0}$ [mol m^{-2} atm^{-1} s^{-1}]	0.437	0.472	0.414	0.309
C_{Fe}° [mol %]	21.9	22.0	22.7	21.2
Δ_{Fe} [mol %]	2.00	2.00	2.00	2.00
R_i [mol s^{-1}]	0.0352	0.0749	0.0566	0.0391
t_{inj} [s]	138	127	120	80

	24	22	16
d_p° [m]	2.16×10^{-4}	2.16×10^{-4}	2.16×10^{-4}
Temperature [K]	1959	1941	1991
a_0	0.257	0.318	0.109
$p_{CO_2}^C$ [atm]	2.75×10^{-5}	3.04×10^{-5}	2.33×10^{-5}
$p_{CO_2}^s$ [atm]	0.204	0.241	0.0983
Adjusted y	7.97	7.97	7.97
$k_a^{t=0}$ [mol m^{-2} atm^{-1} s^{-1}]	0.416	1.13	4.98
C_{Fe}° [mol %]	17.7	35.4	42.3
Δ_{Fe} [mol %]	2.00	2.00	2.00
R_i [mol s^{-1}]	0.0338	0.0359	0.0338
t_{inj} [s]	126	126	138

The MATLAB code developed to run the injection model is presented in the appendix, section A.3. The resultant predictions for carbon gasification rate are shown in Figure 5.6 to Figure 5.12. The model predictions for residual carbon in the slag, partial pressure of CO_2, active fraction of slag-gas interfacial area and average bubble diameter are given in the appendix, section A.4. To compare the experimental partial pressure of CO_2 to the model predictions, the experimental partial pressure of CO_2 was considered to be the ratio $CO_2'/(CO' + CO_2')$ in the gas phase.
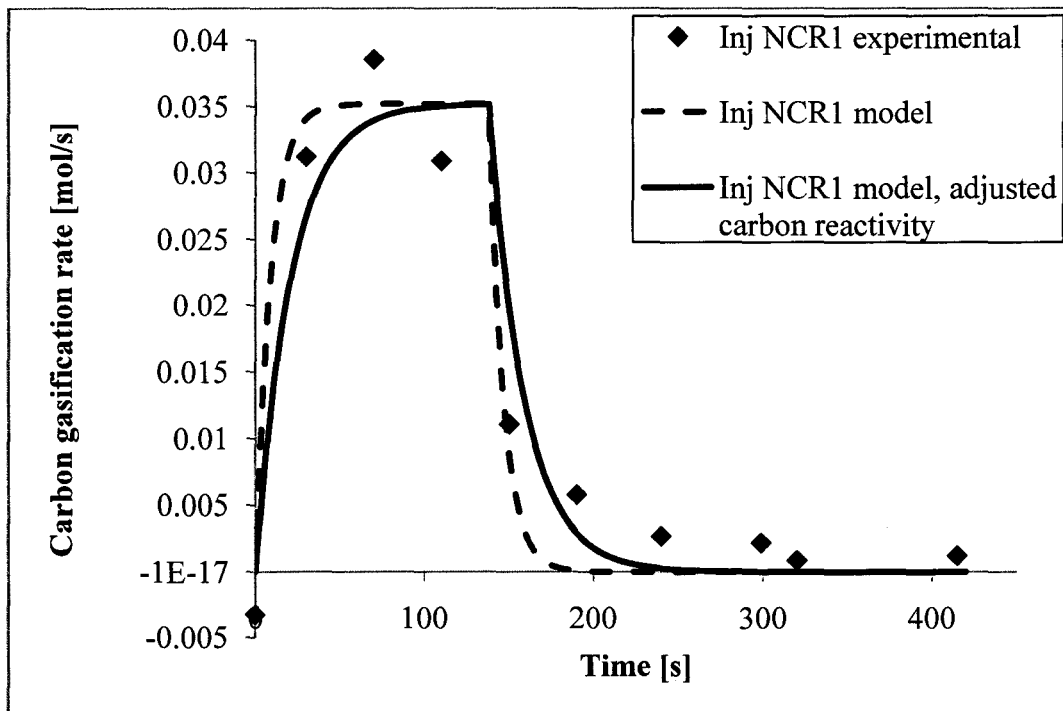
Figure 5.6 - Carbon gasification rate, experiment "Nucor 1"
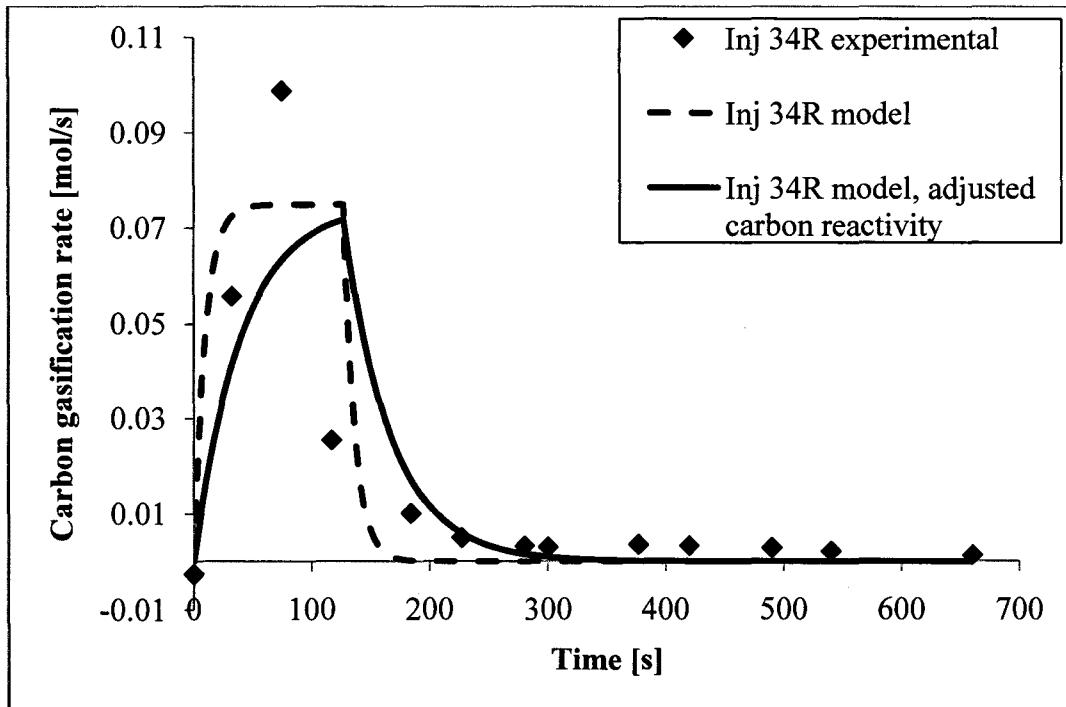
Figure 5.7 - Carbon gasification rate, experiment 34R
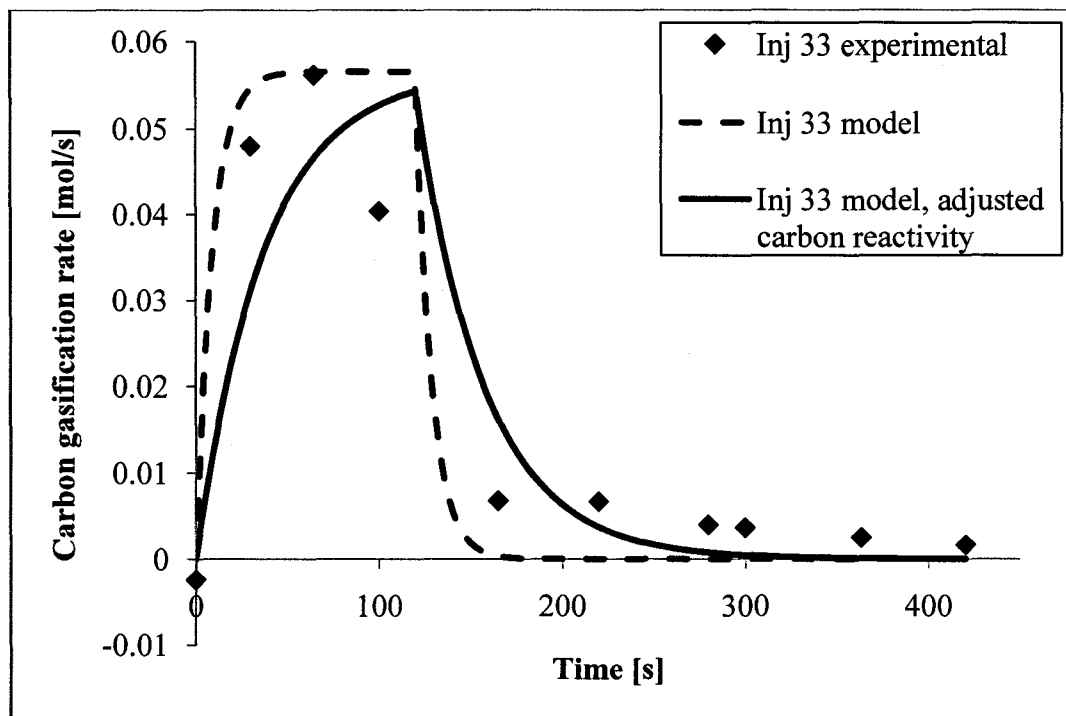
Figure 5.8 - Carbon gasification rate, experiment 33
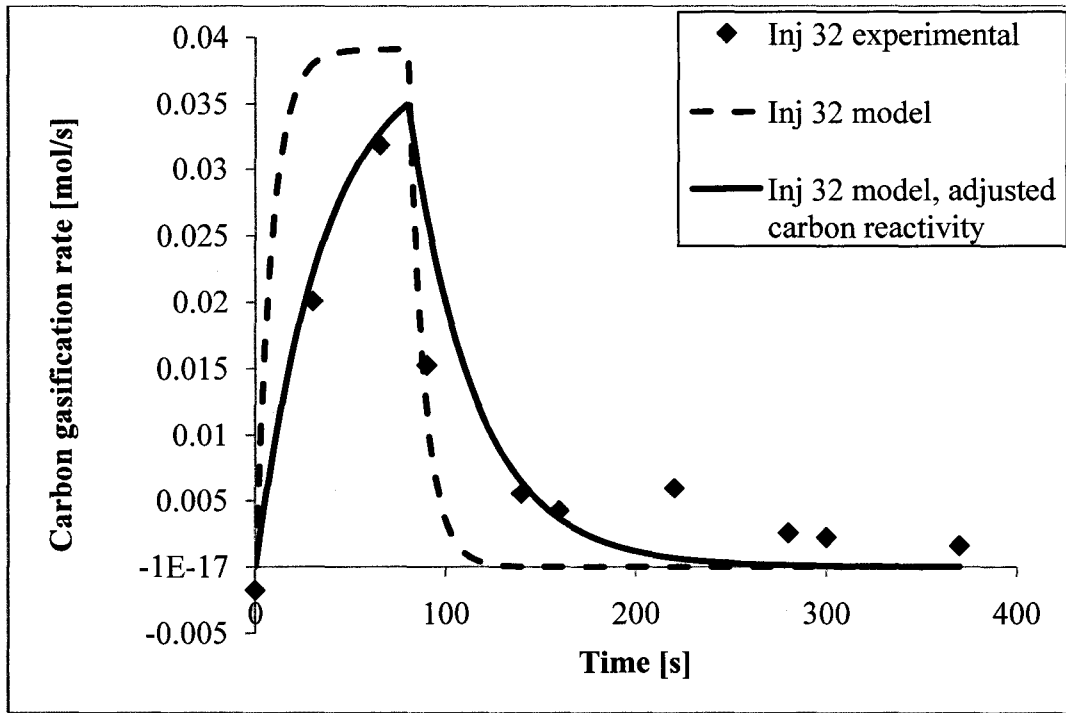
Figure 5.9 - Carbon gasification rate, experiment 32
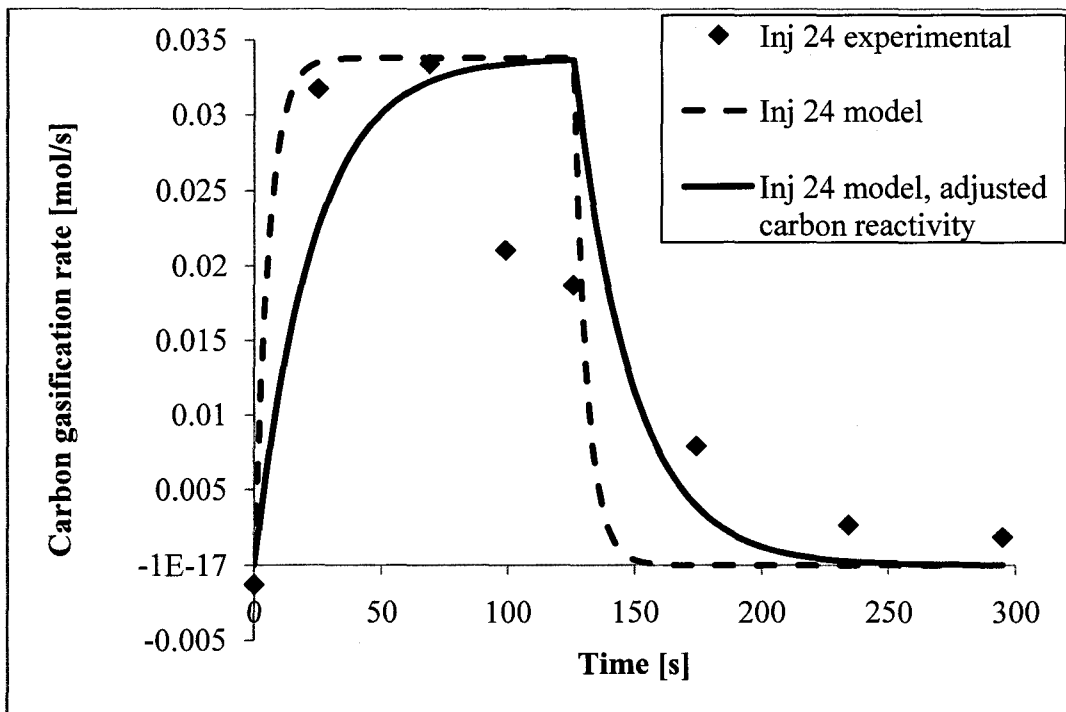
Figure 5.10 - Carbon gasification rate, experiment 24
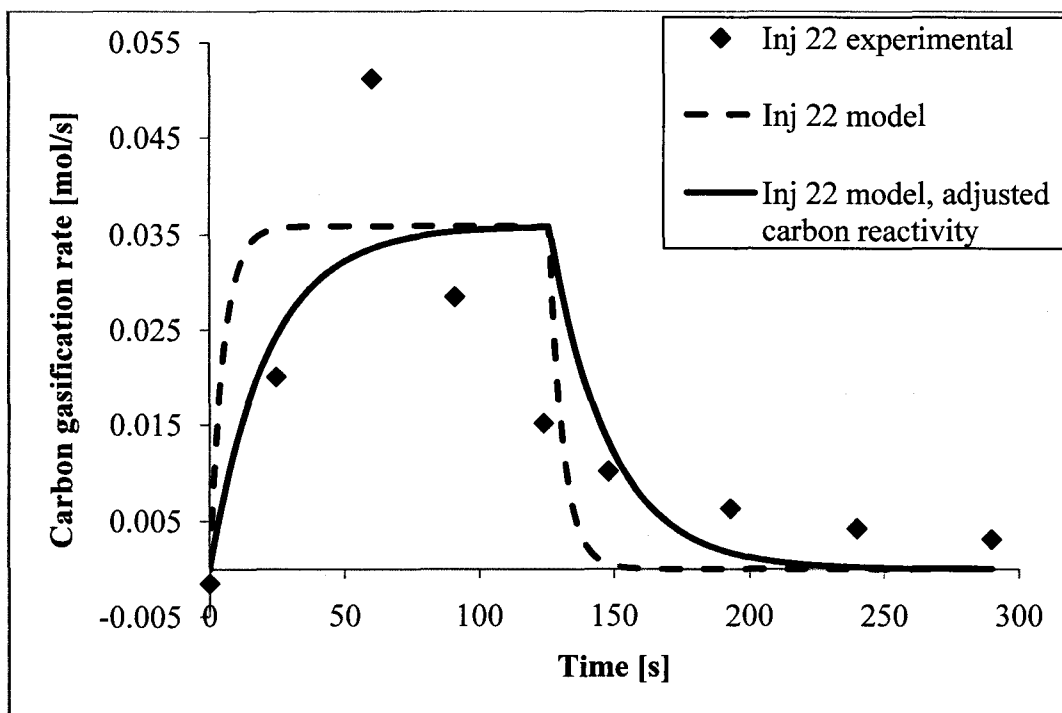
Figure 5.11 - Carbon gasification rate, experiment 22
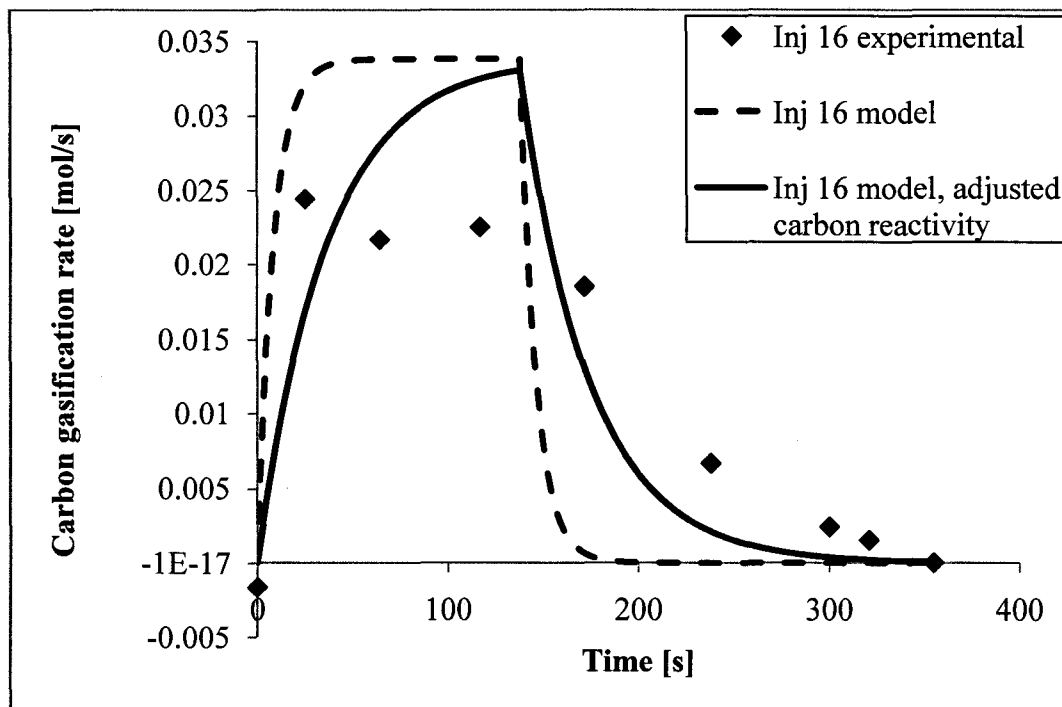
Figure 5.12 - Carbon gasification rate, experiment 16

5.1.4.3 Discussion of Injection Model

The injection model predicts that the carbon gasification rate will level off to a constant value after carbon injection has progressed for some time. This steady-state regime is characterized by:

1. Gasification rate equal to the injection rate.

2. A constant amount of residual carbon in the slag, determined by the carbon reactivity. Higher carbon reactivity will result in less residual carbon.

3. Kinetics controlled almost exclusively by the carbon-gas chemical reaction and thermodynamics controlled almost exclusively by the slag, as observed in the p_{CO_2} plots in the appendix, section A.4.

If carbon injection were to continue for an extended period of time, this steady state would not be sustainable due to decreasing slag reactivity caused by the reduction of iron from ferric to ferrous oxide and from ferrous oxide to liquid iron.

The injection model gives reasonably accurate predictions of the carbon gasification rate and amount of residual carbon in the slag. Variability in experimental injection rates and coal flotation may explain much of the misfit in the predictions of gasification rate and residual carbon. In some experiments, a large amount of coal was injected suddenly due to blockage and sudden opening of the injection lance as discussed in section 3.4. This phenomenon was apparent

in experiments 34R and 22, where it was the cause of the very high gasification rates observed part way through the injection. In experiment 34R, the overall injection rate, calculated by dividing the total amount of carbon injected by the injection time, was 0.0749 mol s^{-1}. Inspection of the coal feeder weight and internal pressure data shown in Figures 5.13 and 5.14 revealed that the injection lance became blocked at approximately 32 seconds. Pressure inside the feeder increased greatly until about 67 seconds, when the blockage cleared resulting in a drop in pressure and injection of excess coal. The actual carbon injection rate varied from 0.0805 mol s^{-1} before the blockage to 0.0312 mol s^{-1} during the blockage, increased to 0.273 mol s^{-1} immediately following the clearing of the lance, and eventually levelled off to 0.0769 mol s^{-1}. Using these revised carbon injection rates in the injection model for experiment 34R instead of the overall rate yielded a carbon gasification rate prediction that corresponded well with the experimental results, shown in Figure 5.15.
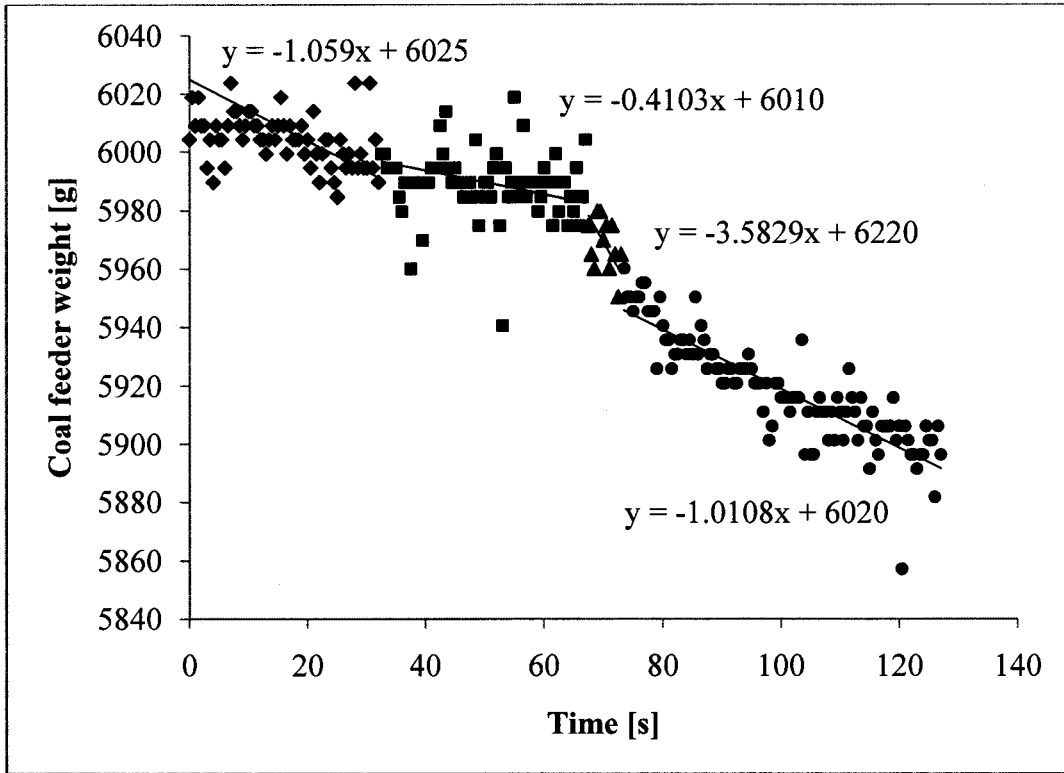
Figure 5.13 - Coal feeder weight during coal injection, experiment 34R
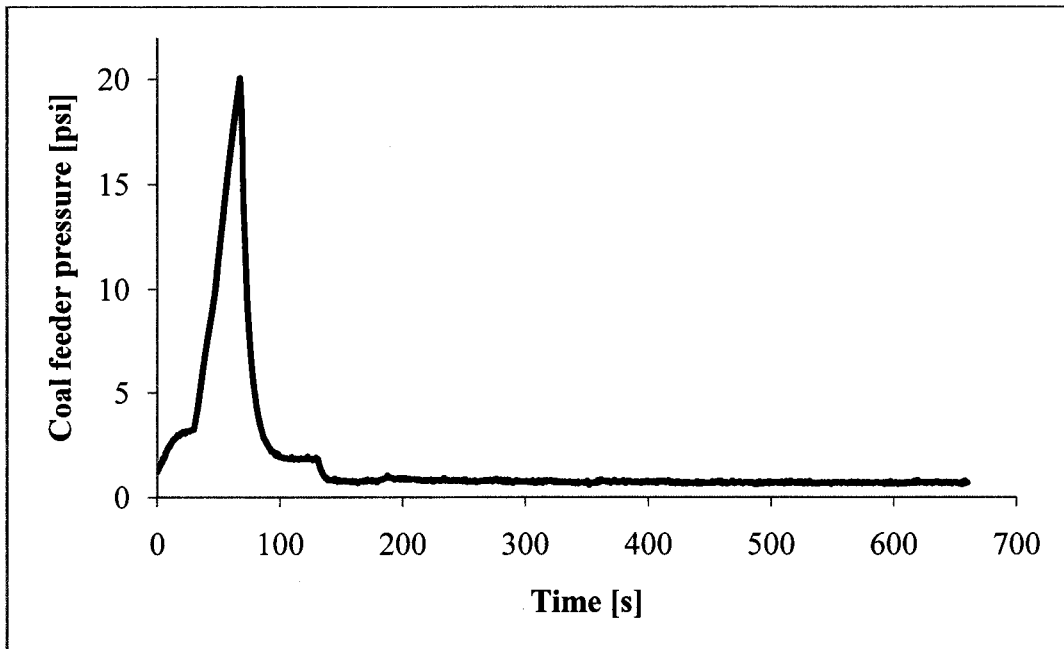
Figure 5.14 - Coal feeder pressure, experiment 34R
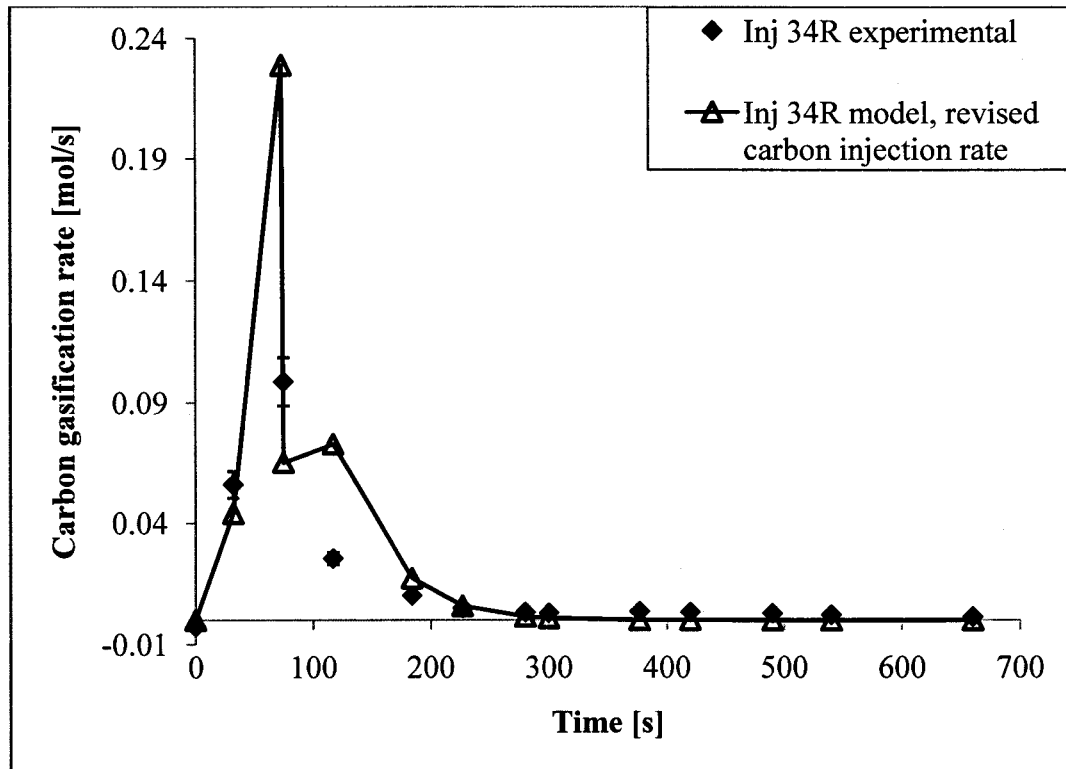
Figure 5.15 - Carbon gasification rate, experiment 34R, revised injection rate

Flotation of coal, also discussed in section 3.4, is likely the result of coal

injected into slag with a high void fraction and not immersed. It would result in

lower gasification rates than expected, as the floating coal would sit on top of the

slag and react mainly with the atmosphere in the freeboard at a slower rate than if

it were reacting with the slag, and more residual carbon would result. This was

observed dramatically in experiment 34R, where the experimental gasification

rate point at 117 seconds is much lower than expected and the residual carbon is

much higher than expected from that time onward. All of the experiments exhibit

this behaviour to some degree. The injection model is accurate in predicting the

total amount of carbon gasified over the injection process. However, optimising the model to fit the shape of the experimental data is challenging due to extensive opportunity for unpredictable experimental fluctuations.

The model tends to over-predict the CO_2 pressure during the carbon injection and under-predict it after the carbon injection has ceased. This is likely due to errors in the experimental analysis, since the gas compositions are approximated via the χ parameter, and the value of χ is assumed constant throughout the injection process. In reality, the value of χ should shift from zero to one as the rate control shifts from the slag to the carbon. The model predicts that the thermodynamics are controlled almost exclusively by the slag and that the rate is controlled almost exclusively by the carbon after about 20 seconds from the beginning of carbon injection in every case. This is because as bubbles form and grow the slag surface area, which initially was the rate limiting factor, becomes more than large enough to sustain the rate causing the carbon-gas reaction to become the limiting factor.

The reactivity of the carbon used in the present experiments appears to be lower than the metallurgical coke and greater than the electrode graphite used by Turkdogan and Vinters (1970). Adjusting the carbon reactivity through the Φ_1 term has a significant effect on the predicted gasification rate, amount of residual carbon, fraction of active slag-gas interfacial area and average bubble diameter, but very little effect on the predicted pressure of CO_2. With carbon of higher

reactivity, it is predicted that the steady-state gasification rate regime is reached more quickly, and that less residual carbon accumulates so that gasification ceases more rapidly after carbon injection has stopped. However, the steady-state gasification rate is not affected by the carbon reactivity. Thus using carbon of higher reactivity is beneficial because it enables more immediate response to changes in injection rate, giving greater control over the rate of gas flow through the slag and slag foaming.

The active fraction of slag-gas interfacial area represents the fraction of slag-gas area of a particle-bubble system that must be participating in the reaction to allow for its calculated reaction rate for the given slag reactivity at a certain point in time, averaged over all the particle-bubble systems at that time. It should be close to unity at time zero, since the slag-gas interfacial area is small and is the limiting factor in the rate. As time progresses the bubbles grow, increasing the total interfacial area, and carbon is consumed, shifting rate control to the carbon-gas reaction. Therefore less of the available slag-gas interfacial area is actually required for the reaction. There is an abrupt drop in the fraction of active area at the time when carbon injection ceases because rate control becomes even more dominated by the carbon-gas reaction at that point due to carbon starvation. In the discussion of active reaction surface area by Ji et al. (2005b), it was concluded that when the calculated active fraction of slag-gas interfacial area is less than unity, not every bubble is associated with a carbon particle, that is, there are more bubbles than particles in the slag. While it is possible that not every bubble is

associated with a carbon particle for its lifetime in the slag, as will be discussed

further in section 5.3.4, a calculation of the active fraction of slag-gas interfacial

area is not in itself sufficient proof of this. Because the slag-gas reaction is not

always rate limiting, even bubbles that contain carbon particles and are reacting

do not have a fully active slag-gas interface. There actually exists a continuum of

bubbles in various states of interfacial activity depending on their residence time

in the slag.

5.2 Rate Control

Story et al. (1998) showed that for the case of coke reacting with slag of

higher FeO contents (greater than about 10 wt % FeO), liquid phase and gas phase

mass transport become relatively unimportant to the overall rate of reaction due to

higher rates of gas evolution and the resulting stirring effect, as shown in Figure

2.1. Since the current work investigated systems which underwent violent stirring

due to the gas-producing reaction and resulting slag foaming, with slag containing

at least 21 wt% FeO, it is reasonable to conclude that both gas phase and liquid

phase mass transport had negligible effects on the rate. Therefore the rate was

under mixed control by the slag-gas and carbon-gas chemical reactions.

As can be seen in the plot of the maximum experimental carbon

gasification rate against the carbon injection rate in Figure 4.5, the gasification

rate is highly dependent on the injection rate. This indicates that kinetic control of

the carbon-slag reaction is dominated by the carbon-gas chemical reaction. The

carbon-slag reaction model discussed in section 5.1.4.3 provides further confirmation of this conclusion.

5.3 Slag Foaming

The height and stability of slag foam are dependent on the physical properties of the slag, which are in turn dependent on its composition and temperature. Greater slag viscosity will result in greater foam height and stability via longer bubble residence time. With bubbles residing in the slag longer, there will be a greater likelihood that carbon particles will react completely without floating out of the slag prematurely. Greater slag surface tension will result in lower foam height and stability since it encourages the formation of larger polyhedral bubbles.

5.3.1 Applicability of the Foaming Index

As discussed in section 2.7.1, for the foaming index to be relevant in a given system, the foam height must be linearly dependent on the superficial gas velocity over the range of superficial gas velocities encountered. In this work, foam height was observed to be linearly dependent on superficial gas velocity below a critical foam height, but above this critical value increasing superficial gas velocity gave a diminishing increase in foam height, as noted in section 4.4 and displayed in Figure 4.6. This deviation from linearity above a critical foam height will henceforth be referred to as "foaming saturation", since in essence it is caused by the liquid becoming saturated with bubbles. The foaming saturation

effect was discussed by Lahiri and Seetharaman (2002). They noted that when gas moves through a column of foaming liquid, two phases initially coexist: a lower bubble-dispersed phase, where bubbles move as individuals through the liquid, and an upper true foam. Over time the foam phase grows and the bubble-dispersed phase shrinks until they reach steady-state relative volume. The relative volume of the foam phase will increase with greater liquid foaminess and/or superficial gas velocity via longer bubble residence time in the foam or more rapid introduction of bubbles to the foam. Under the right conditions (high liquid foaminess, high superficial gas velocity, small initial liquid volume) the bubble-dispersed phase may disappear altogether, with the foam phase extending through the entire column. Lahiri and Seetharaman (2002) gave the relationship between foaming index and void fraction as follows, where α is void fraction and k_b is the rate constant for bubble rupture:

$$\Sigma = \frac{1}{\alpha k_b} \tag{5.49}$$

Therefore, if the rate constant for bubble rupture is unchanging, the foaming index of the system should decrease with increasing void fraction due to a higher rate of bubble rupture. The rate at which bubbles are added to the foam (the rate of increase of foam volume) is proportional to the superficial gas velocity. The rate of bubble rupture (the rate of decrease of foam volume) is proportional to the void fraction in the foam. As long as the bubble-dispersed phase is present, the void fraction will be approximately constant with respect to superficial gas velocity, so

foam volume and hence foam height should increase linearly with superficial gas velocity. At some critical foam height the bubble-dispersed phase will be completely consumed by the foam phase. With the bubble-dispersed phase absent, the void fraction will increase with superficial gas velocity, resulting in a higher rate of bubble rupture and a diminishing rate of increase of foam height with superficial gas velocity. When this occurs, the foaming index will become a function of superficial gas velocity as well as liquid properties.

In the present work the onset of foaming saturation occurred at a slag foam height Δh of approximately 0.16 m for temperatures between 1888 and 1900 K. For temperatures between 1941 and 1991 K, foam heights were not large enough to observe foaming saturation. Work by other researchers cited by Lahiri and Seetharaman (2002) showed evidence of foaming saturation at lower foam heights, in the range of 0.03 to 0.07 m. The difference in foam height at the onset of foaming saturation between different studies may be due to differences in initial liquid volume or bubble size. Further work is required to gain a deeper understanding of the foaming saturation phenomenon.

5.3.2 Foaming Index Models

The foaming index correlation given by Lahiri and Seetharaman (2002) gave the most reasonable predictions of the current experimental results as shown in Figure 4.7. The models of Ito and Fruehan (1989) and Zhang and Fruehan (1995) tended to under-predict the foaming index, and that of Jiang and Fruehan

(1991) predicted drastically low values. In the derivation of their correlation, Jiang and Fruehan (1991) assumed the foaming index to be independent of bubble size. Their experimental work involved bubbles produced by a nozzle with inner diameter of 1.6 mm, with observed bubble diameters between 5 and 20 mm. The bubble size was controlled by the size and shape of the gas injection nozzle, not the liquid properties (Lotun and Pilon, 2005). Bubbles generated in this way tend to be polyhedral, resulting in lower foam height compared to small spherical bubbles generated by chemical reaction (Zhang and Fruehan, 1995). Therefore, the foaming index for a given set of liquid properties measured by Jiang and Fruehan (1991) was lower than it would have been had the bubbles been small and spherical. Zhang and Fruehan (1995) observed the foaming index to be proportional to the inverse of average bubble diameter. When Jiang and Fruehan's model was extrapolated to the bubble sizes measured in the current work using the inverse proportionality, assuming an average bubble diameter of 10 mm in Jiang and Fruehan's experiments, the fit was greatly improved and was comparable to that of Lahiri and Seetharaman's model as shown in Figure 4.8. This indicates that bubble size is an important factor in determining slag foam height. With smaller bubbles, much greater foam heights can be achieved with all other factors constant, so because Ito and Fruehan (1989) and Jiang and Fruehan (1991) only worked with large bubbles under the assumption that foaming index is independent of bubble size (Ito and Fruehan, 1989), their correlations are not readily applied to the current situation. The model from Lahiri and Seetharaman

(2002) predicted foaming index well because it accounts for bubble size. It is unclear why the correlation from Zhang and Fruehan (1995) did not give accurate predictions under the current conditions, but the reason may be that it was derived by dimensional analysis using the results of many studies, most of which had foams composed of large polyhedral bubbles, whereas the correlation from Lahiri and Seetharaman (2002) was derived more rigorously from first principles.

None of the foaming index models gave predictions accurate enough to show the effect of foaming saturation on the foaming index. When foaming saturation occurs, correlations that express foaming index as a function of liquid properties should over-predict the experimentally observed foaming index.

There are a number of empirical models for foaming index, and it appears that each is applicable to the relatively narrow range of conditions for which it was developed. Under the present experimental conditions, with foams composed of small spherical bubbles generated by chemical reaction, the model from Lahiri and Seetharaman (2002) is most accurate.

5.3.3 Effect of Temperature

It was observed in the current experimental work that the foaming index and slag viscosity exhibited very similar dependence on temperature. This is in agreement with the work of Ozturk and Fruehan (1995), reviewed in section 2.7.2.2, who found the apparent activation energy for the decay of foam to be 139.6 kJ mol^{-1} and the activation energy for viscous flow of the slag to be 144.7

kJ mol^{-1}, a difference of 3.59%. For current experiments with foam heights in the range where foaming index was independent of superficial gas velocity, the values of apparent activation energy for the decay of foam and activation energy for viscous flow of the slag were 246 kJ mol^{-1} and 247 kJ mol^{-1} respectively, a difference of 0.4%. The disparity in absolute values of activation energy between this work and that of Oztuk and Fruehan may be explained by the fact that slags of different compositions were used. The nearly identical temperature dependence of foaming index and slag viscosity confirms that foaming index is highly dependent on viscosity, which in turn is dependent on temperature. The relationship between foaming index and viscosity broke down for those experiments with foam height above the critical height for foaming saturation.

5.3.4 Bubble Formation, Growth and Residence Time

There exist different possibilities for the mechanism of bubble formation and growth, and it is unclear which actually occurs in reality since bubble formation and growth has not been experimentally observed for carbon particles as small as those utilized in this work. Either a carbon particle will be associated with, and engulfed by, a single continuously growing bubble for its lifetime in the slag as described by the spherical gas halo scenario shown in Figure 5.1, or bubbles will grow until they reach some critical size and detach from the carbon particle. In the hypothetical case of bubble detachment, there are two potential mechanisms. If the critical size for detachment were small compared to the size of the carbon particle, the result could be approximated as a continuous film of

bubbles on the surface of the particle each with size equal to the critical size for detachment. As soon as a bubble detached a new one would immediately take its place, so there would be a continuous detachment/formation process occurring, and since the critical size is small the bubbles could be assumed to reach that size instantaneously. If the critical size for detachment were close to the carbon particle size, a cyclical process could occur where a few bubbles would grow simultaneously to the critical size and then detach, and a new set of bubbles would then nucleate and grow, with the process repeating until the carbon was consumed. However, the most likely scenario is that of a carbon particle surrounded by a gas halo. Carbon is not easily wet by slag and the average bubble sizes observed were much larger than the average carbon particle size; therefore it is probable that particles were engulfed by a single bubble.

Another important consideration is the rate at which bubbles travel upwards through the slag, reach the top, and rupture. In the case of a bubble containing a carbon particle, upon rupture of the bubble the carbon particle would likely float on top of the slag and react at a much slower rate in the inert (relative to the carbon) atmosphere in the freeboard. Therefore the residence time of carbon particles in the slag may be limited by the rate at which bubbles travel through the slag and rupture at the top, which is in turn dependent on the slag viscosity and surface tension, the height of the foam, and the flow rate of gas through the slag. It would be undesirable to have particle-bubble systems travel through the slag quickly enough to cause a significant portion of carbon particles to float before

fully reacting. To maximize bubble-particle residence time, a slag with high viscosity and low surface tension should be used at as low a temperature as possible in order to achieve a deep, stable foam without requiring a large gas flow rate.

5.3.5 Average Bubble Size

The average bubble diameter, d_b^{avg}, may be estimated using the correlations given by Zhang and Fruehan (1995) and Lahiri and Seetharaman (2002) as presented in equations (5.50) and (5.51), respectively,

$$\frac{\Delta h}{V_g^s} = 115\frac{\mu^{1.2}}{\sigma^{0.2}\rho d_b^{avg}} \tag{5.50}$$

$$\frac{\Delta h}{V_g^s} = 150\frac{\mu}{\rho d_b^{avg}} \tag{5.51}$$

The average bubble diameter predictions made by the above equations as well as by the injection model are compared with the experimental average bubble diameters in Figure 5.16. The average slag bubble diameter is most accurately predicted by the correlation from Lahiri and Seetharaman (2002). The correlation from Zhang and Fruehan (1995) follows a similar trend but consistently under-predicts the bubble diameter. The injection model over-predicts the bubble diameter in every case, and there are two possible explanations. One is that bubbles tend to reach a critical size and then detach from the carbon particles, instead of the scenario assumed by the injection model where one carbon particle

is associated with one bubble that grows until all the carbon in the particle is consumed. The other is that particle-bubble systems travel upwards through the slag quickly enough that they reach the top, rupture and cease to react before the bubbles reach the maximum size predicted by the injection model. The injection model assumes that particle-bubble systems reside in the slag indefinitely, which is not the case in reality.
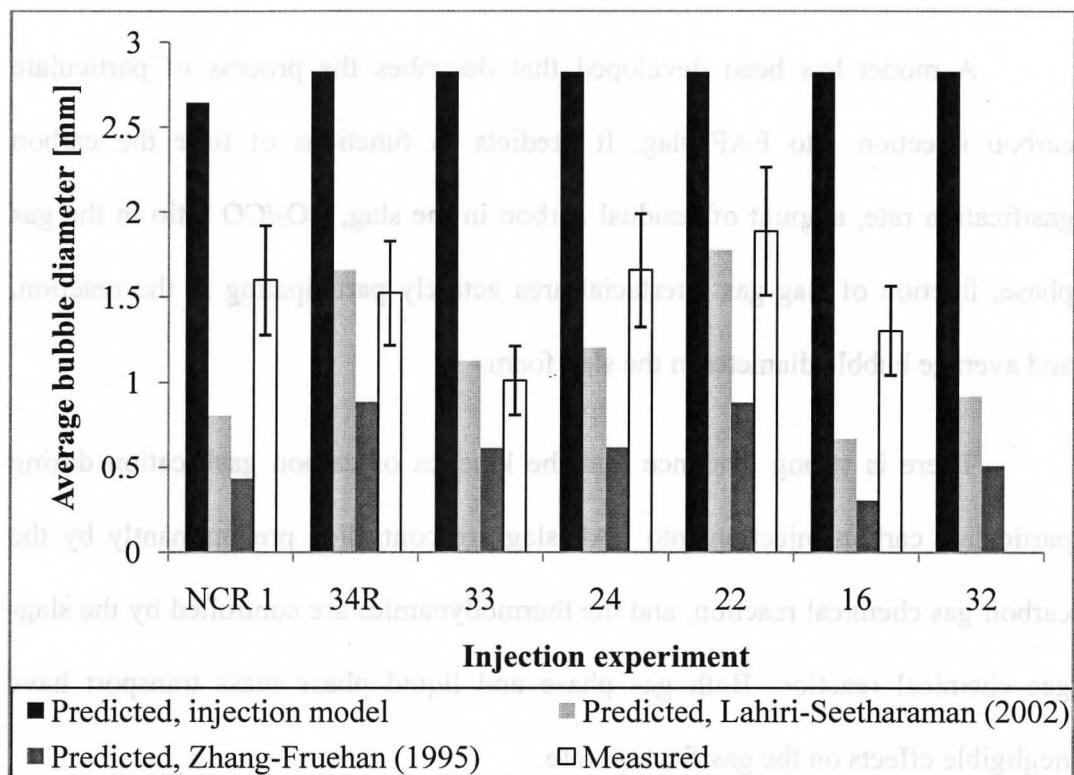
Figure 5.16 - Average bubble diameter predictions

Chapter 6: Conclusions

6.1 Conclusions

Carbon-slag reaction kinetics, slag foaming and the interplay between the two during particulate carbon injection into electric arc furnace slag have been investigated experimentally and theoretically.

A model has been developed that describes the process of particulate carbon injection into EAF slag. It predicts as functions of time the carbon gasification rate, amount of residual carbon in the slag, CO_2/CO ratio in the gas phase, fraction of slag-gas interfacial area actively participating in the reaction, and average bubble diameter in the slag foam.

There is strong evidence that the kinetics of carbon gasification during particulate carbon injection into EAF slag are controlled predominantly by the carbon-gas chemical reaction, and the thermodynamics are controlled by the slag-gas chemical reaction. Both gas phase and liquid phase mass transport have negligible effects on the gasification rate.

A steady-state gasification rate regime is reached after carbon injection has continued for some time. In this regime, gasification rate is equal to the injection rate and the kinetics are controlled by chemical reaction of the carbon. If carbon injection were to continue for an extended period of time, this steady state would not be sustainable due to decreasing slag reactivity caused by reduction of

iron oxide. In order to sustain the steady state, iron oxide would need to be replenished in the slag.

Since rate control is dominated by the chemical reaction of carbon, the reactivity of the injected carbon plays an important role in the reaction behaviour. With carbon of higher reactivity, the steady-state gasification rate regime is reached more quickly, and less residual carbon accumulates so that gasification ceases more rapidly after carbon injection has stopped. However, the steady-state gasification rate is not affected by the carbon reactivity. Thus using carbon of higher reactivity is beneficial because it would result in more immediate response to changes in injection rate, giving greater control over the rate of gas flow through the slag and slag foaming.

Another consequence of the rate control being dominated by the chemical reaction of carbon is that the slag chemistry has little effect on the carbon gasification rate, provided that the slag 'FeO' content is greater than about 21 wt% as investigated in this study. However, slag composition is vitally important to slag foaming behaviour, since the viscosity, density and surface tension of a slag are directly related to its composition. EAF slags should be designed to have high viscosity and low surface tension to ensure deep, stable foam. Since the viscosity of a slag is highly dependent on its temperature, lower temperatures promote foam stability and depth.

In an industrial EAF situation, it is important to ensure that there is a sufficient volume of liquid slag to wet injected particulate carbon. A very high void fraction in the foamed slag could result in carbon not being immersed and floating on the surface of the slag. This carbon would not contribute to foaming the slag and would therefore be wasted. Carbon should be injected at a rate such that the steady-state regime, in which gasification rate is equal to injection rate, is achieved. If the injection rate is increased without a corresponding increase in the gasification rate, this is an indication of carbon flotation, provided that the slag-gas chemical reaction has not become rate-limiting. Another possible cause of carbon flotation and wastage is particle-bubble systems travelling rapidly through the slag and rupturing before the carbon has fully reacted. To prevent this, slag with good foaming properties should be used to increase bubble residence time.

The foaming index is a useful parameter for quantifying slag foaming behaviour; however, it is only applicable when the foam void fraction is constant with respect to gas flow rate. At large foam heights the void fraction may increase with increasing superficial gas velocity, so that foaming index is no longer a function of liquid properties alone.

Bubble size is an important factor in slag foaming, with smaller average bubble diameter resulting in greater foam height and stability. Foaming index models that take bubble size into account tend to be more accurate than those which assume foaming index to be independent of bubble size. The injection model developed in this work predicted bubble sizes larger than were observed,

and there are two likely explanations: either bubbles associated with a carbon particle tended to grow until they reached a critical size and detached, or bubbles ruptured at the top of the slag before reaching the maximum size predicted by the injection model.

6.2 Future Work

It is important to understand the mechanism of bubble formation, growth and dissociation in the study of carbon-slag reactions since the bubble size determines the slag, and possibly the carbon, reaction area. The spherical gas halo mechanism has been assumed in the model derivations in this work, but it is desirable to have a more certain understanding. An experiment could be designed in which X-ray photography is used to directly observe a carbon particle reacting in a bath of molten slag and the resulting bubble behaviour.

An investigation into the role of hydrogen, present in coal volatiles, in increasing the rate of coal-slag reaction could bear much fruit. The H_2O/H_2 gas mixture is known to react more rapidly with both carbon and slag than CO_2/CO, and higher reaction rate is beneficial in increasing foaming. Thus, hydrogen in coal could be very advantageous as there is potential for a dual benefit: cost-savings by using cheaper coal with higher volatile content as well as better foaming performance.

Further study into optimising the carbon injection rate and slag properties for generating slag foam would be beneficial. The foaming saturation effect that

occurs at higher foam heights limits the maximum useful height, since attempting to increase the height beyond the critical point for saturation using greater gas flow rates is largely a wasted effort and will result in increased foam void fraction. High void fraction in the foam may result in carbon not being immersed in the slag. If bubble residence time in the slag is short due to small slag depth, high gas velocity or low liquid foaminess, premature carbon flotation may result. It is desirable to achieve maximum foam height using a minimal amount of carbon without any wasted carbon. This is achievable by using slag with good foaming properties to obtain maximum foam height with minimal gas flow rate, and ensuring that there is a sufficient volume of liquid slag to keep void fraction relatively low. Being able to predict, for a given set of conditions, the maximum useful slag height and the optimal carbon injection rate required to obtain that height would be very useful.

Bibliography

Ban-ya, S., Iguchi, Y., & Nagasaka, T. (1984). *Tetsu-to-Hagane , 70*, 1689-1696.

Barati, M., & Coley, K. (2005). *Metall. Mater. Trans. B , 36B*, 169-178.

Barati, M., & Coley, K. (2006). *Metall. Mater. Trans. B , 37B*, 61-69.

Brinkman, H. (1952). *J. Chem. Phys. , 20*, 571.

Chen, E. (2005). *M. Eng. Thesis.* McMaster University, Hamilton, ON.

El-Rahaiby, S., Sasaki, Y., Gaskell, D., & Belton, G. (1986). *Metall. Trans. B , 17B*, 307-316.

Fruehan, R., Goldstein, D., Sarma, B., Story, S., Glaws, P., & Pasewicz, H. (2000). *Metall. Mater. Trans. B , 31B*, 891-898.

Gaskell, D. (2003). *Introduction to the Thermodynamics of Materials* (4th ed.). New York, NY: Taylor & Francis.

Geiger, G., & Poirier, D. (1937). *Transport Phenomena in Metallurgy.* New York, NY: Addison-Wesley Publishing Co., 463-471.

Glaws, P., & Belton, G. (1990). *Metall. Trans. B , 21B*, 511-519.

Goel, R., & Kellogg, H. (1984). In H. Fine, & D. Gaskell (Ed.), *Proc. 2nd Int. Symp. on Metallurgical Slags and Fluxes* (pp. 347-355). Warrendale, PA: TMS-AIME.

Gulbransen, E., Andrew, K., & Brassort, F. (1965). *Carbon , 2*, 421-429.

Guo, D. (1984). *Archiv Fur Das Eisenhuttenwesen , 55*, 183-188.

Happel, J. (1957). *J. Appl. Phys. , 28*, 1288-1292.

Harrison, T.S.; Group Chemical Laboratories, British Steel Corporation. (1979). *Handbook of Analytical Control of Iron and Steel Production.* Chichester, England: Ellis Horwood Limited.

Hayes, P. (1979). *Metall. Trans. B , 10B*, 211-217.

Iida, T., Sakai, H., Kita, Y., & Shigeno, K. (2000). *ISIJ International , 40*, Supplement, S110-S114.

Irons, G. (2005a). *Howe Memorial Lecture, AISTech.* Charlotte, NC.

Irons, G. (2005b, July). *AIST Trans. ,* 111-123.

Ito, K., & Fruehan, R. (1989). *Metall. Trans. B , 20B*, 509-521.

Ji, F.-Z., Barati, M., Coley, K., & Irons, G. (2002). *60th Electric Arc Furnace Conference Proceedings, ISS,* (pp. 14-27). San Antonio, Texas.

Ji, F.-Z., Barati, M., Coley, K., & Irons, G. (2003). *ISS Tech 2003 Conference Proceedings,* (pp. 703-711). Indianapolis, IN.

Ji, F.-Z., Barati, M., Coley, K., & Irons, G. (2004). *VII International Conference on Molten Slags, Fluxes and Salts,* (pp. 399-405). South Africa.

Ji, F.-Z., Barati, M., Coley, K., & Irons, G. (2005a). *CMQ , 44*, 85-94.

Ji, F.-Z., Coley, K., & Irons, G. (2005b). *Conference of AIStech 2005 and ICS2005, ICS2005 Proceedings*, (pp. 423-430). Charlotte, NC.

Jiang, R., & Fruehan, R. (1991). *Metall. Mater. Trans. B , 22B*, 481-489.

Jung, S., & Fruehan, R. (2000). *ISIJ International , 40*, 348-355.

Kondratiev, A., & Jak, E. (2001). *Metall. Mater. Trans. B , 32B*, 1015-1025.

Lahiri, A., & Seetharaman, S. (2002). *Metall. Mater. Trans. B , 33B*, 499-502.

Li, Y., & Ratchev, I. (2002). *Metall. Mater. Trans. B , 33B*, 651-660.

Li, Y., Ratchev, I., Lucas, J., Evans, G., & Belton, G. (2000). *Metall. Mater. Trans. B , 31B*, 1049-1057.

Lotun, D., & Pilon, L. (2005). *ISIJ International , 45*, 835-840.

Matsuura, H., Ishida, I., & Tsukihashi, F. (2004). *ISIJ International , 44*, 1494-1500.

Meschter, P., & Grabke, H. (1979). *Metall. Trans. B , 10B*, 323-329.

Mills, K., & Keene, B. (1987). *Int. Mater. Rev. , 32*, 1-120.

Min, D., Han, J., & Chung, W. (1999). *Metall. Mater. Trans. B , 30B*, 215-221.

Morales, R., Lule, R., Lopez, F., Camacho, J., & Romero, J. (1995). *ISIJ International , 35*, 1054-1062.

Morales, R., Rodriguez, H., & Conejo, A. (2001). *ISIJ International , 41*, 426-435.

Morales, R., Rodriguez, H., Garnica, P., & Romero, A. (1997). *ISIJ International, 37*, 1072-1080.

Mori, M., Morita, K., & Sano, N. (1996). *ISIJ International , 36*, 624-630.

Mullins, W. (1992). *Surf. Sci. Lett. , 262*, L144-L146.

Nagasaka, T. (1985). *Ph.D. Thesis.* Tohoku University, Sendai, Japan.

Nagasaka, T., Hino, M., & Ban-ya, S. (2000). *Metall. Mater. Trans. B , 31B*, 945-955.

Ogawa, Y., Huin, D., Gaye, H., & Tokumitsu, N. (1993). *ISIJ International , 33*, 224-232.

Oltmann, H., & Pretorius, E. (n.d.). Simulation of the Refining Stage of the EAF Process. *Process Tech. Group, LWB Refractories .*

Ozturk, B., & Fruehan, R. (1995). *Metall. Mater. Trans. B , 26B*, 1086-1088.

Pilon, L., & Viskanta, R. (2004). *Chem. Eng. Process. , 43*, 149-160.

Platts, M. (n.d.). Retrieved July 2008, from American Coke and Coal Chemicals Institute: www.accci.org/Byproduct.pdf

Pollard, R., & Present, R. (1948). *Phys. Rev. , 73*, 762-774.

Riboud, P., Roux, Y., Lucas, L., & Gaye, H. (1981). *Fachber. Huttenprax. Metallweiterverarb.* , *19*, 859-869.

Rodriguez, H., Conejo, A., & Morales, R. (2001). *Steel Res.* , *72*, 298-303.

Sahajwalla, V., Hong, L., & Saha-Chaudhury, N. (2006). *Iron and Steel Technology* , *3*, 91-96.

Sahajwalla, V., Rahman, M., Hong, L., & Saha-Chaudhury, N. (2006). *Iron and Steel Technology* , *3*, 54-63.

Sarma, B., Cramb, A., & Fruehan, R. (1996). *Metall. Mater. Trans. B* , *27B*, 717-730.

Sasaki, Y., & Belton, G. (1983). *Metall. Trans. B* , *14B*, 267-272.

Sasaki, Y., & Belton, G. (1986). In D. Gaskell, J. Hoffman, J. Hager, & P. Mackey (Ed.), *The Reinhardt Schuhmann Int. Symp. on Innovative Technology and Reactor Design in Extractive Metallurgy* (pp. 583-595). Warrendale, PA: TMS-AIME.

Sasaki, Y., Hara, S., Gaskell, D., & Belton, G. (1984). *Metall. Trans. B* , *15B*, 563-571.

Sommerville, I., & Yang, Y. (2001). *AusIMM Proceedings* , *306*, 71-77.

Sosinsky, D., & Sommerville, I. (1986). *Metall. Trans. B* , *17B*, 331-337.

Story, S., & Fruehan, R. (2000). *Metall. Mater. Trans. B* , *31B*, 43-54.

Story, S., Sarma, B., Fruehan, R., Cramb, A., & Belton, G. (1998). *Metall. Mater. Trans. B , 29B*, 929-932.

Sun, S. (1988). *Ph.D. Thesis.* University of Newcastle, Newcastle, Australia.

Thiele, E. (1939). *Ind. Eng. Chem. , 31*, 916-920.

Tien, R., & Turkdogan, E. (1970). *Carbon , 8*, 607-621.

Turkdogan, E., & Vinters, J. (1969). *Carbon , 7*, 101-117.

Turkdogan, E., & Vinters, J. (1970). *Carbon , 8*, 39-53.

Turkdogan, E., Koump, V., Vinters, J., & Perzak, T. (1968). *Carbon , 6*, 467-484.

Urbain, G. (1987). *Steel Res. , 58*, 111-115.

Urbain, G., Cambier, F., Deletter, M., & Anseau, M. (1981). *Trans. J. Br. Ceram. Soc. , 80*, 139-141.

Warczok, A., & Utigard, T. (2000). *Steel Res. , 71*, 277-280.

Weisz, P., & Schwartz, A. (1962). *J. Catal. , 1*, 399-406.

Winkler, T., & Chipman, J. (1946). *Trans. Amer. Inst. min. metallurg. Engrs. , 167*, 111-133.

Xie, D., & Belton, G. (2003). *Metall. Mater. Trans. B , 34B*, 225-234.

Youngquist, G. (1970). *Flow through Porous Media.* Washignton, DC: American Chemical Society Publications, pp. 57-69.

Zhang, L., & Jahanshahi, S. (1998). *Metall. Mater. Trans. B , 29B*, 177-195.

Zhang, Y. (1992). *Ph.D. Thesis.* Carnegie Mellon University, Pittsburgh, PA.

Zhang, Y., & Fruehan, R. (1995). *Metall. Mater. Trans. B , 26B*, 803-812.

Appendix

A.1 Experimental

The experimental conditions for the injection experiments analysed in this work are given in Table A.1. The measured compositions of the molten slag just before coal injection began are given in Table A.2 and the slag compositions after calculating the Fe_2O_3 content using the model by Guo (1984) and normalizing to 100% are given in Table A.3. The measured gas compositions, modified volumetric fractions, flow rates of N_2 from coal and carrier gas (Q_{N_2}), flow rates of H_2 from coal (Q_{H_2}), and calculated gasification rates of carbon (Q_C) are given in Table A.4 to Table A.24. The carbon balances for all injection experiments are plotted in Figure A.1 to Figure A.7.

Table A.1 - Injection experimental conditions

	NCR 1	34R	33	32	24	22	16
Temperature [K]	1900	1900	1895	1888	1959	1941	1991
Total coal injected [g]	71.0	125	89.5	41.5	56.3	59.8	61.5
Injection duration [s]	138	127	120	80	126	126	138
Carbon injection rate [mol s^{-1}]	0.0352	0.0749	0.0566	0.0391	0.0338	0.0359	0.0338
N_2 carrier gas flow rate [Nl min^{-1}]	7.77	7.64	7.85	7.90	7.86	9.61	8.00
Slag weight [kg]	3.57	3.57	3.60	3.59	3.63	5.32	5.89
Experimental χ	0.26	0.13	0.26	0.27	0.19	0.11	0.23

Table A.2 - Measured slag compositions

	NCR 1	34R	33	32	24	22	16
wt% SiO_2	20.43	19.34	21.24	23.38	22.64	17.78	6.52
wt% P_2O_5	0.28	0.34	-	-	-	-	0.20
wt% Al_2O_3	5.84	5.92	5.80	5.85	4.80	5.06	3.94
wt% CaO	36.69	37.04	36.25	35.67	42.10	23.10	31.14
wt% MgO	7.98	7.93	7.29	7.26	7.60	10.46	7.17
wt% MnO	2.12	2.20	0.77	0.79	0.49	0.46	0.98
wt% FeO	26.23	26.22	26.82	24.98	21.60	40.76	48.18

Table A.3 - Slag compositions after applying model by Guo (1984)

	NCR 1	34R	33	32	24	22	16
wt% SiO_2	20.52	19.54	21.63	23.87	22.82	18.21	6.65
wt% P_2O_5	0.28	0.35	0.00	0.00	0.00	0.00	0.20
wt% Al_2O_3	5.87	5.98	5.91	5.97	4.84	5.18	4.01
wt% CaO	36.85	37.41	36.92	36.42	42.43	23.66	31.73
wt% MgO	8.02	8.01	7.43	7.42	7.66	10.72	7.30
wt% MnO	2.13	2.22	0.79	0.81	0.49	0.47	1.00
wt% FeO	21.92	21.85	22.92	21.73	17.94	36.88	39.60
wt% Fe_2O_3	4.42	4.63	4.40	3.78	3.83	4.87	9.50

Table A.4 - Experiment "Nucor 1" measured gas composition

Time [s]	$\%CO_2$	$\%O_2$	$\%N_2$	%CO	$\%H_2$
0	1.60	17.7	80.7	0.00	0.00
30	9.90	0.00	22.1	58.2	9.73
70	8.44	2.42	25.3	56.4	7.43
110	7.04	0.97	20.6	63.1	8.22
150	6.54	3.93	44.1	42.1	3.28
190	9.98	4.57	60.8	23.3	1.41
240	8.74	7.76	74.2	8.78	0.488
299	11.2	7.71	78.0	2.95	0.114
320	5.08	8.32	83.8	2.66	0.113
415	6.24	10.3	81.1	2.25	0.0602

Table A.5 - Experiment "Nucor 1" modified volumetric fractions

Time [s]	CO_2'	O_2'	N_2'	CO'	H_2'
0	0.0548	0.162	0.822	-0.0385	0.00
30	0.0526	0.0221	0.216	0.614	0.0951
70	0.0530	0.0389	0.249	0.586	0.0732
110	0.0534	0.0179	0.205	0.643	0.0815
150	0.0535	0.0449	0.439	0.431	0.0326
190	0.0526	0.0672	0.594	0.273	0.0138
240	0.0529	0.0928	0.730	0.119	0.00480
299	0.0523	0.103	0.758	0.0856	0.00111
320	0.0539	0.0819	0.839	0.0237	0.00113
415	0.0536	0.107	0.808	0.0309	0.000599

Table A.6 - Flow rates of N_2 and H_2 and gasification rate of carbon for experiment "Nucor 1"

Time [s]	Q_{N2} [mol s^{-1}]	Q_{H2} [mol s^{-1}]	Q_C [mol s^{-1}]
0	0.00611	0.00373	-0.00326
30	0.00611	0.00373	0.0312
70	0.00611	0.00373	0.0386
110	0.00611	0.00373	0.0309
150	0.00578	0	0.0111
190	0.00578	0	0.00573
240	0.00578	0	0.00268
299	0.00578	0	0.00218
320	0.00578	0	0.000856
415	0.00578	0	0.00121

Table A.7 - Experiment 34R measured gas composition

Time [s]	%CO_2	%O_2	%N_2	%CO	%H_2
0	2.73	16.9	80.4	0.00	0.00
32	11.3	0.561	25.8	61.9	0.430
75	4.95	0.727	12.3	72.0	10.1
117	4.38	1.78	25.1	61.1	7.62
184	8.31	3.81	50.7	35.8	1.40
227	13.6	5.00	69.2	11.7	0.481
280	14.3	5.24	75.7	4.62	0.133
300	13.7	5.48	76.4	4.38	0.0845
377	13.2	5.38	73.5	7.69	0.172
420	12.2	7.51	75.7	4.60	0.0712
490	13.4	6.24	77.3	3.01	0.0544
540	10.7	7.82	79.3	2.17	0.0367
660	8.49	9.09	82.4	0.00	0.00

Table A.8 - Experiment 34R modified volumetric fractions

Time [s]	CO_2'	O_2'	N_2'	CO'	H_2'
0	0.0261	0.169	0.803	0.00127	0.00
32	0.0250	0.0468	0.247	0.677	0.00412
75	0.0258	0.0188	0.121	0.734	0.0999
117	0.0258	0.0264	0.249	0.623	0.0755
184	0.0253	0.0648	0.493	0.403	0.0136
227	0.0247	0.0996	0.655	0.216	0.00456
280	0.0246	0.105	0.715	0.155	0.00125
300	0.0247	0.104	0.724	0.146	0.000801
377	0.0248	0.102	0.698	0.174	0.00163
420	0.0249	0.117	0.722	0.135	0.000680
490	0.0247	0.111	0.733	0.131	0.000516
540	0.0251	0.114	0.762	0.0987	0.000353
660	0.0253	0.117	0.801	0.0571	0.00

Table A.9 - Flow rates of N₂ and H₂ and gasification rate of carbon for experiment 34R

Time [s]	Q_{N2} [mol s^{-1}]	Q_{H2} [mol s^{-1}]	Q_C [mol s^{-1}]
0	0.00601	0.00366	-0.00268
32	0.00601	0.00366	0.0558
75	0.00601	0.00366	0.0987
117	0.00601	0.00366	0.0254
184	0.00568	0	0.0101
227	0.00568	0	0.00495
280	0.00568	0	0.00320
300	0.00568	0	0.00294
377	0.00568	0	0.00360
420	0.00568	0	0.00325
490	0.00568	0	0.00280
540	0.00568	0	0.00212
660	0.00568	0	0.00130

Table A.10 - Experiment 33 measured gas composition

Time [s]	%CO_2	%O_2	%N_2	%CO	%H_2
0	2.43	12.5	84.9	0.05	0.140
30	7.89	0.540	16.3	67.5	7.79
65	6.73	1.65	16.7	67.4	7.50
100	5.75	1.55	17.5	66.6	8.58
165	8.05	4.89	56.4	28.7	1.96
220	5.76	6.74	57.3	28.3	1.93
280	9.16	6.61	68.4	14.9	0.910
300	10.0	5.83	69.6	13.6	0.920
363	7.98	7.62	74.9	8.83	0.650
420	4.46	6.97	78.1	9.91	0.550

Table A.11 - Experiment 33 modified volumetric fractions

Time [s]	CO_2'	O_2'	N_2'	CO'	H_2'
0	0.0571	0.111	0.862	-0.0319	0.00142
30	0.0556	0.0166	0.161	0.690	0.0770
65	0.0559	0.0219	0.166	0.681	0.0746
100	0.0562	0.0161	0.175	0.667	0.0858
165	0.0555	0.0603	0.557	0.308	0.0194
220	0.0562	0.0680	0.572	0.284	0.0193
280	0.0552	0.0823	0.672	0.182	0.00894
300	0.0550	0.0787	0.681	0.176	0.00900
363	0.0556	0.0870	0.740	0.111	0.00642
420	0.0565	0.0643	0.786	0.0880	0.00553

Table A.12 - Flow rates of N₂ and H₂ and gasification rate of carbon for experiment 33

Time [s]	Q_{N2} [mol s^{-1}]	Q_{H2} [mol s^{-1}]	Q_C [mol s^{-1}]
0	0.00608	0.00277	-0.00241
30	0.00608	0.00277	0.0480
65	0.00608	0.00277	0.0562
100	0.00608	0.00277	0.0404
165	0.00584	0	0.00677
220	0.00584	0	0.00663
280	0.00584	0	0.00396
300	0.00584	0	0.00364
363	0.00584	0	0.00244
420	0.00584	0	0.00161

Table A.13 - Experiment 32 measured gas composition

Time [s]	%CO₂	%O₂	%N₂	%CO	%H₂
0	0.930	14.7	84.3	0.07	0.00
30	10.8	0.880	30.3	49.2	8.81
65	9.29	0.140	20.0	63.5	7.07
90	9.45	3.63	40.6	42.9	3.38
140	8.49	5.81	60.8	22.9	2.01
160	10.1	6.56	67.5	14.5	1.35
220	6.78	4.01	55.5	30.7	3.03
280	8.57	6.47	73.7	10.2	1.09
300	8.57	6.26	75.4	8.89	0.850
370	5.15	10.8	78.3	5.51	0.270

Table A.14 - Experiment 32 modified volumetric fractions

Time [s]	CO_2'	O_2'	N_2'	CO'	H_2'
0	0.0672	0.122	0.868	-0.0569	0.00000
30	0.0639	0.0295	0.296	0.524	0.0863
65	0.0644	0.0150	0.198	0.653	0.0698
90	0.0644	0.0502	0.401	0.451	0.0333
140	0.0646	0.0673	0.602	0.246	0.0199
160	0.0641	0.0820	0.663	0.178	0.0133
220	0.0652	0.0413	0.554	0.309	0.0303
280	0.0646	0.0742	0.730	0.121	0.0108
300	0.0646	0.0721	0.747	0.108	0.00841
370	0.0657	0.101	0.789	0.0416	0.00272

Table A.15 - Flow rates of N_2 and H_2 and gasification rate of carbon for experiment 32

Time [s]	Q_{N2} [mol s^{-1}]	Q_{H2} [mol s^{-1}]	Q_C [mol s^{-1}]
0	0.00605	0.00193	-0.00178
30	0.00605	0.00193	0.0201
65	0.00605	0.00193	0.0318
90	0.00587	0	0.0152
140	0.00587	0	0.00555
160	0.00587	0	0.00423
220	0.00587	0	0.00596
280	0.00587	0	0.00256
300	0.00587	0	0.00224
370	0.00587	0	0.00159

Table A.16 - Experiment 24 measured gas composition

Time [s]	%CO_2	%O_2	%N_2	%CO	%H_2
0	0.770	17.2	81.4	0.670	0
25	8.54	4.88	37.2	48.8	0
69	7.33	5.10	35.5	51.5	0
99	6.75	3.92	35.7	53.0	0
126	5.84	5.45	39.9	48.3	0
174	5.60	8.84	59.4	25.6	0
234	4.79	11.7	74.5	8.46	0
295	3.49	12.8	77.1	6.07	0

Table A.17 - Experiment 24 modified volumetric fractions

Time [s]	CO_2'	O_2'	N_2'	CO'	H_2'
0	0.0405	0.158	0.827	-0.0258	0
25	0.0391	0.0704	0.366	0.525	0
69	0.0394	0.0670	0.351	0.542	0
99	0.0395	0.0526	0.354	0.553	0
126	0.0397	0.0635	0.398	0.499	0
174	0.0397	0.0963	0.592	0.272	0
234	0.0399	0.121	0.746	0.0929	0
295	0.0402	0.126	0.777	0.0562	0

Table A.18 - Flow rates of N₂ and H₂ and gasification rate of carbon for experiment 24

Time [s]	Q_{N2} [mol s^{-1}]	Q_{H2} [mol s^{-1}]	Q_C [mol s^{-1}]
0	0.00599	0.00166	-0.00128
25	0.00599	0.00166	0.0317
69	0.00599	0.00166	0.0334
99	0.00599	0.00166	0.0211
126	0.00599	0.00166	0.0187
174	0.00584	0	0.00790
234	0.00584	0	0.00267
295	0.00584	0	0.00187

Table A.19 - Experiment 22 measured gas composition

Time [s]	%CO₂	%O₂	%N₂	%CO	%H₂
0	0.930	15.2	83.2	0.00	0
25	8.90	6.61	50.9	33.0	0
60	20.1	6.65	62.3	10.3	0
91	19.4	7.34	65.7	6.98	0
124	18.9	8.06	70.3	2.11	0
148	12.8	11.7	73.4	1.47	0
193	9.11	13.2	75.0	2.09	0
240	5.87	14.8	76.3	2.44	0
290	4.54	14.8	77.0	2.99	0

Table A.20 - Experiment 22 modified volumetric fractions

Time [s]	CO$_2$'	O$_2$'	N$_2$'	CO'	H$_2$'
0	0.0257	0.146	0.845	-0.0162	0
25	0.0246	0.0955	0.496	0.384	0
60	0.0234	0.143	0.576	0.258	0
91	0.0234	0.146	0.609	0.221	0
124	0.0235	0.151	0.653	0.172	0
148	0.0242	0.161	0.702	0.112	0
193	0.0246	0.161	0.730	0.0845	0
240	0.0250	0.163	0.754	0.0572	0
290	0.0252	0.158	0.767	0.0498	0

Table A.21 - Flow rates of N$_2$ and H$_2$ and gasification rate of carbon for experiment 22

Time [s]	Q_{N2} [mol s^{-1}]	Q_{H2} [mol s^{-1}]	Q_C [mol s^{-1}]
0	0.00730	0.00177	-0.00153
25	0.00730	0.00177	0.0200
60	0.00730	0.00177	0.0512
91	0.00730	0.00177	0.0284
124	0.00730	0.00177	0.0152
148	0.00715	0	0.0101
193	0.00715	0	0.00627
240	0.00715	0	0.00420
290	0.00715	0	0.00307

Table A.22 - Experiment 16 measured gas composition

Time [s]	%CO$_2$	%O$_2$	%N$_2$	%CO	%H$_2$
0	0.00730	16.6	83.4	0.00	0
25	8.71	8.30	52.5	30.5	0
64	7.50	8.28	51.5	32.8	0
117	12.1	7.42	55.7	24.8	0
172	13.0	6.88	57.5	22.3	0
238	4.75	15.7	73.3	5.98	0
300	0.240	19.3	77.2	3.22	0
321	1.48	18.0	78.8	1.80	0
355	0.00700	12.4	87.6	0.00	0

Table A.23 - Experiment 16 modified volumetric fractions

Time [s]	CO$_2$'	O$_2$'	N$_2$'	CO'	H$_2$'
0	0.0233	0.157	0.843	-0.0232	0
25	0.0223	0.111	0.508	0.358	0
64	0.0225	0.106	0.501	0.370	0
117	0.0220	0.117	0.531	0.330	0
172	0.0219	0.117	0.547	0.315	0
238	0.0228	0.168	0.726	0.0835	0
300	0.0233	0.185	0.780	0.0117	0
321	0.0231	0.176	0.791	0.00979	0
355	0.0233	0.114	0.886	-0.0232	0

Table A.24 - Flow rates of N$_2$ and H$_2$ and gasification rate of carbon for experiment 16

Time [s]	Q$_{N2}$ [mol s^{-1}]	Q$_{H2}$ [mol s^{-1}]	Q$_C$ [mol s^{-1}]
0	0.00610	0.00166	-0.00166
25	0.00610	0.00166	0.0244
64	0.00610	0.00166	0.0217
117	0.00610	0.00166	0.0225
172	0.00595	0	0.0185
238	0.00595	0	0.00666
300	0.00595	0	0.00242
321	0.00595	0	0.00152
355	0.00595	0	0.00
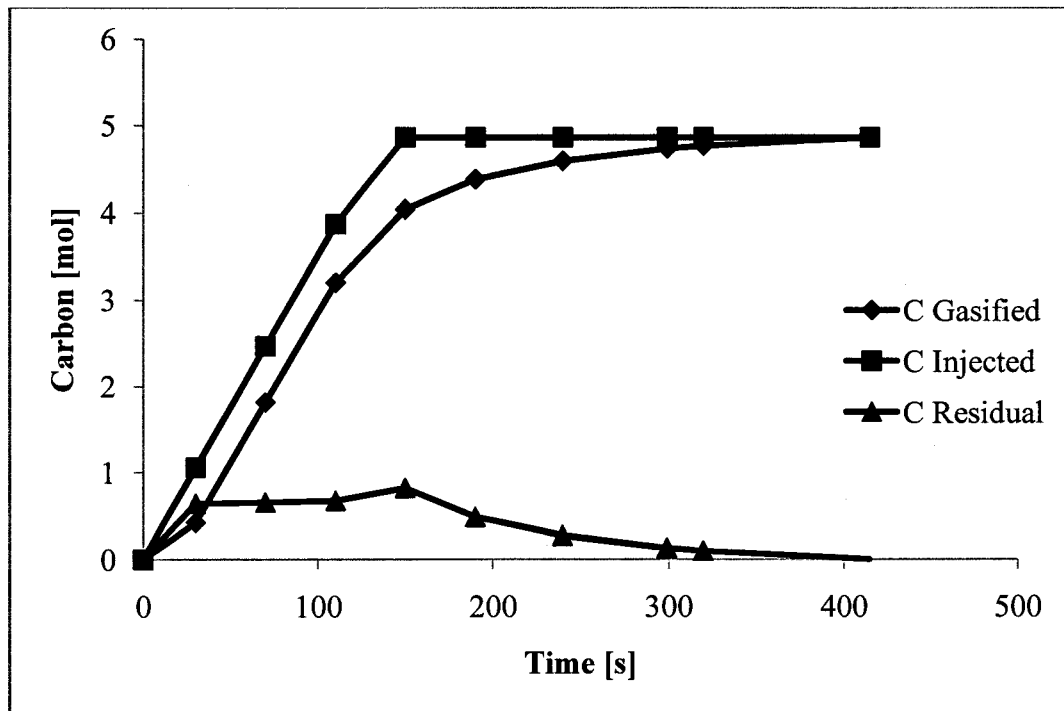
Figure A.1 - Experiment "Nucor 1" carbon balance
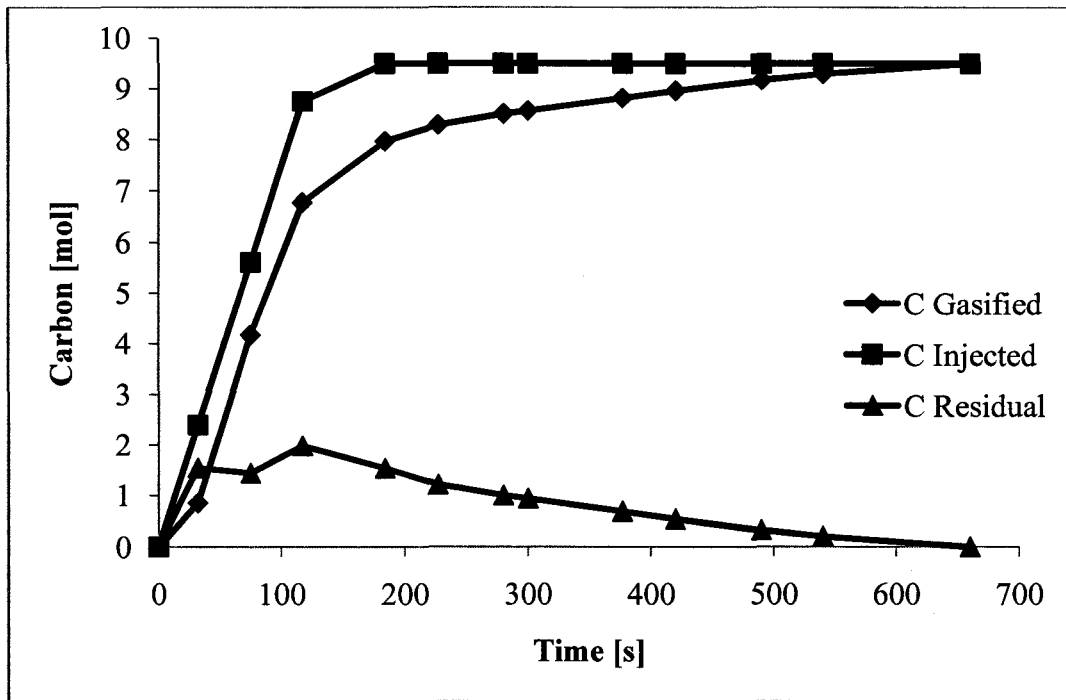
Figure A.2 - Experiment 34R carbon balance
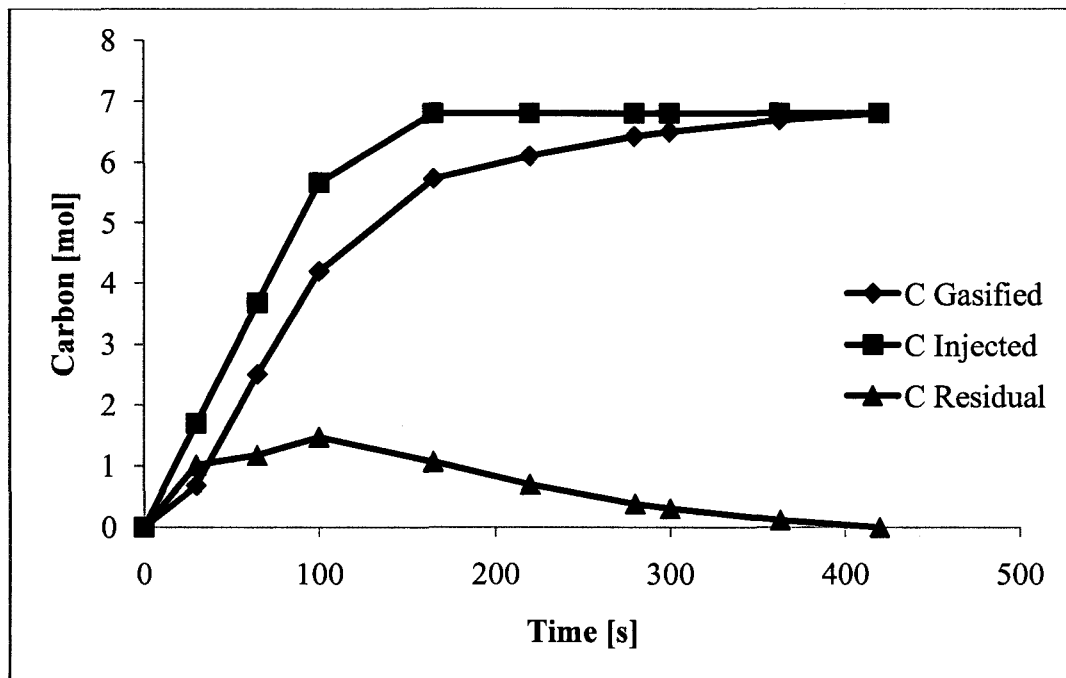
Figure A.3 - Experiment 33 carbon balance
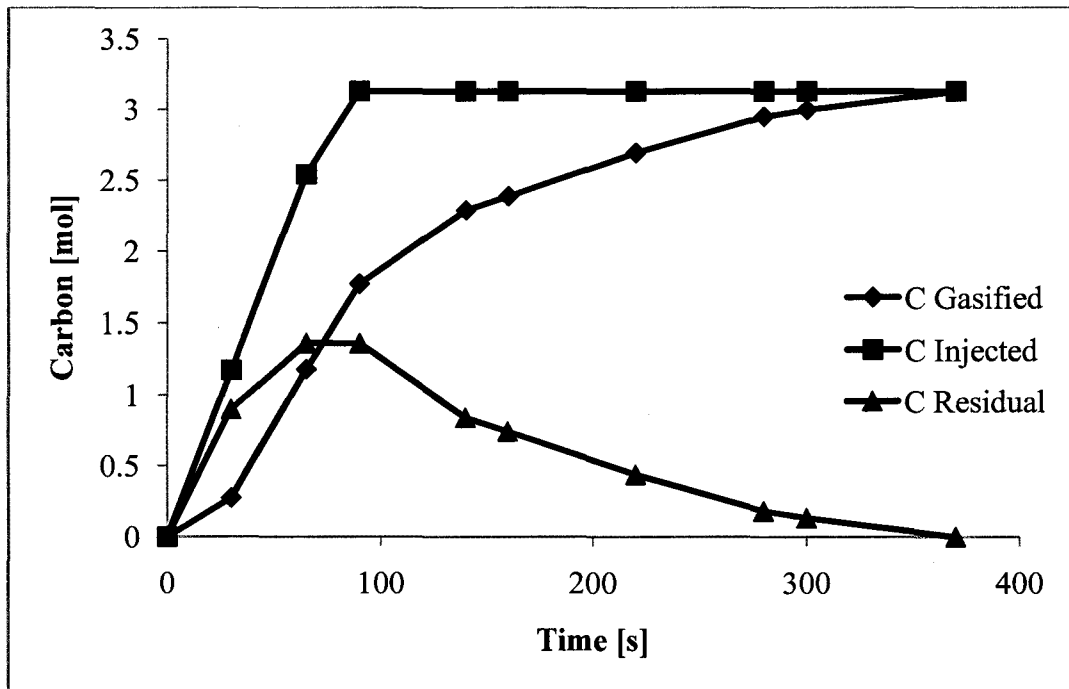
Figure A.4 - Experiment 32 carbon balance
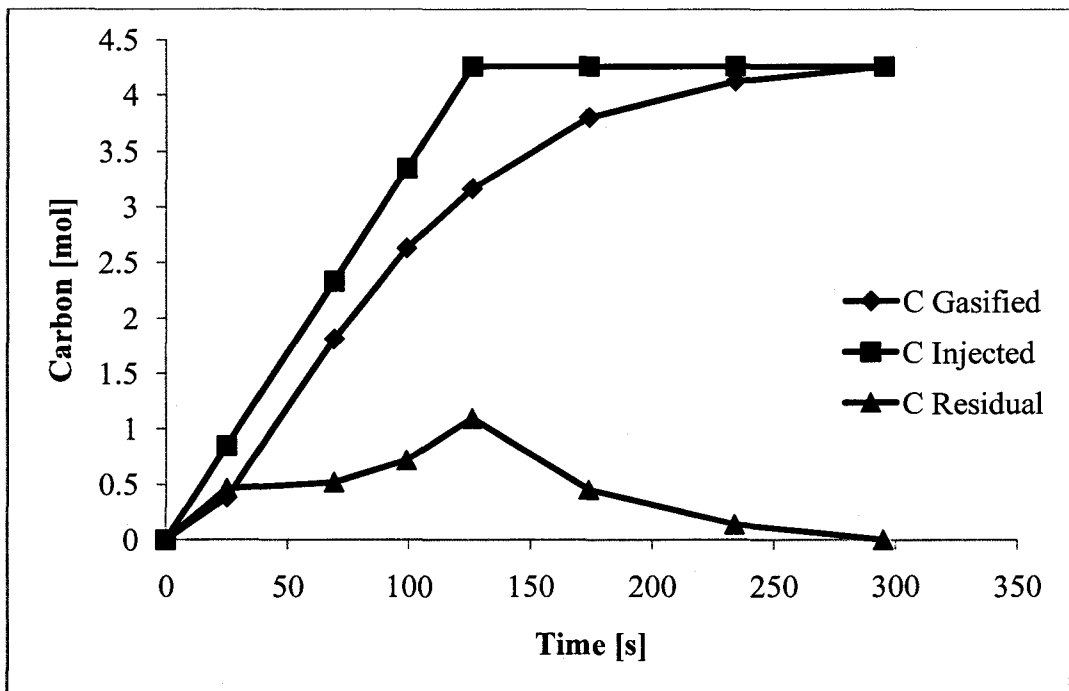
Figure A.5 - Experiment 24 carbon balance
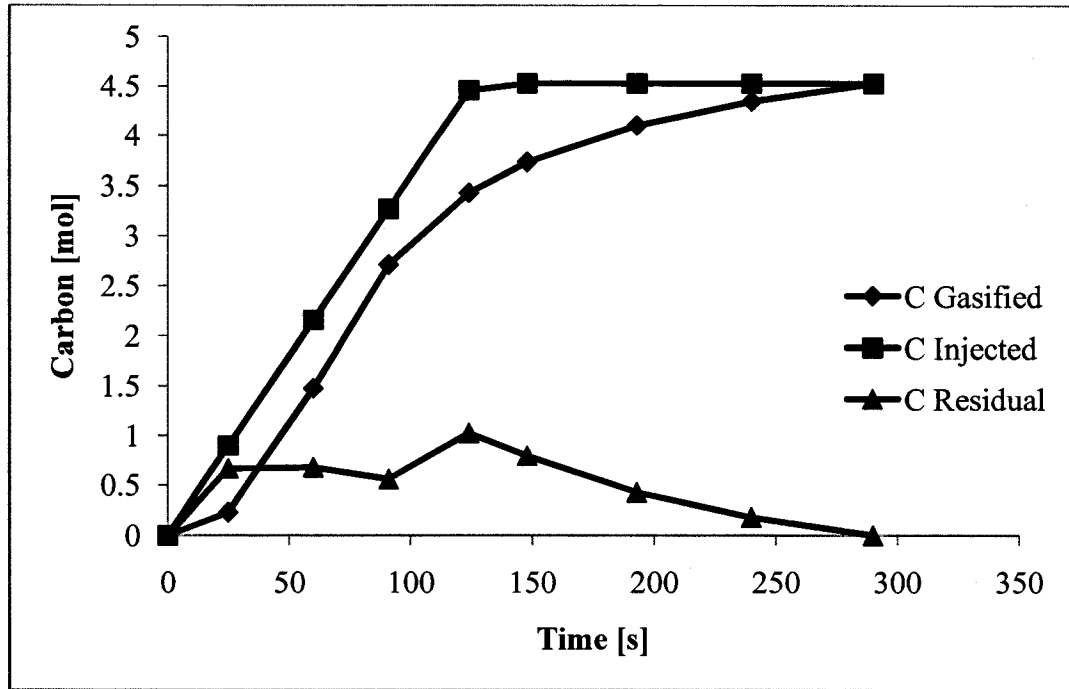
Figure A.6 - Experiment 22 carbon balance
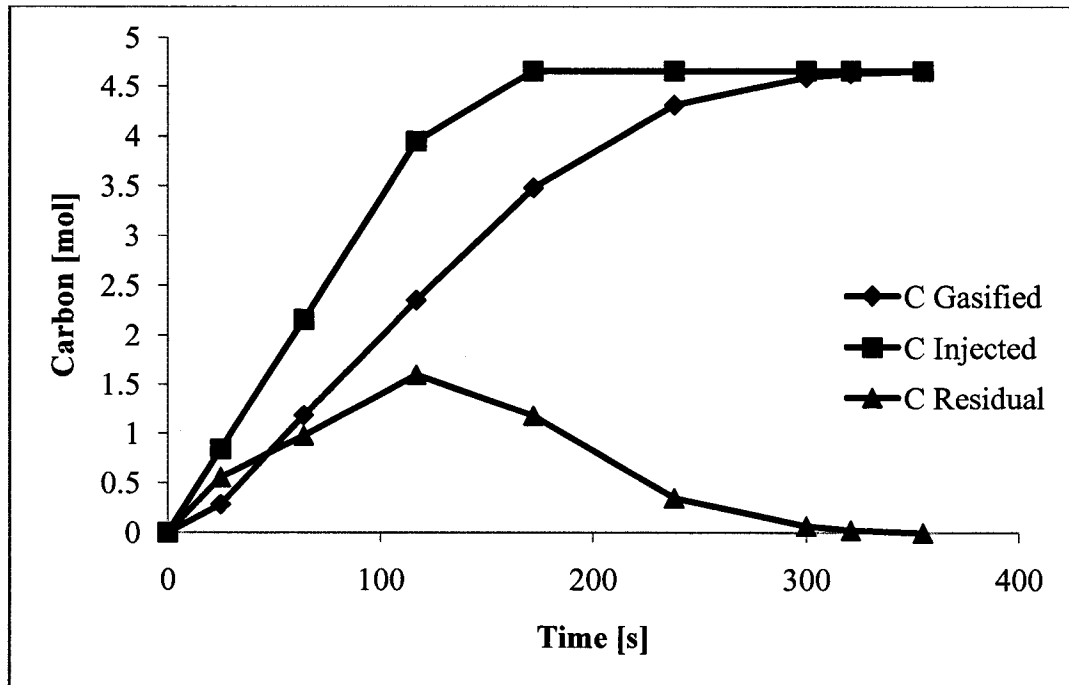
Figure A.7 - Experiment 16 carbon balance

A.2 Single Particle Model MATLAB Code

```
% Model for the reaction of a single carbon particle surrounded by
% a gas halo in slag

clear all
format short g

% Specify constants (injection NCR 1)

MC = 0.0120108;       % Molecular weight of C [kg/mol]

rhoC = 1100;      % Bulk density of carbon (reacted layer) [kg/m3]

d_p_0 = 0.000202;   % Initial particle diameter [m]

Vp_0 = (4/3)*pi*((d_p_0/2)^3);   % Initial particle volume [m3]

nC_0 = Vp_0*rhoC/MC;     % Initial number of moles in carbon
                         % particle [mol]

a0 = 0.265;      % Slag oxygen potential, defined as the
                 % equilibrium pCO2/pCO ratio at the slag-gas
                 % interface

pCO2_C = 3.81e-5;    % Equilibrium partial pressure of CO2 at
                     % carbon-gas interface [atm]

pCO2_sl = a0/(1+a0);     % Equilibrium partial pressure of CO2 at
                         % slag-gas interface [atm]

temp = 1900;     % Temperature [K]

phi1 = (10^((-13200/temp)+8.60))/60;     % Temperature-dependent
                                         % rate parameter for
                                         % carbon-gas reaction
                                         % [1/atm/s]

phiCO = 10^((-5940/temp)+3.46);     % Temperature-dependent
                                    % parameter for carbon surface
                                    % poisoning effect by CO [atm]

ka = 0.437;     % Slag-gas rate constant [mol/m2/atm/s]

MCO = 0.0280101;     % Molecular weight of CO [kg/mol]
rhoCO = 1.145;       % Density of CO [kg/m3]

delta_t = 0.25;      % Time step [s]
nC_stop = 1e-12;     % Amount of carbon at which model ends [mol]
```

```
% Set initial values

t = 0;
c = 1;      % while loop counter
nC = nC_0;


% Solution

while nC > nC_stop

    % Set rate at carbon-gas and slag-gas interfaces equal,
    % solve for pCO2

    solve_pCO2 = @(x) (nC_0*(phi1*phiCO*(pCO2_C-x)/...
        (1+phiCO-x))*exp(phi1*phiCO*t*(pCO2_C-x)/(1+phiCO-x)))-...
        (4*pi*((MCO/rhoCO)^2)*(ka^3)*(t^2)*(((x*(1+a0))-a0)^3));

    if c == 1
        xo = 0;
    else
        xo = particle((c-1),4);
    end

    pCO2 = fzero(solve_pCO2,xo);

    % Use calculated pCO2 to solve for rate,
    % amount of carbon and bubble diameter

    dnC = -nC_0*(phi1*phiCO*(pCO2_C-pCO2)/(1+phiCO-pCO2))...
        *exp(phi1*phiCO*t*(pCO2_C-pCO2)/(1+phiCO-pCO2));

    nC = nC_0*exp(phi1*phiCO*t*(pCO2_C-pCO2)/(1+phiCO-pCO2));

    diam_b = 1000*(((((36*pi)^(1/3))/pi)*((MCO/rhoCO)^(2/3))*...
        ((nC_0-nC)^(2/3)))^(1/2));


    % Construct "particle" matrix

    particle(c,1) = t;          % Time [s]
    particle(c,2) = dnC;        % Reaction rate [molC/s]
    particle(c,3) = nC;         % Amount of carbon in particle
                                % [mol]
    particle(c,4) = pCO2;       % Partial pressume of CO2 in gas
                                % bubble [atm]
    particle(c,5) = diam_b;     % Bubble diameter [mm]

    t = t + delta_t;
```

```
    c = c + 1;

end % while loop


% Output

figure(1)
plot(particle(1:end,1), particle(1:end,2))
xlabel('Time [s]')
ylabel('-dnC/dt [molC/s]')
title('Rate of carbon gasification')

figure(2)
plot(particle(1:end,1), particle(1:end,3))
xlabel('Time [s]')
ylabel('nC [mol]')
title('Amount of carbon in particle')

figure(3)
plot(particle(1:end,1), particle(1:end,4),...
    particle(1:end,1), pCO2_sl, ':')
xlabel('Time [s]')
ylabel('pCO2')
legend('pCO2 bubble', 'pCO2 eq, slag')
title('Partial pressure of CO2 in gas bubble')

figure(4)
plot(particle(1:end,1), particle(1:end,5))
xlabel('Time [s]')
ylabel('Bubble diameter [mm]')

particle

save sing_part_NCR1.dat particle -ascii

% The end
```

A.3 Injection Model MATLAB Code

```
% Model for Multiple Carbon Particles injected over Time at a
% fixed Rate

clear all
format short g


% Specify constants
```

```
MC = 0.0120108;      % Molecular weight of C [kg/mol]

rhoC = 1100;     % Bulk density of carbon (reacted layer) [kg/m3]

d_p_0 = 0.000202;    % Initial particle diameter [m]

Vp_0 = (4/3)*pi*((d_p_0/2)^3);   % Initial particle volume [m3]

nC_0 = Vp_0*rhoC/MC;     % Initial number of moles in carbon
                         % particle [mol]

a0 = 0.265;      % Slag oxygen potential, defined as the
                 % equilibrium pCO2/pCO ratio at the slag-gas
                 % interface

pCO2_C = 3.81e-5;    % Equilibrium partial pressure of CO2 at
                     % carbon-gas interface [atm]

pCO2_sl = a0/(1+a0);     % Equilibrium partial pressure of CO2 at
                         % slag-gas interface [atm]

temp = 1900;     % Temperature [K]

phi1 = (10^((-13200/temp)+8.60))/60;     % Temperature-dependent
                                         % rate parameter for
                                         % carbon-gas reaction
                                         % [1/atm/s]

phiCO = 10^((-5940/temp)+3.46);      % Temperature-dependent
                                     % parameter for carbon surface
                                     % poisoning effect by CO [atm]

ka_0 = 0.437;    % Slag-gas rate constant [mol/m2/atm/s]

CFe_0 = 21.9;    % Initial concentration of Fe in slag [mol %]

delta_Fe = 2.00;     % Decrease in concentration on Fe in slag over
                     % the injection time, t_inj [mol %]

q = ka_0/((CFe_0)^2);    % Slag-gas rate parameter; a function of
                         % slag composition
                         % (equal to ka_0/(CFe_0^2))

MCO = 0.0280101;     % Molecular weight of CO [kg/mol]

rhoCO = 1.145;   % Density of CO [kg/m3]

Ri = 0.0352;     % Injection rate [molC/s]

Rp = Ri/nC_0;    % Injection rate [particles/s]
```

```
t_inj = 138;    % Time of injection stop [s]

delta_t = 0.25; % Time step [s]

t_stop = 420;    % Time at which model ends


% Solution

c = 1;  % Matrix index counter

for t = 0:(delta_t):(t_stop)

    if t < t_inj    % Time during carbon injection

        Np = Rp*t;

        ka = q*((CFe_0-(delta_Fe*(t/t_inj)))^2);

        solve_pCO2 = @(x) (Rp*nC_0*((exp(phi1*phiCO*t*...
            (pCO2_C-x)/(1+phiCO-x)))-1))-...
            (Rp*(4*pi/3)*((MCO/rhoCO)^2)*(ka^3)*...
            (((x*(1+a0))-a0)^3)*(t^3));
        if c == 1
            xo = 0;
        else
            xo = matr((c-1),4);
        end
        pCO2_tot = fzero(solve_pCO2,xo);

        dnC_tot = -Rp*nC_0*((exp(phi1*phiCO*t*...
            (pCO2_C-pCO2_tot)/(1+phiCO-pCO2_tot)))-1);

        nC_tot = Rp*nC_0*((1+phiCO-pCO2_tot)/(phi1*phiCO*...
            (pCO2_C-pCO2_tot)))*((exp(phi1*phiCO*t*...
            (pCO2_C-pCO2_tot)/(1+phiCO-pCO2_tot)))-1);

        A_sl_act = -dnC_tot/(ka*((pCO2_tot*(1+a0))-a0));

        A_sl_tot = Np*((36*pi)^(1/3))*((MCO/rhoCO)^(2/3))*...
            ((nC_0-(nC_tot/Np))^(2/3));

        db_avg = 1000*(A_sl_tot/(pi*Np))^(1/2);

    else            % Time after carbon injection ends

        Np = Rp*t_inj;

        ka = q*((CFe_0-(delta_Fe*(t/t_inj)))^2);
```

```
        solve_pCO2 = @(x) (Rp*nC_0*((exp(phi1*phiCO*t*...
            (pCO2_C-x)/(1+phiCO-x)))-(exp(phi1*phiCO*(t-t_inj)*...
            (pCO2_C-x)/(1+phiCO-x)))))-...
            (Rp*(4*pi/3)*((MCO/rhoCO)^2)*(ka^3)*...
            (((x*(1+a0))-a0)^3)*((t^3)-((t-t_inj)^3)));
        xo = matr((c-1),4);
        pCO2_tot = fzero(solve_pCO2,xo);

        dnC_tot = -Rp*nC_0*((exp(phi1*phiCO*t*...
            (pCO2_C-pCO2_tot)/(1+phiCO-pCO2_tot)))-...
            (exp(phi1*phiCO*(t-t_inj)*(pCO2_C-pCO2_tot)/...
            (1+phiCO-pCO2_tot))));

        nC_tot = Rp*nC_0*((1+phiCO-pCO2_tot)/(phi1*phiCO*...
            (pCO2_C-pCO2_tot)))*(exp(phi1*phiCO*t*...
            (pCO2_C-pCO2_tot)/(1+phiCO-pCO2_tot)))-...
            (exp(phi1*phiCO*(t-t_inj)*(pCO2_C-pCO2_tot)/...
            (1+phiCO-pCO2_tot))));

        A_sl_act = -dnC_tot/(ka*((pCO2_tot*(1+a0))-a0));

        A_sl_tot = Np*((36*pi)^(1/3))*((MCO/rhoCO)^(2/3))*...
            ((nC_0-(nC_tot/Np))^(2/3));

        db_avg = 1000*(A_sl_tot/(pi*Np))^(1/2);

    end

    matr(c,1) = t;                % Time [s]
    matr(c,2) = dnC_tot;          % Overall carbon gasification
                                  % rate [mol/s]
    matr(c,3) = nC_tot;           % Total amount of carbon in
                                  % slag [mol]
    matr(c,4) = pCO2_tot;         % Overall pCO2 in slag [atm]
    matr(c,5) = A_sl_act;         % Active slag surface area
                                  % [m2]
    matr(c,6) = A_sl_tot;         % Total slag surface area [m2]
    matr(c,7) = A_sl_act/A_sl_tot; % Fraction of slag surface
                                  % area active
    matr(c,8) = db_avg;           % Average bubble diameter [mm]

    c = c + 1;

end % t loop


% Output

figure(1)
plot(matr(1:end,1), matr(1:end,2))
```

```
xlabel('Time [s]')
ylabel('-dnC_tot/dt [mol/s]')
title('Total carbon gasification rate')

figure(2)
plot(matr(1:end,1), matr(1:end,3))
xlabel('Time [s]')
ylabel('nC_tot [mol]')
title('Total amount of carbon in slag')

figure(3)
plot(matr(1:end,1), matr(1:end,4), matr(1:end,1), pCO2_sl, ':')
xlabel('Time [s]')
ylabel('pCO2_tot [atm]')
legend('pCO2 in gas', 'pCO2 eq, slag')
title('Partial pressure of CO2 in slag')

figure(4)
plot(matr(1:end,1), matr(1:end,7))
xlabel('Time [s]')
ylabel('Fraction of slag surface area active')

figure(5)
plot(matr(1:end,1), matr(1:end,8))
xlabel('Time [s]')
ylabel('Average bubble diameter [mm]')

matr

save inj_NCR1.dat matr -ascii

% The end
```

A.4 Injection Model Predictions

The injection model predictions for residual carbon in the slag, partial pressure of CO_2, active fraction of slag-gas interfacial area and average bubble diameter are given in Figure A.8 to Figure A.35. The predicted CO_2 pressures for non-adjusted carbon reactivities are not shown as they are indistinguishable from those predicted for the adjusted cases at the scale shown.
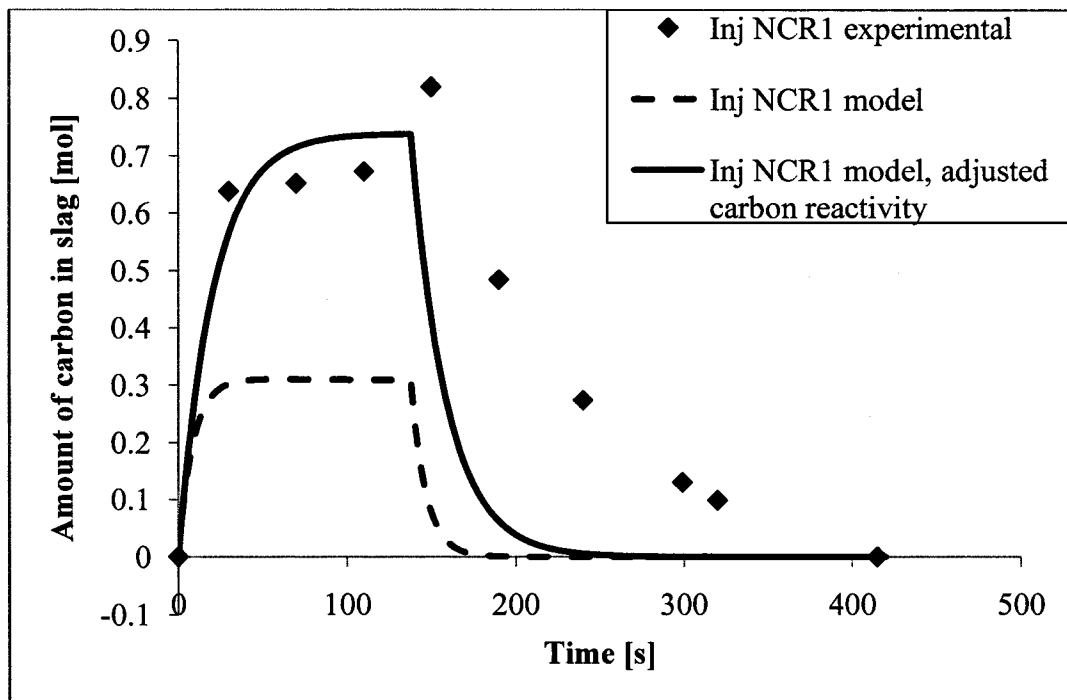
Figure A.8 - Residual carbon in slag, experiment "Nucor 1"
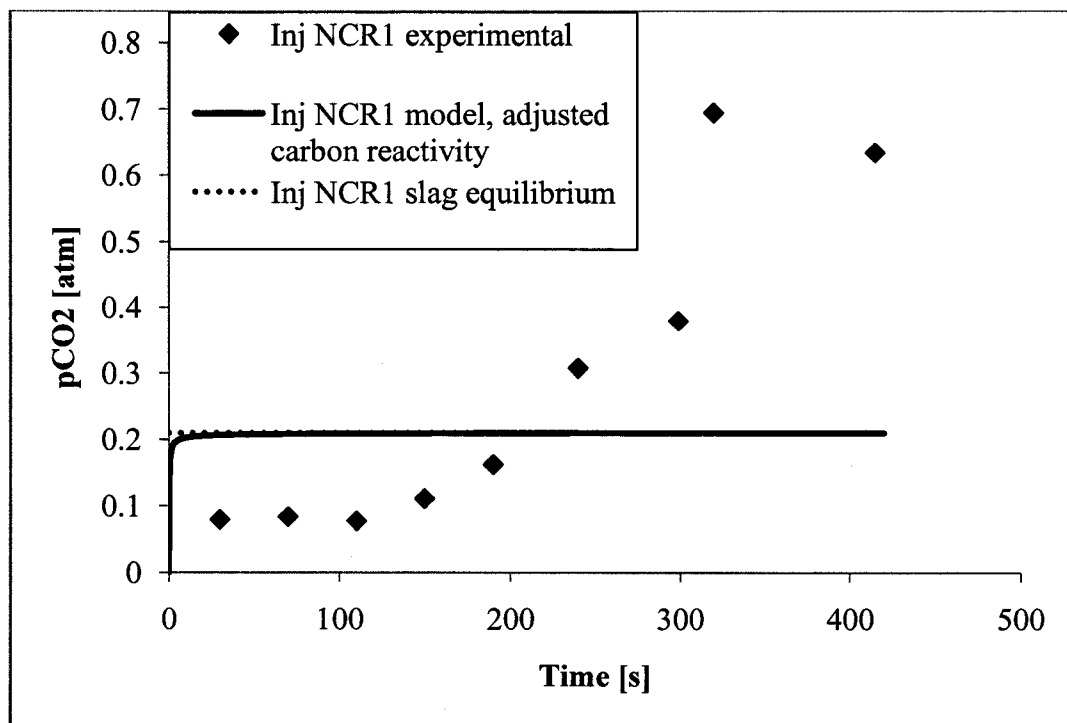
Figure A.9 - Pressure of CO₂, experiment "Nucor 1"
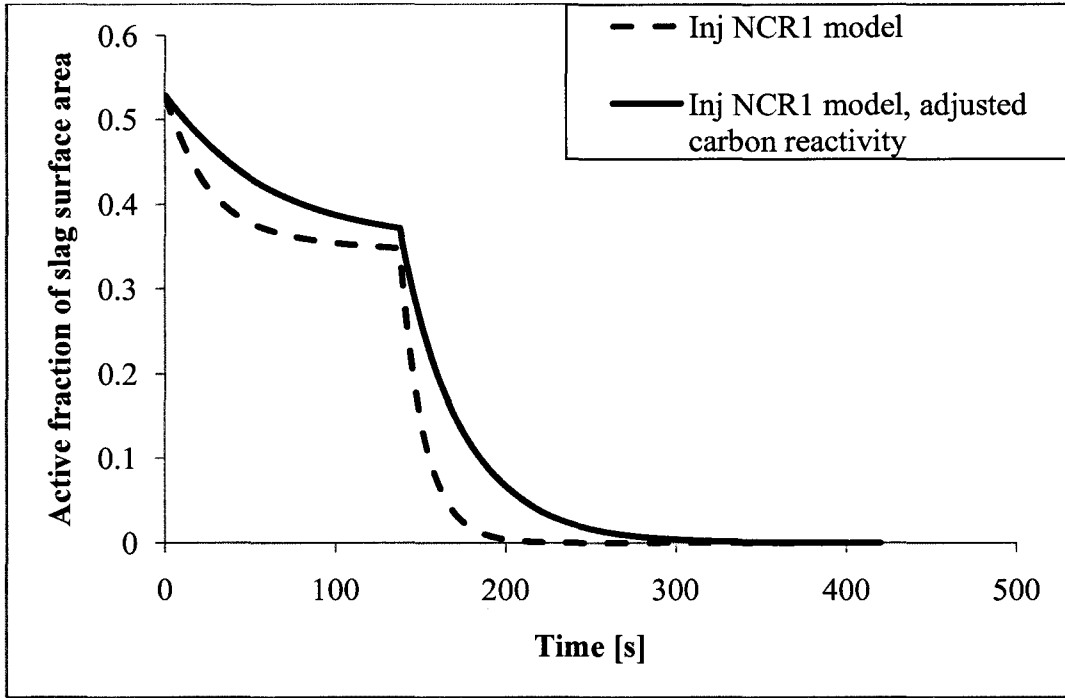
Figure A.10 - Predicted active fraction of slag interfacial area, experiment "Nucor 1"
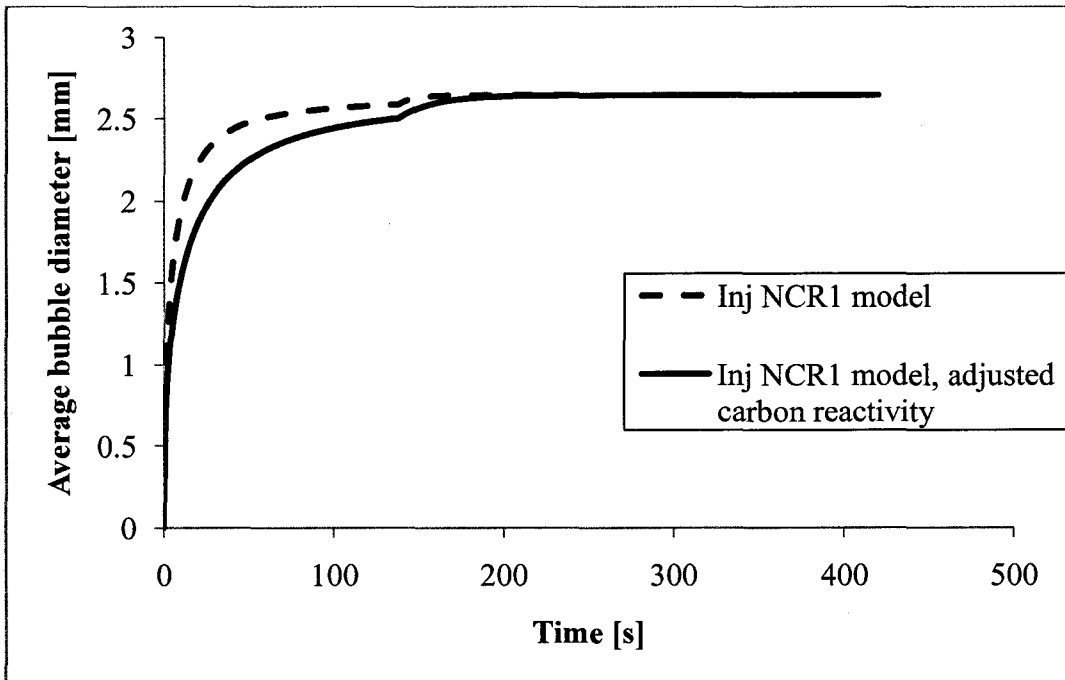
Figure A.11 - Predicted average bubble diameter, experiment "Nucor 1"
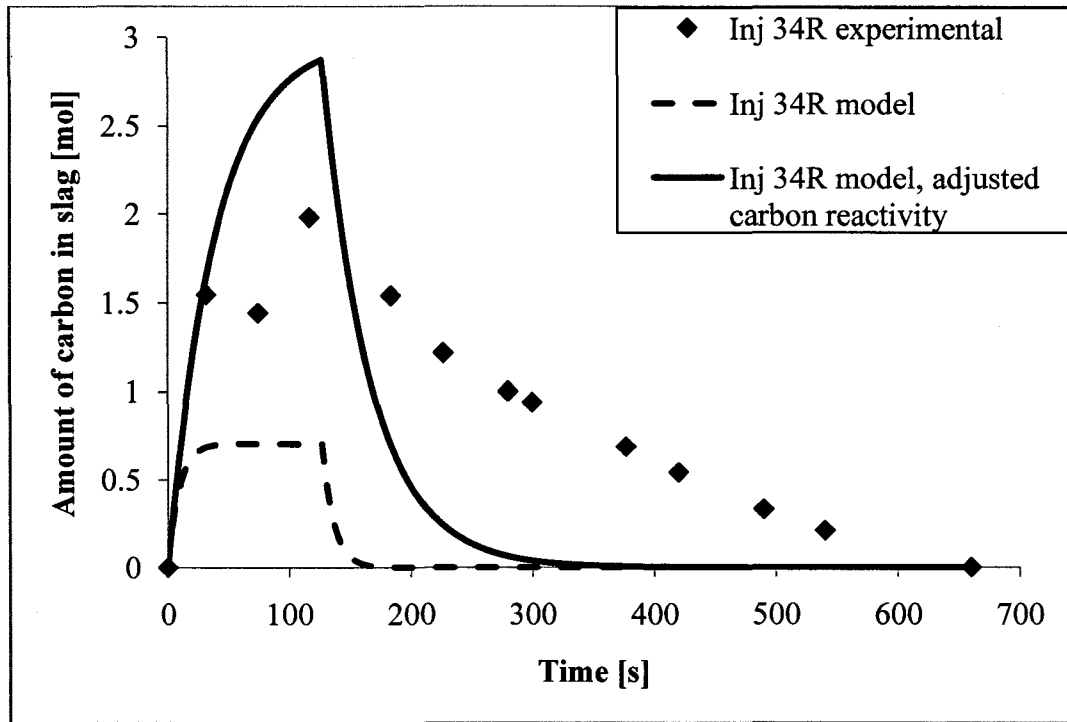
Figure A.12 - Residual carbon in slag, experiment 34R
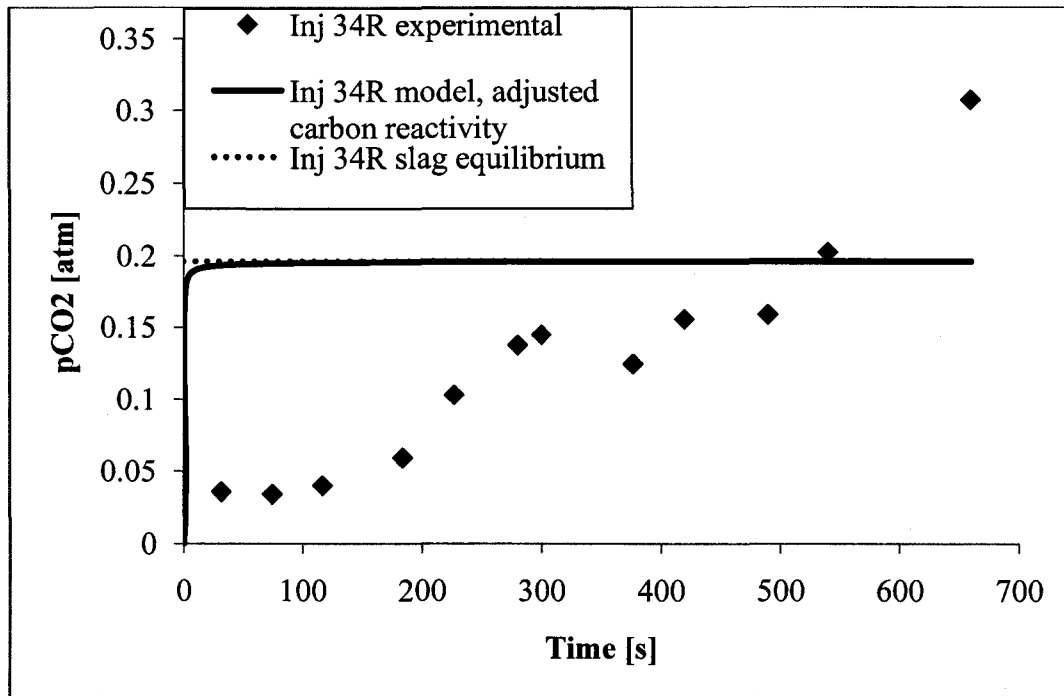
Figure A.13 - Pressure of CO₂, experiment 34R
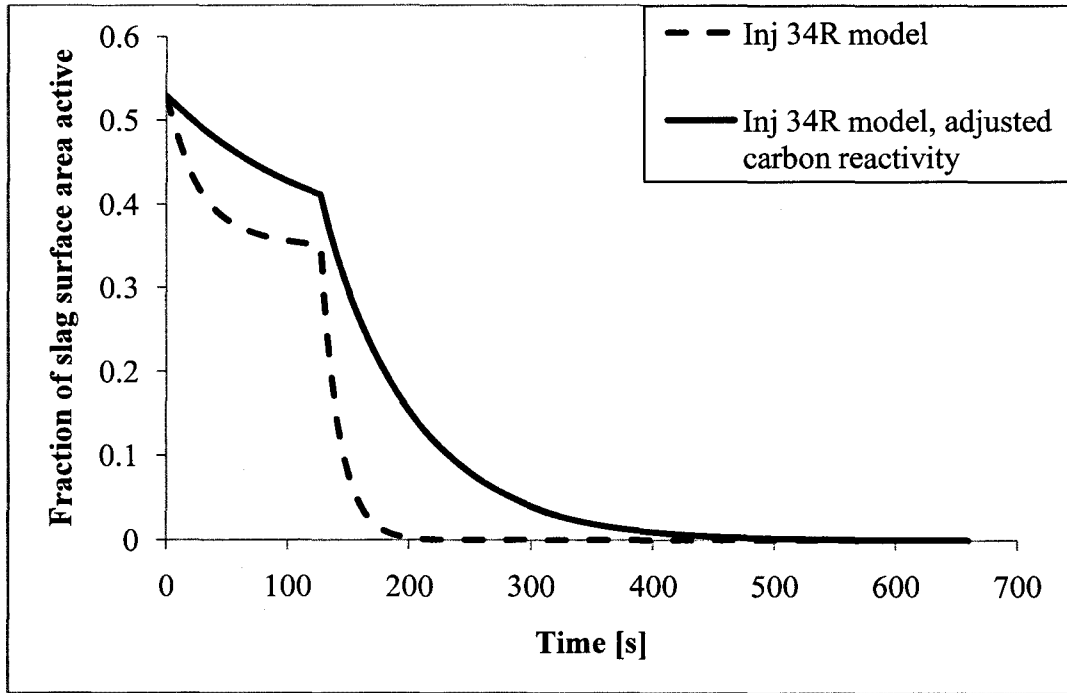
Figure A.14 - Predicted active fraction of slag interfacial area, experiment 34R
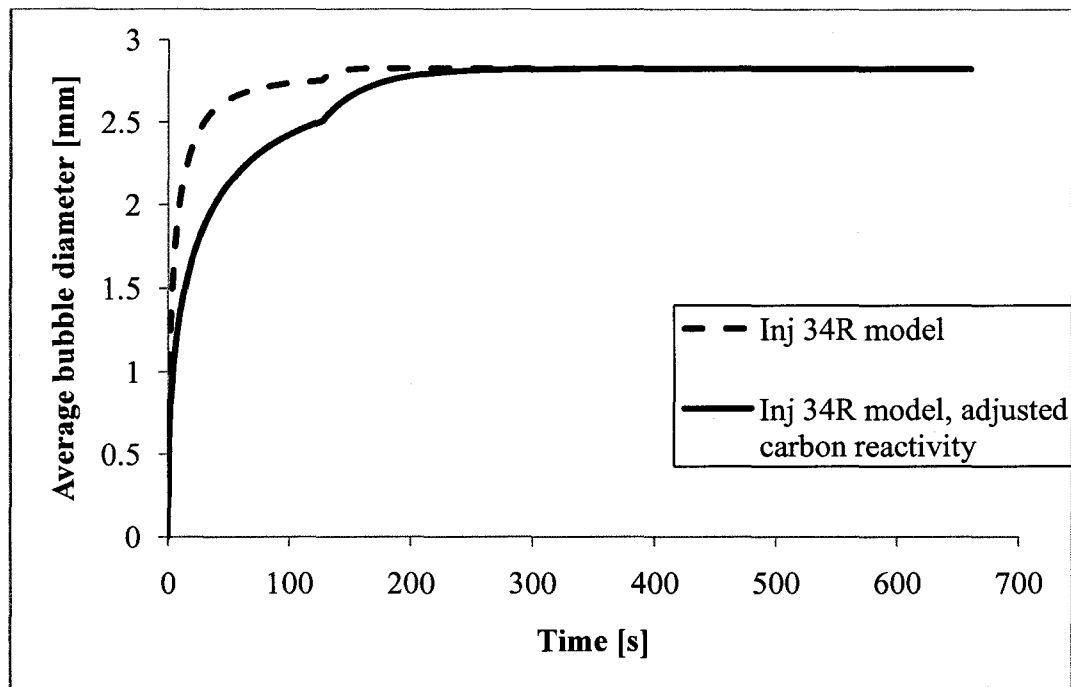
Figure A.15 - Predicted average bubble diameter, experiment 34R
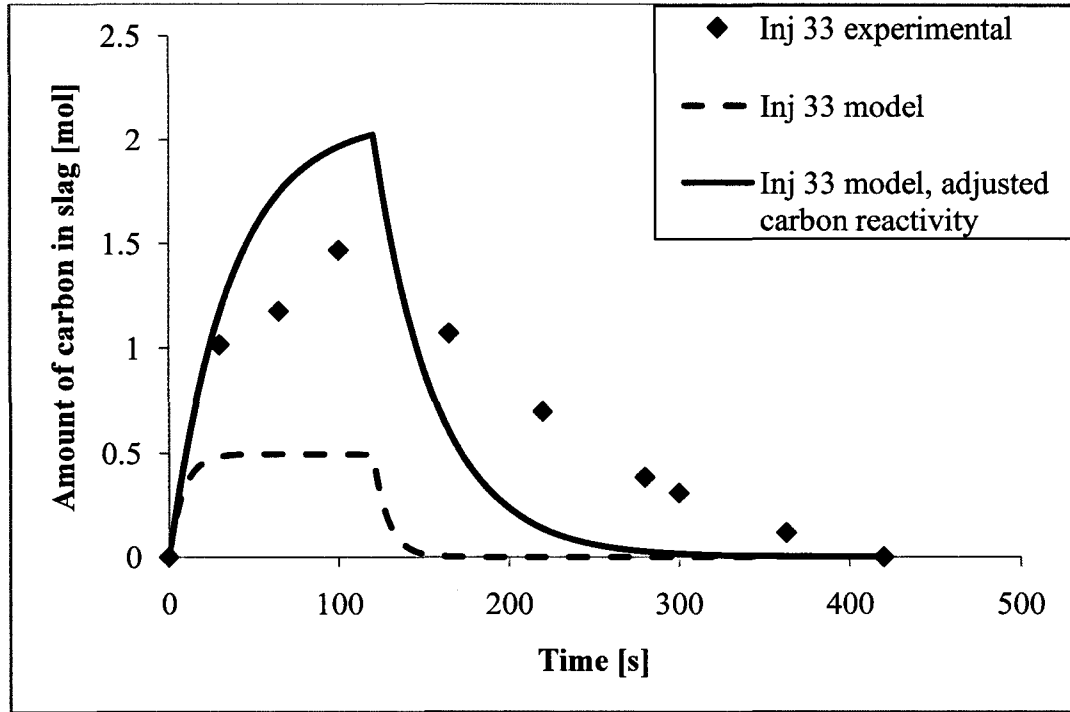
Figure A.16 - Residual carbon in slag, experiment 33
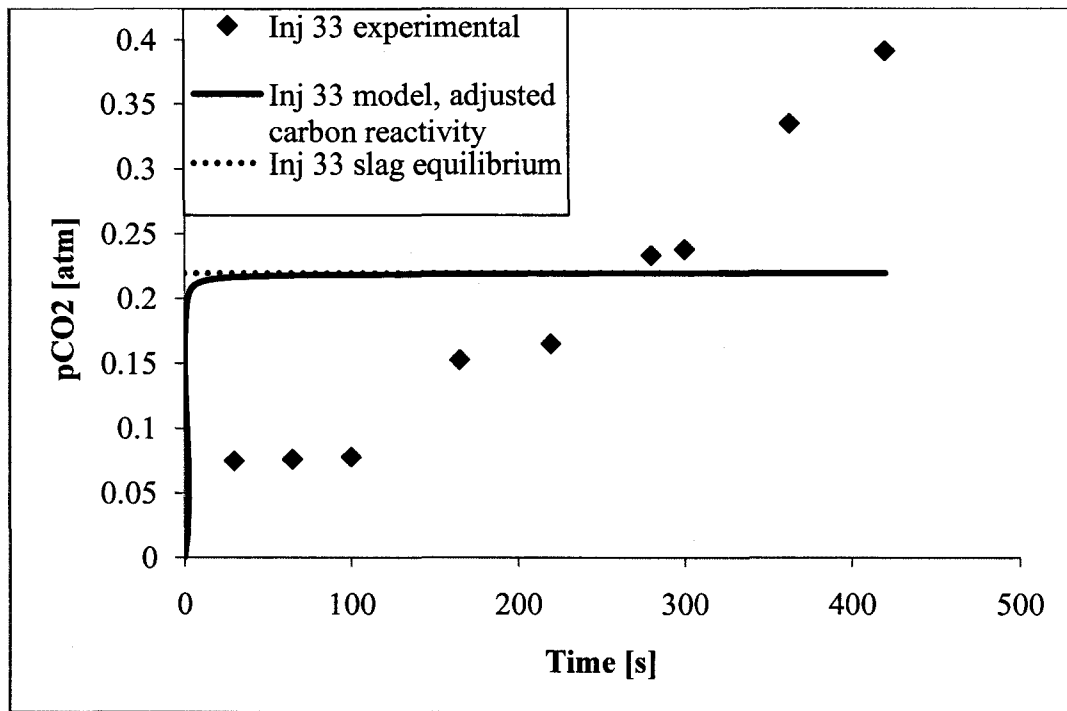
Figure A.17 - Pressure of CO₂, experiment 33
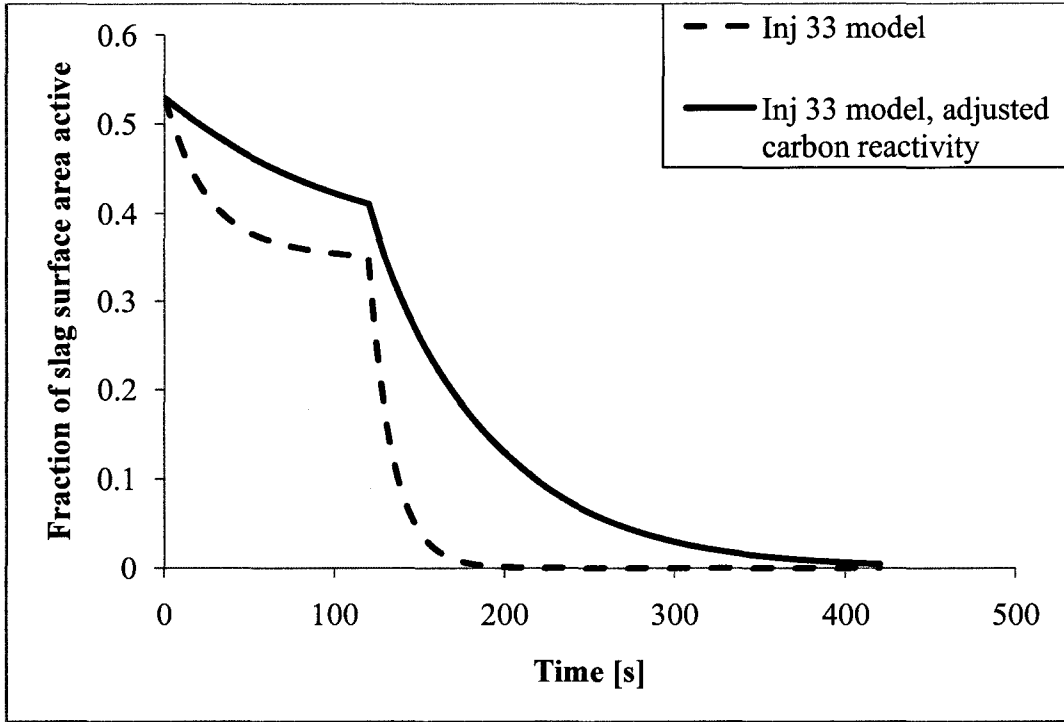
Figure A.18 - Predicted active fraction of slag interfacial area, experiment 33
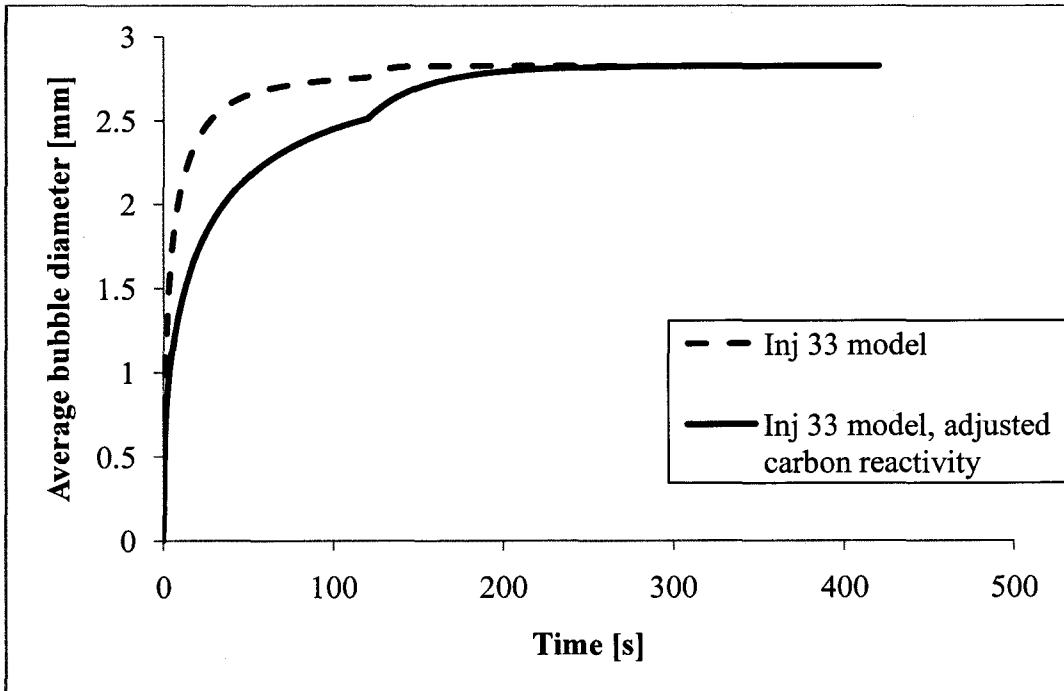
Figure A.19 - Predicted average bubble diameter, experiment 33
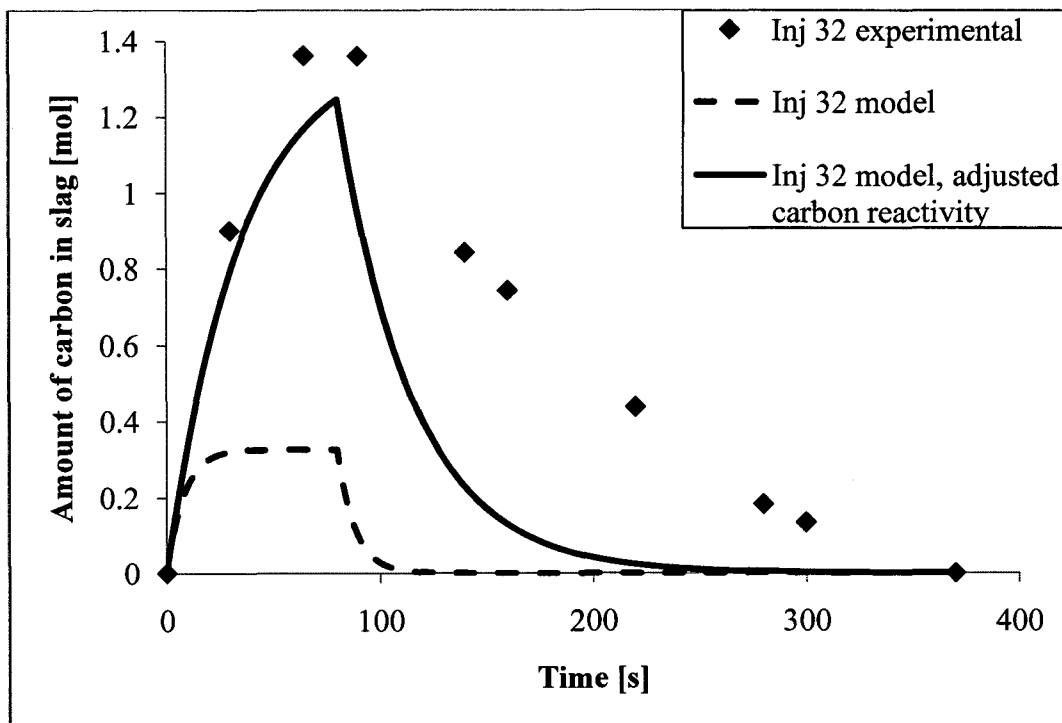
Figure A.20 - Residual carbon in slag, experiment 32
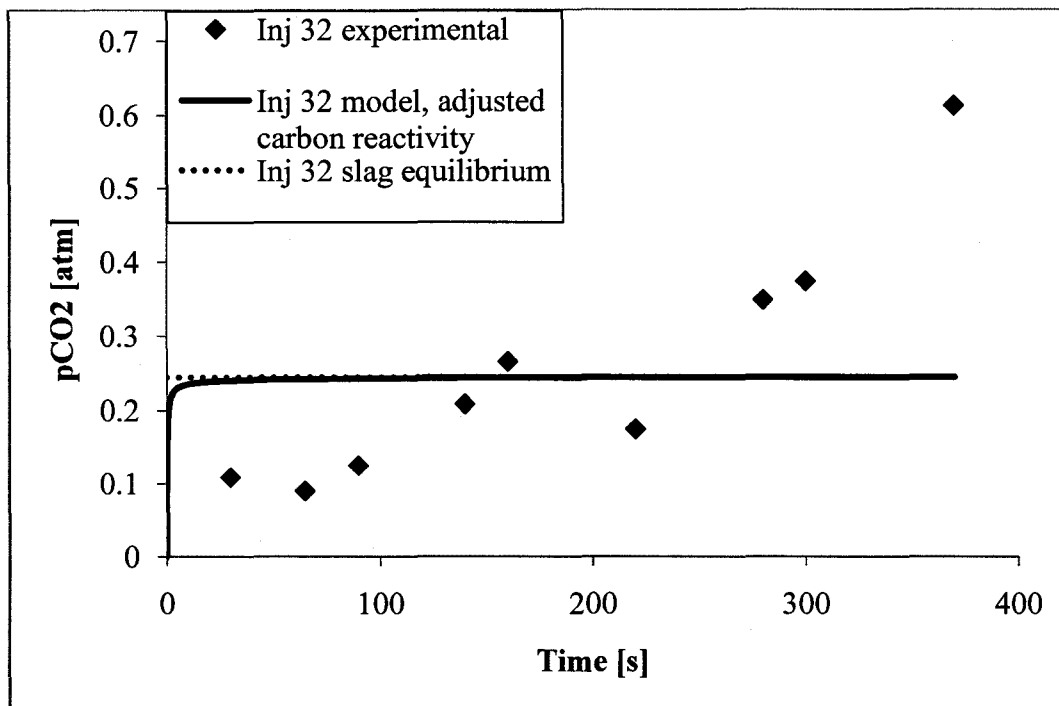
Figure A.21 - Pressure of CO₂, experiment 32
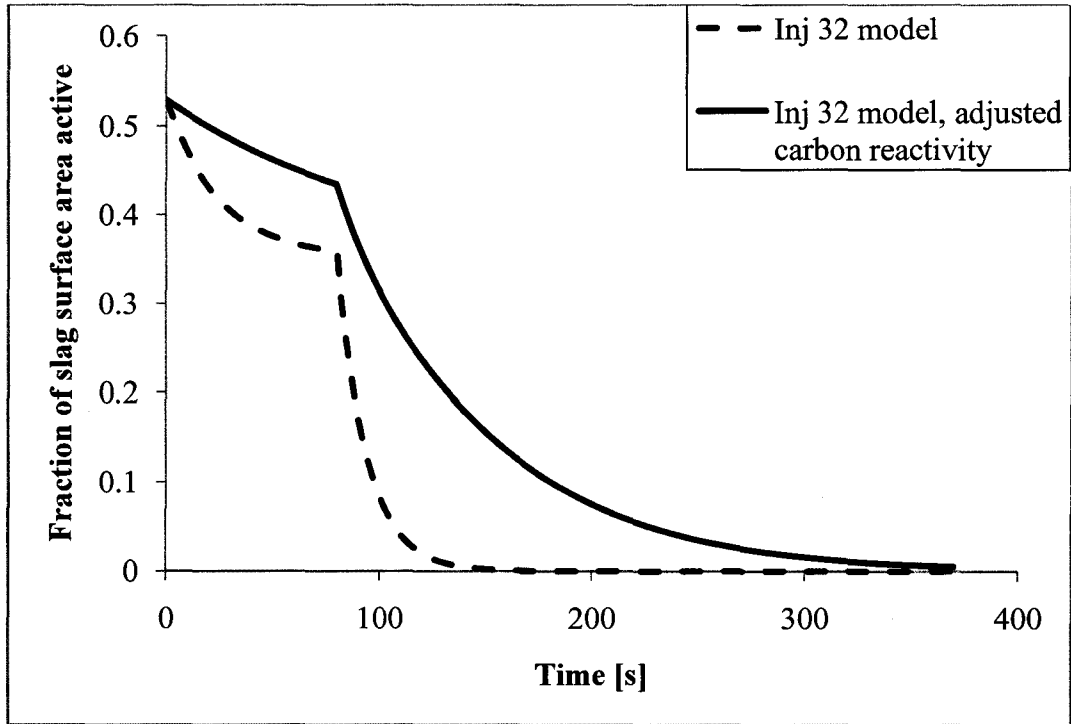
Figure A.22 - Predicted active fraction of slag interfacial area, experiment 32
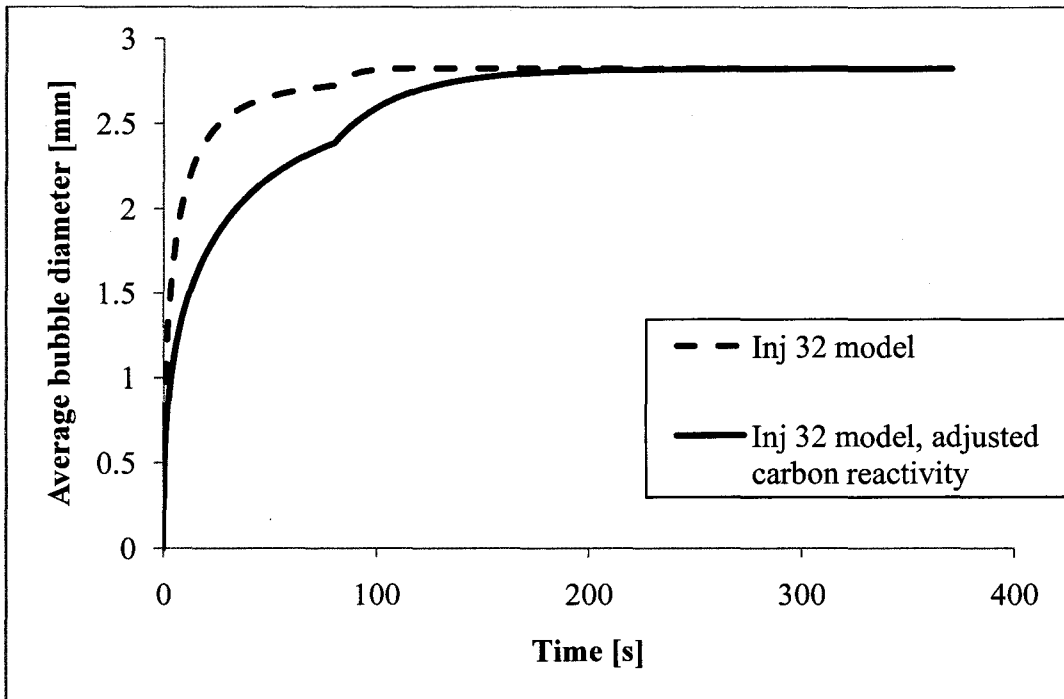
Figure A.23 - Predicted average bubble diameter, experiment 32
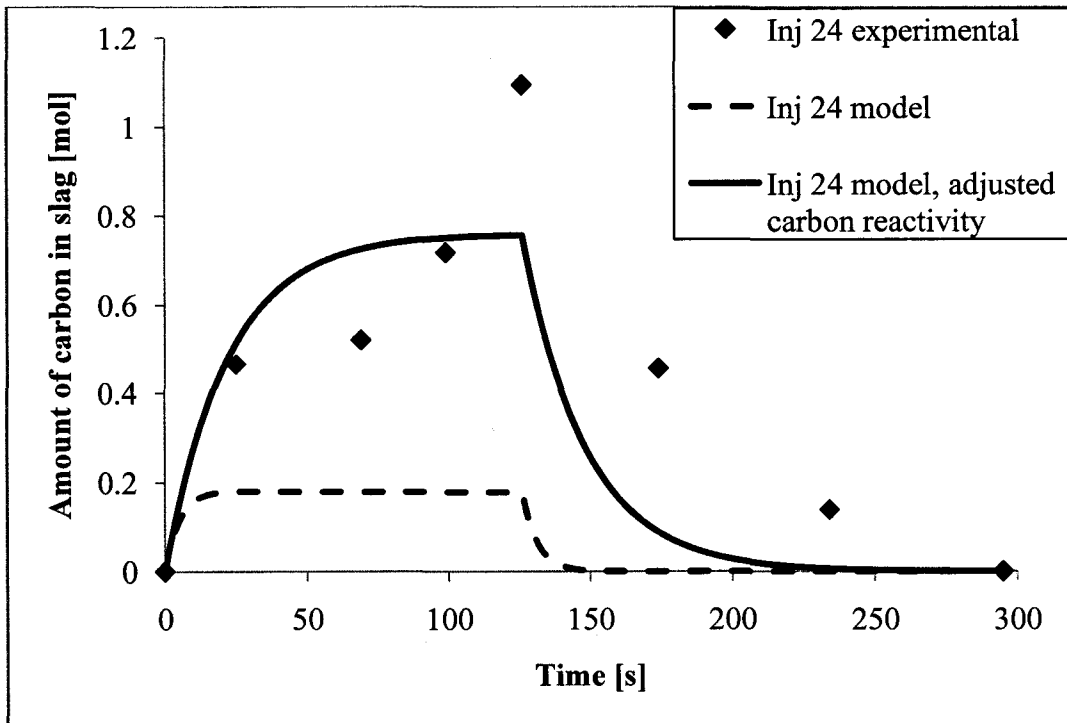
Figure A.24 - Residual carbon in slag, experiment 24
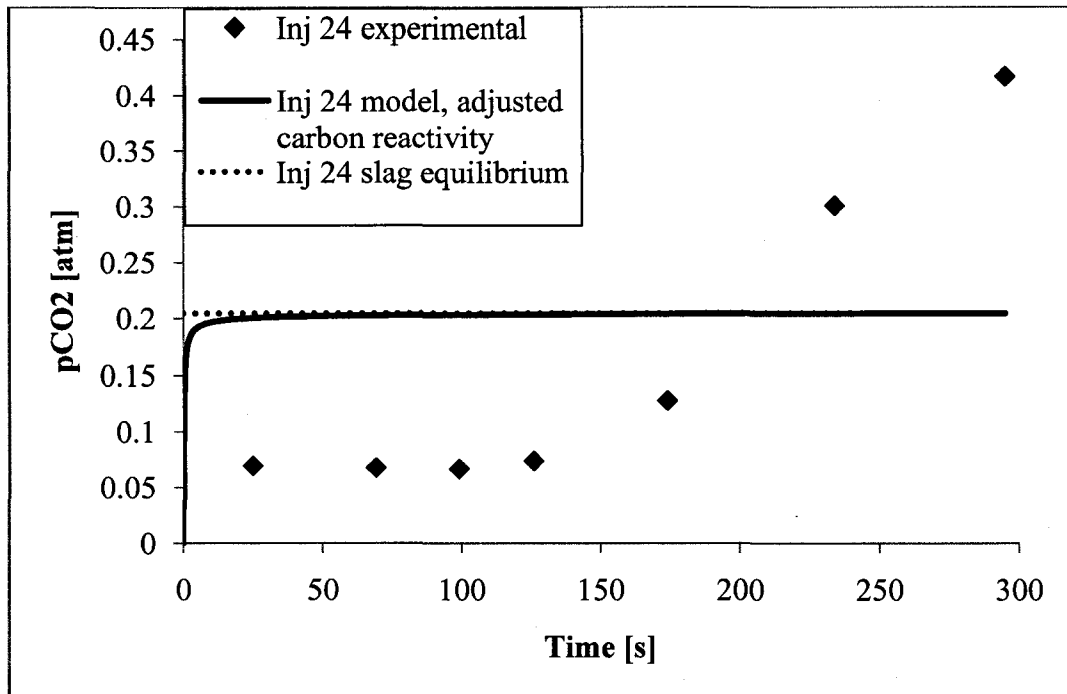
Figure A.25 - Pressure of CO$_2$, experiment 24
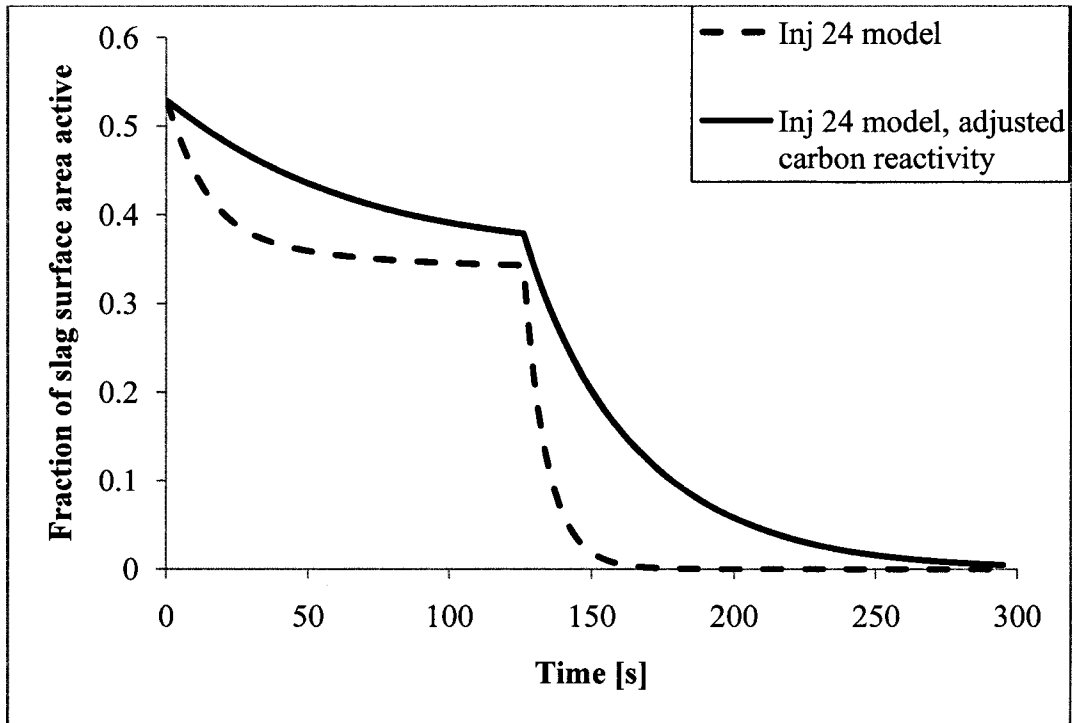
Figure A.26 - Predicted active fraction of slag interfacial area, experiment 24
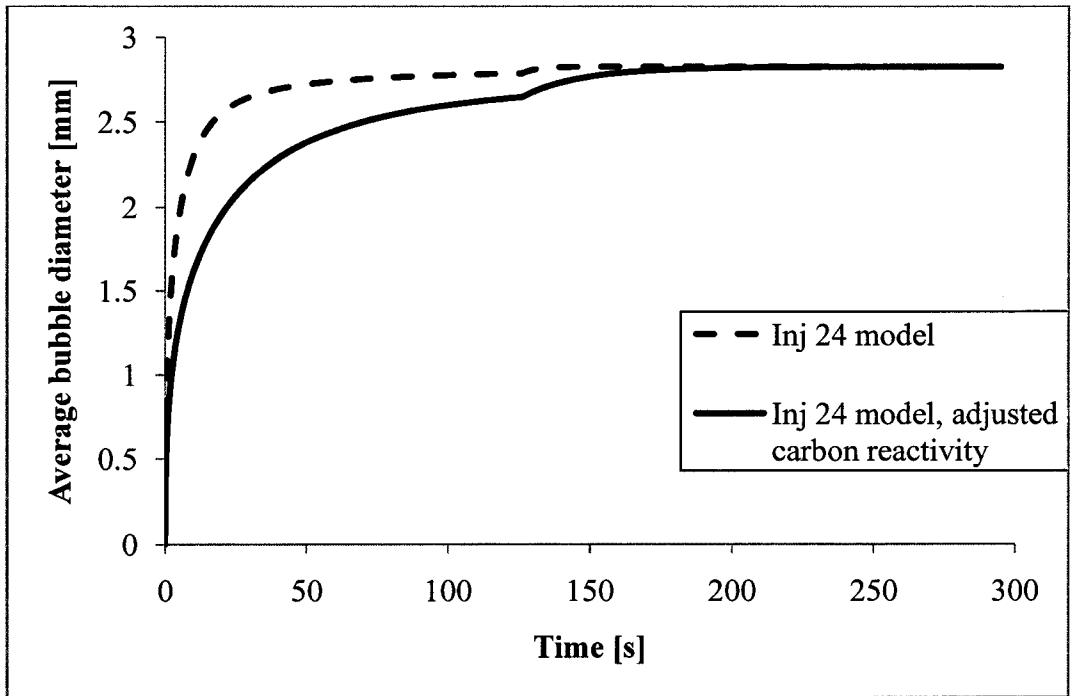
Figure A.27 - Predicted average bubble diameter, experiment 24
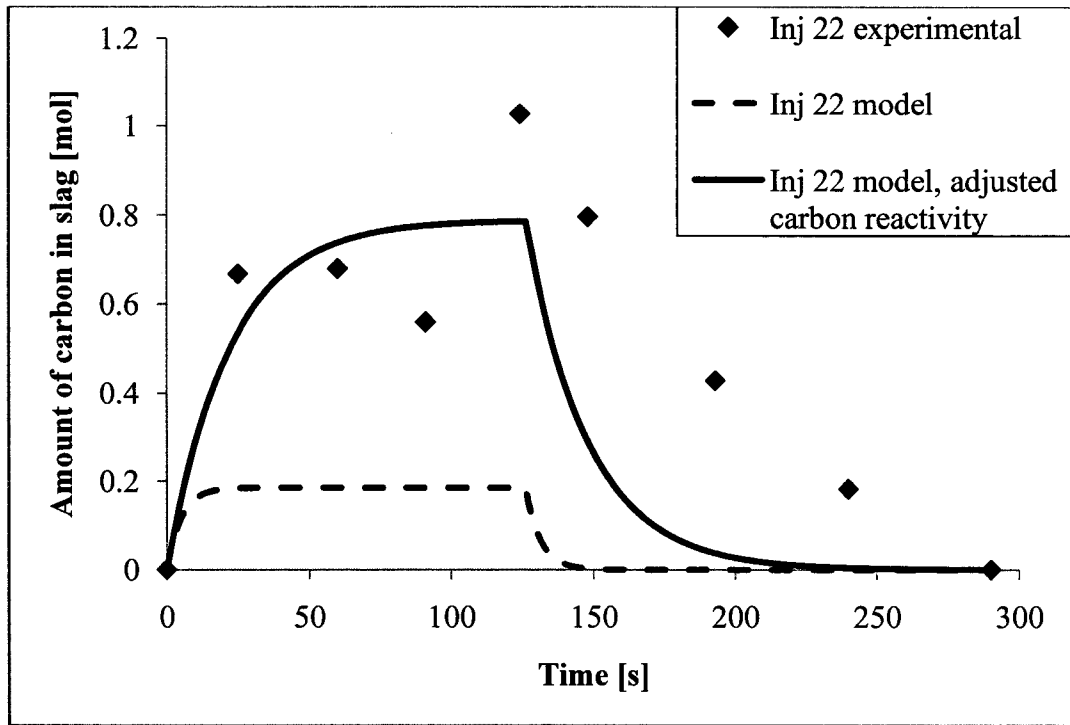
Figure A.28 - Residual carbon in slag, experiment 22
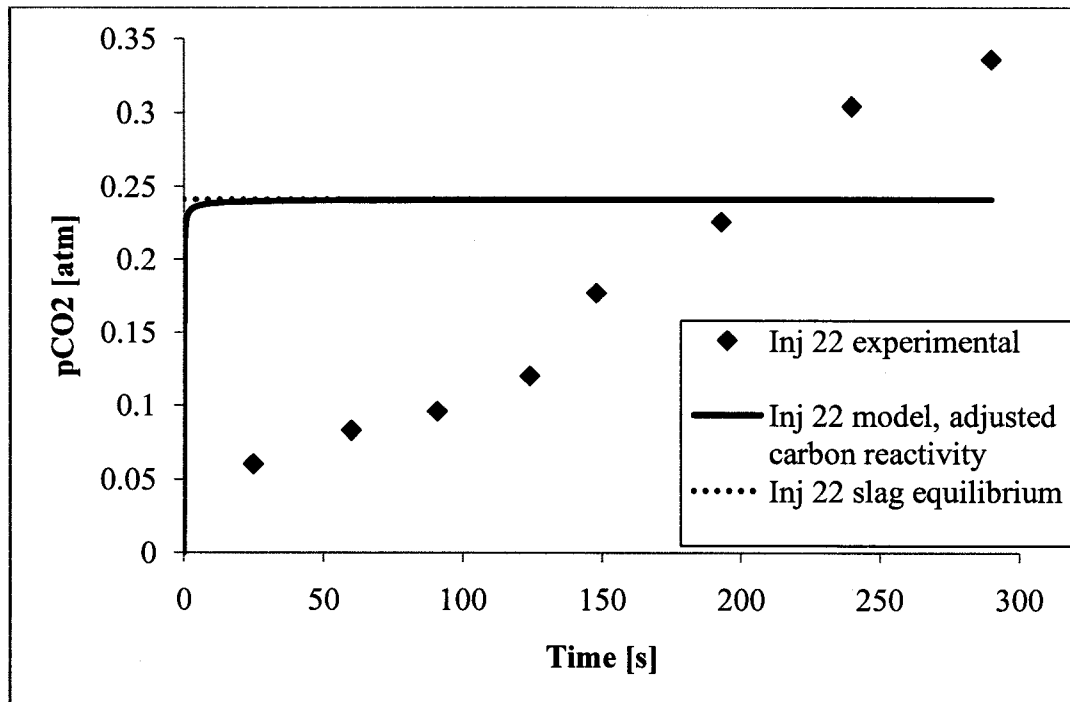
Figure A.29 - Pressure of CO₂, experiment 22
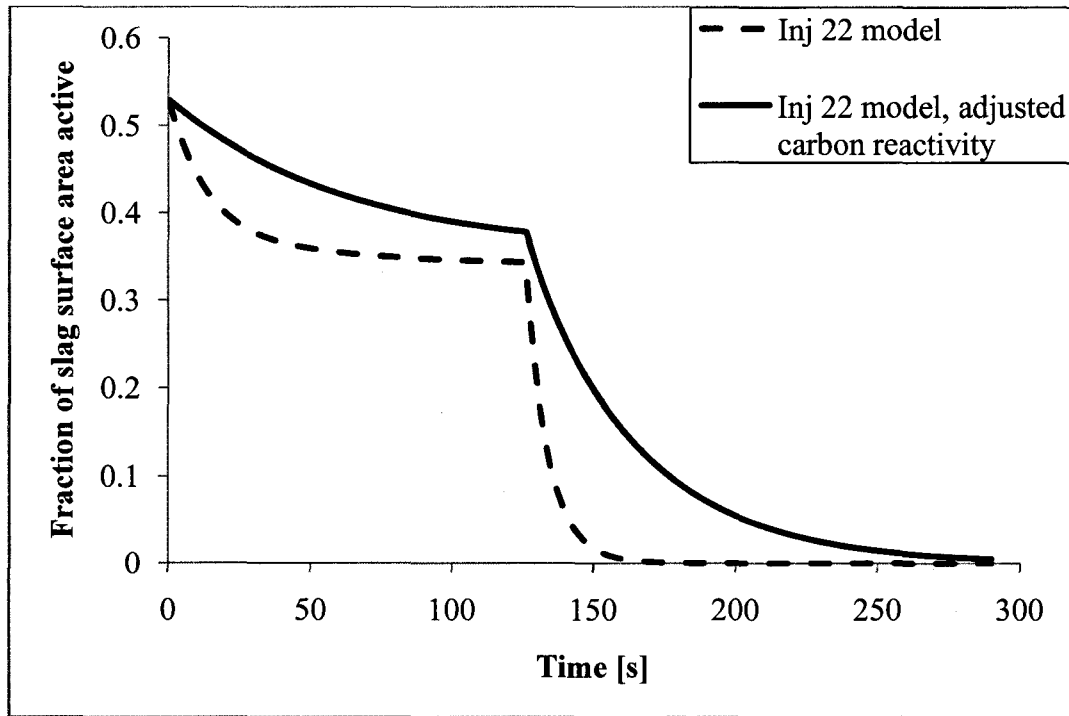
Figure A.30 - Predicted active fraction of slag interfacial area, experiment 22
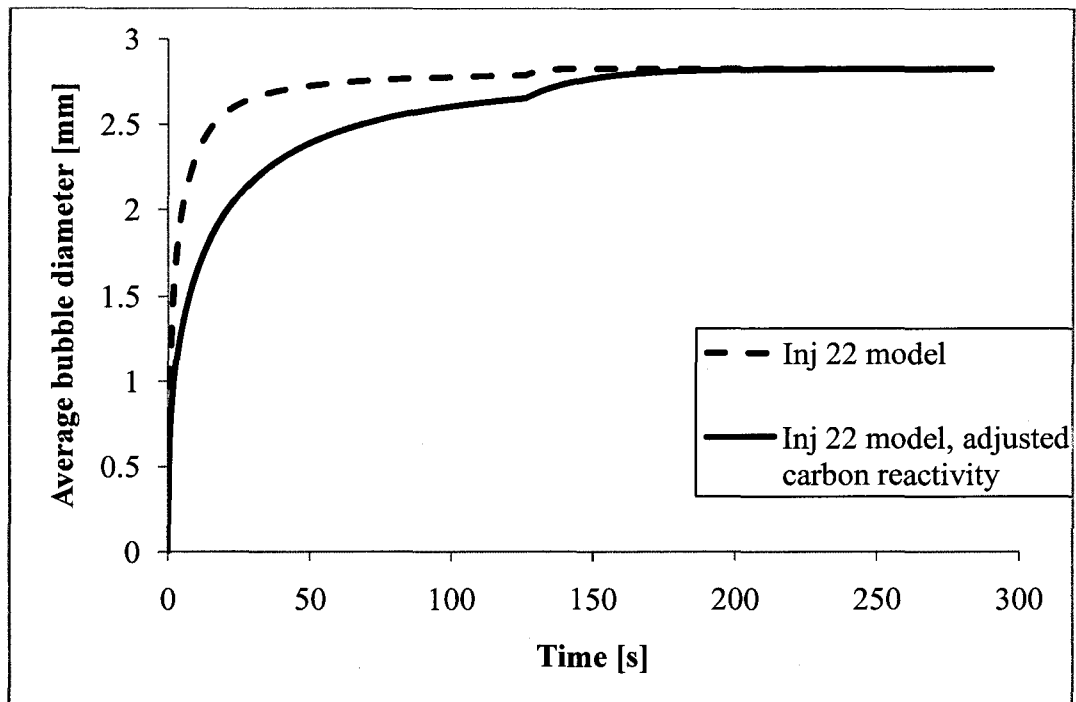
Figure A.31 - Predicted average bubble diameter, experiment 22
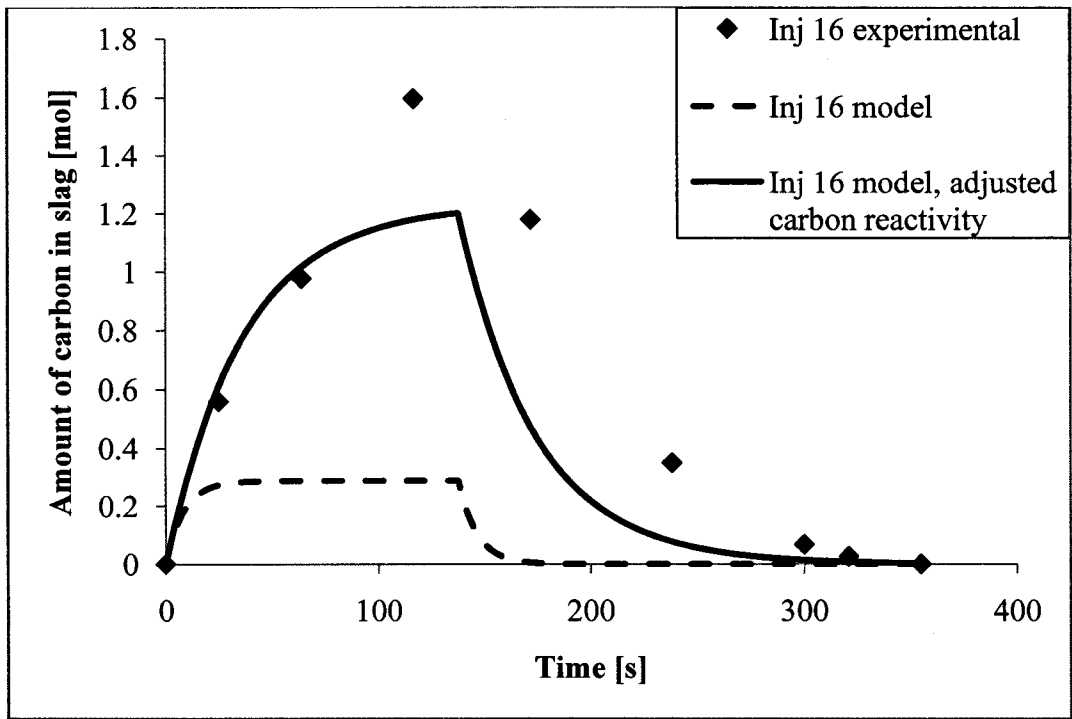
Figure A.32 - Residual carbon in slag, experiment 16
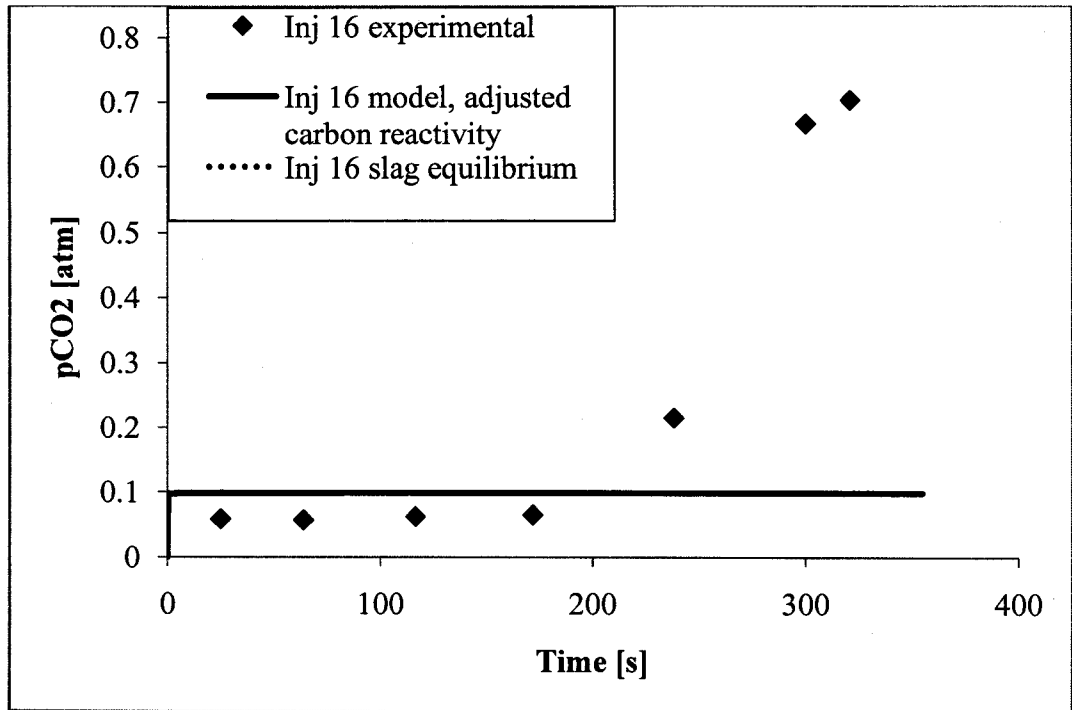
Figure A.33 - Pressure of CO₂, experiment 16
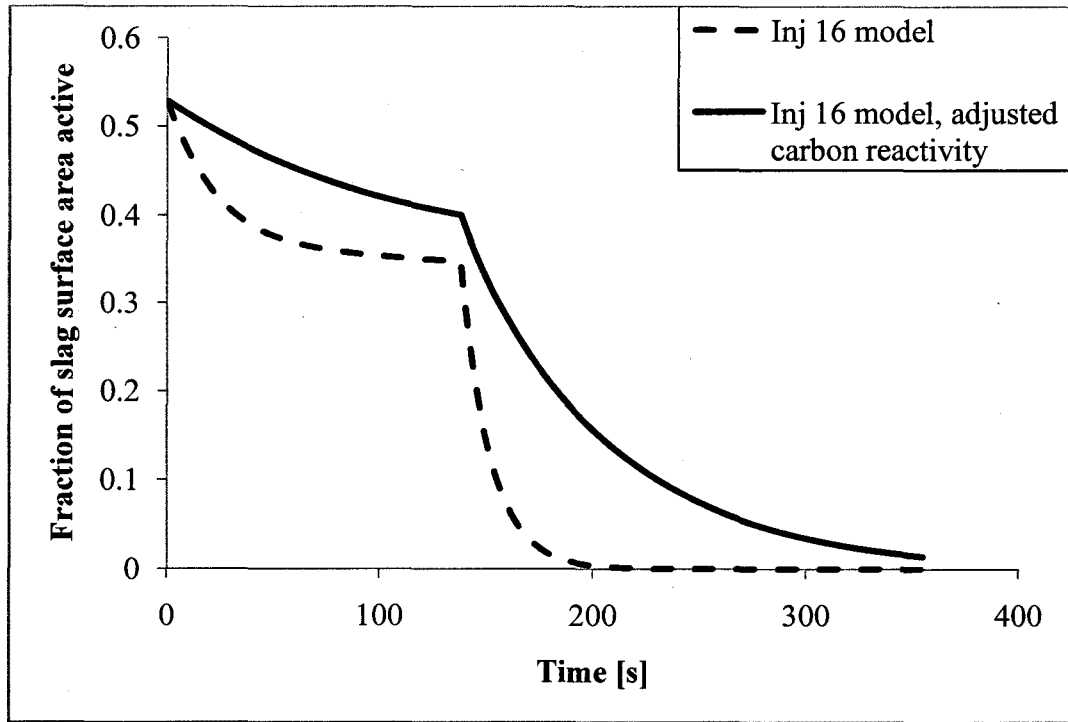
Figure A.34 - Predicted active fraction of slag interfacial area, experiment 16
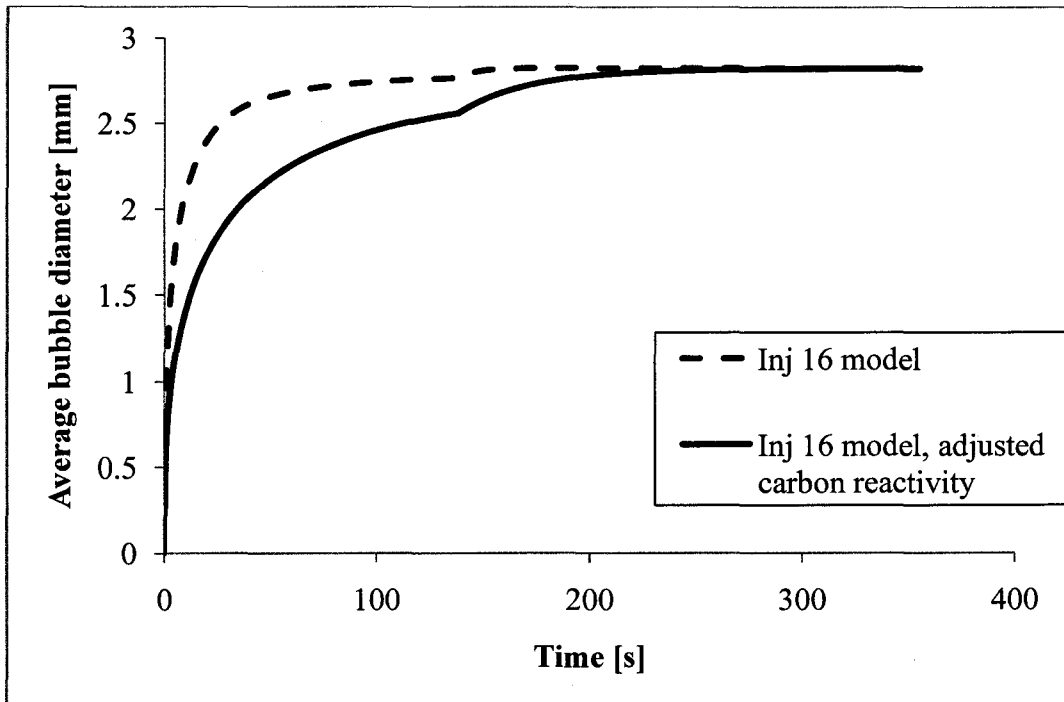
Figure A.35 - Predicted average bubble diameter, experiment 16